THESIS FOR THE DEGREE OF DOCTOR OF PHILOSOPHY

Design and Assessment of HVDC Off-shore Wind Turbine Generator

POOPAK ROSHANFEKR

Department of Energy and Environment
Division of Electric Power Engineering
CHALMERS UNIVERSITY OF TECHNOLOGY
Gothenburg, Sweden, 2015

Design and Assessment of HVDC Off-shore Wind Turbine Generator
POOPAK ROSHANFEKR
ISBN 978-91-7597-271-8

Doktorsavhandlingar vid Chalmers Tekniska Högskola
Ny serie nr. 3952
ISSN 0346-718X

Department of Energy and Environment
Division of Electric Power Engineering
Chalmers University of Technology
SE–412 96 Gothenburg
Sweden
Telephone +46 (0)31–772 1000

Printed by Chalmers Reproservice
Gothenburg, Sweden, 2015

Design and Assessment of HVDC Off-shore Wind Turbine Generator
POOPAK ROSHANFEKR
Department of Energy and Environment
Chalmers University of Technology

Abstract

In this work, design and assessment of a 5 MW wind energy generator with a gearbox is performed to find an energy-efficient generator for HVDC offshore wind turbines, studying an interior permanent magnet synchronous generator (IPMSG) as well as a permanent magnet assisted synchronous reluctance generator (PMa-SynRG). Quantities such as torque density, torque ripple, losses and amount of magnet material are studied. The investigation includes different numbers of air barriers of the PMa-SynRG rotor; up to 6, as well as how to fill the barriers with magnet material, in order to achieve high torque density and low torque ripple. The iron bridge thickness is checked from a mechanical perspective in order to ensure good electromagnetic performance while still keeping the needed mechanical strength. Moreover, the impact of segmenting the magnets and the risk of demagnetization are quantified. Assessing the average annual efficiency using the two generating systems during different average wind conditions shows that when the PMa-SynRG is used, the machine annual energy efficiency is higher. The key reason for this is the lower flux level in the PMa-SynRG which creates lower iron losses at low wind speeds. In addition, the PMa-SynRG has 30% less magnet weight for the same geometrical size and maximum power level.

Index Terms: high voltage direct current (HVDC), wind energy, interior permanent magnet synchronous generator (IPMSG), permanent magnet assisted synchronous reluctance generator (PMa-SynRG), finite element method (FEM), maximum torque per ampere (MTPA), annual energy efficiency.

Acknowledgments

My sincere gratitude goes to my main supervisor, best friend and role model Associate Professor Sonja Tidblad Lundmark for her outstanding guidance and active participation in this work. Without her supervision and help this dissertation would not have been possible. I really appreciate her patience and endless support through those tough and challenging times.

I would also like to thank my co-supervisor Dr. Mikael Alatalo for his valuable inputs. In addition, a thank you to the examiner and assistant supervisor of the project Professor Torbjörn Thiringer for the fruitful discussions.

This work has been funded by the Swedish Energy Agency which is highly appreciated. Financial support from the Erik Feuk fund is also thankfully received.

I would like to express my thanks to all members of the reference group of the off-shore HVDC wind park project, with special gratitude to Dr. Aron Szucs for his great comments and ideas regarding my part of the wind park project.

I am grateful to Jonas Norlin from ANSYS, Sweden and Dr. Håkan Johansson at the division of Dynamics, department of Applied Mechanics Chalmers University of Technology for their help in mechanical analysis.

Special thanks go to Professor Hamid Toliyat in Texas A & M University for giving me the opportunity and honor to work in the Electrical Machines & Power Electronics (EMPE) Laboratory as a visiting scholar. I am not only so grateful to him for giving me this once-in-a-lifetime chance but also for his perfect hospitality during my stay in the USA. I am also thankful to Dr. Yateendra Deshpande for sharing his research, precious knowledge and time with me.

I wish to thank Eva for her support, time and friendship, especially during the stressful and lonely days. I am also very thankful to Annie for doing all the administrative work in the best and fastest possible way.

My deepest gratitude goes to wonderful Adrian for his constant love and kindness. I am very thankful and lucky to have you and your continuous support in my life.

Finally, I would like to thank my family for their support and encouragement over all these years.

Poopak Roshanfekr
Gothenburg, Sweden
October, 2015

List of Abbreviations and Symbols

AC	Alternating Current
HVDC	High Voltage Direct Current
PM	Permanent Magnet
PMSM	Permanent Magnet Synchronous Machine
PMSG	Permanent Magnet Synchronous Generator
SynRM	Synchronous Reluctance Machine
SynRG	Synchronous Reluctance Generator
IPM	Interior Permanent Magnet
IPMSM	Interior Permanent Magnet Synchronous Machine
IPMSG	Interior Permanent Magnet Synchronous Generator
SPMSM	Surface Permanent Magnet Synchronous Machine
SPMSG	Surface Permanent Magnet Synchronous Generator
PMa-SynRM	Permanent Magnet assisted Synchronous Reluctance Machine
PMa-SynRG	Permanent Magnet assisted Synchronous Reluctance Generator
BLDC	Brushless Direct Current
EMSM	Electrically Magnetized Synchronous Machine
MTPA	Maximum Torque Per Ampere
NdFeB	Neodymium Iron Boron
FFT	Fast Fourier Transform
THD	Total Harmonic Distortion
u_{sd}	d-axis stator voltage
u_{sq}	q-axis stator voltage
R_s	Resistance of the stator windings
L_d	d-axis inductance
L_q	q-axis inductance
ω_{el}	Angular velocity of the rotor
I_s	RMS value of stator current
i_s	Peak value of stator current
i_{sd}	d-axis stator current
i_{sq}	q-axis stator current
Ψ_m	Permanent magnet flux linkage
T_e	Electromagnetic torque
γ	Current phase angle

P_{cu}	Copper loss
P_{hy}	Hysteresis loss
P_{ec}	Eddy current loss
P_{magnet}	Permanent magnet loss
ρ	Resistivity
L_m	Magnet length
W_m	Magnet width
l_m	Magnet height
A_c	Magnet area that a circumferential non-segmented magnet eddy current enters
A_z	Magnet area that an axial non-segmented magnet eddy current enters
A_r	Magnet area that a radial non-segmented magnet eddy current enters
A'_c	Magnet area that a circumferential segmented magnet eddy current enters
A'_z	Magnet area that an axial segmented magnet eddy current enters
A'_r	Magnet area that a radial segmented magnet eddy current enters
$R_{NoSegment\_FluxRadial}$	Total resistance of the eddy current paths created by the stator flux in the radial direction for a non-segmented magnet
$R'_{TwoCirSegments\_FluxRadial}$	Total resistance of the eddy current paths created by the stator flux in the radial direction for a magnet segmented into two pieces circumferentially
$R'_{TwoAxialSegments\_FluxRadial}$	Total resistance of the eddy current paths created by the stator flux in the radial direction for a magnet segmented into two pieces axially
$R'_{TwoRadialSegments\_FluxRadial}$	Total resistance of the eddy current paths created by the stator flux in the radial direction for a magnet segmented into two pieces radially
$R_{NoSegment\_FluxCircumferential}$	Total resistance of the eddy current paths created by the stator flux in the circumferential direction for a non-segmented magnet
$R'_{TwoCirSegments\_FluxCircumferential}$	Total resistance of the eddy current paths created by the stator flux in the circumferential direction for a magnet segmented into two pieces circumferentially
$R'_{TwoAxialSegments\_FluxCircumferential}$	Total resistance of the eddy current paths created by the stator flux in the circumferential direction for a magnet segmented into two pieces axially
$R'_{TwoRadialSegments\_FluxCircumferential}$	Total resistance of the eddy current paths created by the stator flux in the circumferential direction for a magnet segmented into two pieces radially

$R_{NoSegment\_FluxAxial}$	Total resistance of the eddy current paths created by the stator flux in the axial direction for a non-segmented magnet
$R'_{TwoCirSegments\_FluxAxial}$	Total resistance of the eddy current paths created by the stator flux in the axial direction for a magnet segmented into two pieces circumferentially
$R'_{TwoAxialSegments\_FluxAxial}$	Total resistance of the eddy current paths created by the stator flux in the axial direction for a magnet segmented into two pieces axially
$R'_{TwoRadialSegments\_FluxAxial}$	Total resistance of the eddy current paths created by the stator flux in the axial direction for a magnet segmented into two pieces radially
B	Magnetic flux density
H	Field intensity
H_{ext}	External magnetic field
B_{max}	Maximum flux density
B_r	Remanence (flux density when $H=0$)
H_c	Coercivity (field intensity when $B=0$)
B_{knee}	Minimum flux density before PM demagnetizes
μ_0	Permeability of air
μ_r	Relative permeability of the material
σ_ν	Von Mises stress
σ_{ii}	Normal stress
σ_{ij}	Shear stress
n_{rotor}	Rotor speed in rpm
f	Frequency
n	Integer number
p	Number of pole pairs
g	Air-gap length
P	Machine power
A_{copper}	Copper area
m	Number of phases
q	Number of slots per pole per phase
τ_p	Pole pitch
τ_s	Slot pitch
N_c	Number of conductors per slot per phase
y	Coil pitch
a	Number of parallel branches
SF_g	Slot fill factor
θ	Angle that the magnet covers on the surface of the rotor (polar arc)
α	Magnet coverage
W_s	Slot pitch normalized to the pole pitch
W_t	Tooth width normalized to the pole pitch

I_{sc}	Short-circuit current
$f(\omega)$	Probability of having wind speed ω during one year
$p(\omega)$	Losses as a function of the wind speed
E_{loss}	Loss annual energy
E_{mec}	Mechanical annual energy
E	Annual energy efficiency

Contents

Chapter 1

Introduction

1.1 Background and motivation

Wind energy is one of the most promising clean energy sources and its penetration has been increasing throughout the world during the last years [1], [2], [3], [4] and [5]. The expansion of wind power takes place both on land (on-shore) and at sea (off-shore). However, so far wind turbines are mainly erected on land [6]. Problems with finding suitable places to install wind farms on land and the existence of huge fairly shallow areas in the North Sea and the Baltic Sea where off-shore wind farms can be located, has prompted a great interest in placing off-shore wind farms, which is also advantageous because average wind speed is much higher off-shore compared to on-shore.

For large off-shore wind farms with a long distance to the shore, High Voltage Direct Current (HVDC) transmission offers technical and economical advantages in comparison with Alternating Current (AC) connections [7]-[8]. An example of a wind farm using a dc-transmission system is a wind park at Borkum (Borwin1) . Figure 1.1 shows the generating and transmission system used in Borkum. Even though a dc-transmission is used for the Borkum wind farm, still 50/60 Hz technology, for instance bulky 50/60 Hz transformers are used within the park. A future possibility for off-shore wind farms could be a completely dc-based system, comprising of a dc collection grid, a dc-transmission line and dc/dc converters as seen in Fig. 1.2. In this case the need for heavy and large platforms is reduced.

The same as for on-shore wind farms, in off-shore wind turbines, a collection voltage of 33-36 kV seems to be the most cost-effective solution [9], since the size and cost of the transformer are increased for higher voltage levels. In future off-shore wind farms (see Fig. 1.2) if a high frequency dc/dc transformer is used instead of a 50/60 Hz transformer, higher voltage level can be used in order to minimize the power losses. Therefore, a dc voltage level of 40-70 kV for the energy transportation to the collection point could be appropriate. This voltage is by far too high to operate the wind turbine generator directly from (according to [10], the most common voltage levels for generators up to 3 MW is from 660 to 750 V, with 690 V being most common and for generators over 3 MW it is between 3.1-6.6 kV, with 3.3 kV being most common). Thus, a dc/dc converter is needed to boost the voltage. The use of a dc/dc converter also makes the

choice of a suitable dc-link voltage for the generating system fairly free.

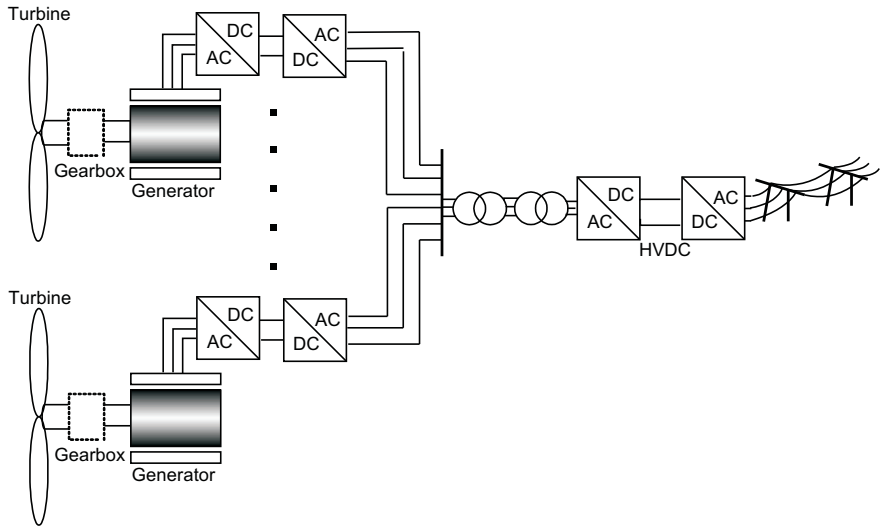

Fig. 1.1 Generator and transmission system in the Borkum wind farm.

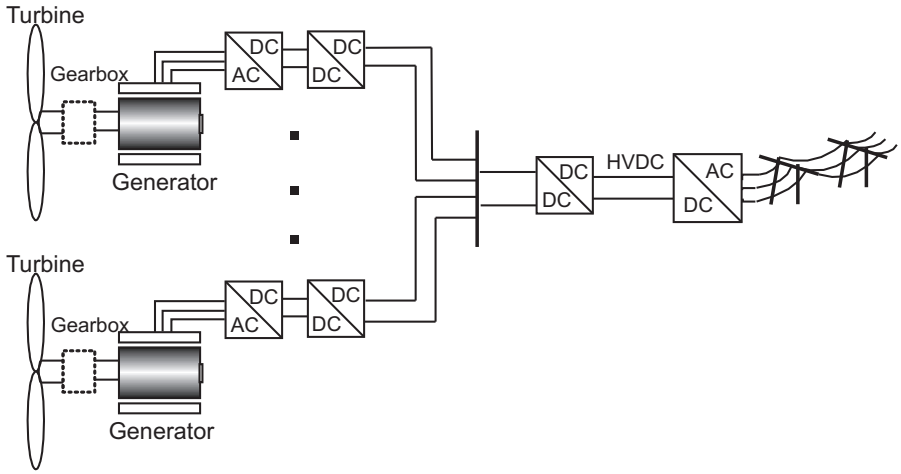

Fig. 1.2 Generator and transmission system in the future remote off-shore wind farms.

Permanent magnet synchronous generators (PMSGs) are popular in wind turbine application, since they have high torque density and high efficiency. One of the most used permanent magnet material in MW wind generators is the type of rare-earth magnet based on Neodymium Iron Boron (NdFeB). This material can be expensive and therefore, it is important to use as little material as possible and to make the best use of the material. Usually, it is not economical to recycle this material after the end of life of a machine with NdFeB magnets [11]. Although, due to the increased cost of the magnets there are investigations in the area of recycling, see for example [12].

Synchronous reluctance generators (SynRGs) can be an interesting option for wind applications [13], since they are robust, inexpensive and they have a simple rotor construction. Moreover,

SynRGs have low noise emission and are suitable for variable speed operation [14]. However, they have a lower power factor compared to PMSGs.

The magnets in a PMSM can be placed on the surface or inside the rotor (surface and interior permanent magnet synchronous machine). By placing the magnets inside the rotor (IPMSM), the machine utilizes both the torque produced from the interaction of magnet and stator winding flux (alignment torque or simply magnet torque) as well as the reluctance torque. An IPMSM generates flux concentration in the rotor that can allow thinner magnets [15] and they have demagnetization protection. However, the pole number in an IPMSM may be limited due to finite space in the rotor, and the magnet flux leakage is relatively high as well [16]. On the other hand, surface permanent magnet synchronous machines (SPMSM) can more easily have a lower torque ripple. But they also have high magnet losses and risk of demagnetization [17]. A comparison of interior and surface permanent magnet machines for traction purposes has been done in [18] in terms of power density, electrical efficiencies, losses and torque. Design strategies for large-scale v-shape IPM and SPM wind generators are introduced and their performances are compared in [16].

In IPMSMs usually one layer of magnet (single-layer IPMSM) is placed inside the rotor which is easy to manufacture [19], however, the reluctance torque contribution is moderate, since the saliency is small. Therefore, most of the developed torque originates from the rare-earth permanent magnets which can make them costly due to the high amount of needed magnet material. The magnets can be placed in two or more layers, creating a multi-layer rotor structure. In this way, the contribution of reluctance torque will be increased and the amount of used magnet material could be smaller compared to single-layer PMSMs. In [20], a single-layer IPMSM is compared to a double-layer IPMSM and it is shown that increasing layers in the rotor of an IPM motor is an effective way to improve the torque density performance of the IPMSM without adding more permanent magnets. A double-layer IPMSM can also be effective to reduce torque ripple and cogging torque compared to a single-layer IPMSM [21]. A multi-layer PMSM can also be called a permanent magnet assisted synchronous reluctance machine (PMa-SynRM) which can be employed in a wide range of applications [22], [23] and [24]. A PMa-SynRM has a higher power factor compared to a SynRM and like the SynRM can have lower cost in comparison with the other PM machines. Therefore, it can be an interesting option to use in a wind turbine generating system, and the topic is worthy of further research.

In IPMSMs and PMa-SynRMs the iron bridge thickness is an important parameter, since decreasing the thickness of the bridge will increase the air-gap flux density due to saturation of the iron bridges and therefore a higher torque can be obtained from that machine. However, due to the mechanical strength, this parameter cannot be chosen to be very small. In [25] and [26], the importance of the investigation of this parameter at maximum speed for mechanical robustness is discussed. However, the change of the performance of the machine versus iron bridge thickness is not investigated. Also missing in literature is a comparison of different wind generating systems from an energy efficiency point of view.

1.2 Purpose of the thesis and main contributions

The aim of this thesis is to investigate different generators for off-shore wind turbines with HVDC connections which is shown in Fig. 1.2. Main aspects are to study energy efficiencies and weight of the generators.

This work is the continuation of a licentiate thesis [1], see [27]. In [27] which focuses on energy-efficient generating systems for HVDC off-shore wind turbines, a surface and an interior mounted permanent magnet synchronous generator as well as a synchronous reluctance generator with an active transistor converter have been studied. For the machine losses, iron and copper losses have been considered. The main contribution of the half way reporting [27] are:

- Determination of the power density and annual energy efficiency performance for two PMSMGs, with the same main dimensions, with magnets placed on the surface and inside the rotor.
- Investigation of the power density of a synchronous reluctance wind generator in relation to a permanent magnet synchronous generator.
- Comparative studies on the machine annual energy efficiency for a wind turbine consisting of a permanent magnet synchronous machine with a wind turbine comprising of a synchronous reluctance machine for various average wind speeds.
- Establishing an ideal dc-link voltage for a given wind generator.
- Quantify the losses for a two-level wind energy converter using IGBT modules with various rated voltages.

In this work, a purpose in addition to the investigation performed in [27], is to investigate a PMa-SynRG, since as was mentioned, it can be an option to use in a wind turbine generating system. Moreover, an objective is to include mechanical stress calculations for both the PMa-SynRG as well as the IPMSG. Furthermore, a goal is to also include the magnet losses of the machines.

To the best of the author's knowledge, the additional contributions are thus:

- A design suggestion of an IPMSG and a PMa-SynRG with the mechanical restriction of the rotor iron bridges included.
- A quantification of the importance of segmenting the magnets in various directions.
- An energy efficiency and weight comparison of the suggested 5 MW PMa-SynRG with the IPMSG.

[1] In Sweden in between the Master thesis and PhD thesis there is a half way reporting, licentiate thesis, which constitute a part of the PhD thesis.

1.3 List of publications

The publications originating from the project are:

I. P. Roshanfekr, T. Thiringer, S. Lundmark , M. Alatalo , "DC-link Voltage Selection for a Multi-MW Wind Turbine", *COMPEL: The International Journal for Computation and Mathematics in Electrical and Electronic Engineering*, Vol. 33 Issue: 5, pp.1722-1740.

II. P. Roshanfekr, S. Lundmark, T. Thiringer, M. Alatalo, M., "Improving the performance of a 5 MW interior permanent magnet generator for wind application by increasing the layers," submitted to IET Electric Power Application journal.

III. P. Roshanfekr, S. Lundmark, T. Thiringer, M. Alatalo, "Comparison of a 5 MW Permanent Magnet Assisted Synchronous Reluctance Generator with an IPMSG for Wind Application," *Electrical Machines (ICEM), XXIth International Conference on*, SEP. 2014, Berlin, Germany.

IV. P. Roshanfer, S. Lundmark, T. Thiringer, M. Alatalo, "Torque ripple reduction methods for an interior permanent magnet synchronous generator," *Power Electronics and Applications (EPE'14-ECCE Europe), 16th European Conference on*, pp.1-7, 26-28 Aug. 2014, Lappeenranta, Finland.

V. P. Roshanfekr, S. Lundmark, T. Thiringer, M. Alatalo, "Effect of Magnet Coverage on Torque, Loss and Torque Ripple in a PMSM," *IECON 40th Annual Conference on IEEE Industrial Electronics Society*, 29 Oct-1 Nov. 2014, Dallas, USA.

VI. P. Roshanfekr, S. Lundmark, T. Thiringer, M. Alatalo, "A Synchronous Reluctance Generator for a Wind Application-compared with an Interior Mounted Permanent Magnet Synchronous Generator," *Power Electronics, Machines and Drives (PEMD 2014), 7th IET International Conference On*, pp.1,5, 8-10 April 2014, Manchester, UK.

VII. S. Lundmark, P. Roshanfekr, "Magnet and core loss in a radial flux and a transverse flux PM traction motor," *Ecological Vehicles and Renewable Energies (EVER), Tenth International Conference on*, pp.1,9, March 31 2015-April 2 2015.

VIII. P. Roshanfekr, T. Thiringer and S. Lundmark, "Efficiency comparison of a 5 MW wind turbine PMSG-equipped generating system using various dc-link voltages," in *Electrical Vehicles and Renewable Energies (EVER) Conference on*, March 2012.

IX. P. Roshanfekr, T. Thiringer , M. Alatalo and S. Lundmark, "Performance of two 5 MW permanent magnet wind turbine generators using surface mounted and interior mounted magnets," in *Electrical Machines (ICEM), 2012 XXth IEEE International Conference on*, 2012, pp. 1041-1047.

X. P. Roshanfekr, T. Thiringer , S. Lundmark and M. Alatalo, "Selecting IGBT module for a high voltage 5 MW wind turbine PMSG-equipped generating system," in *Power Electronics and Machines in Wind Applications (PEMWA), 2012 IEEE*, 2012, pp.1-6.

XI. Roshanfekr, P. "Energy-efficient Generating System for HVDC Off-shore Wind Turbine," Licentiate Thesis, Chalmers University of Technology, Department of Electric Power Engineering, Göteborg, Sweden, October 2013.

Chapter 2

Turbine generator theory

2.1 Permanent magnet synchronous machine (PMSM)

The Permanent Magnet Synchronous Machine is here considered to be a polyphase AC motor with rotor mounted permanent magnets and sinusoidal distribution of the stator phase windings as well as fed with sinusoidal currents (thus the brushless dc permanent magnet machine, BLDC, is not considered here). The permanent magnets provide the field excitation in the machine.

By having the magnets in the rotor instead of field windings, the electrical losses of the machine are reduced and the absence of mechanical components such as slip rings and brushes make the machine lighter.

Compared to induction motors in which the stator current contains magnetizing as well as torque-producing components, the use of the permanent magnets in the rotor of permanent magnet machines makes it unnecessary to supply magnetizing current through the stator to obtain constant air-gap flux, so the stator current is mainly used to produce torque. Therefore, for the same output, the PMSM will operate at a higher power factor and it will be more efficient than the induction machine.

The PMSMs have a wide range of applications. E.g. the application of PM servo motors fed from static inverters is increasing [28]. The PMSM can be used in large power synchronous motors rated more than 1 MW. Large PMSMs can be used both in low speed drives as well as high speed drives.

2.1.1 Cons and pros of PMSM

The use of permanent magnets in construction of electrical machines brings the followings advantages:

- The magnetic field is provided by the permanent magnet and there is no need for additional DC supply for magnetization (excitation circuit). Therefore, without slip rings, and

brushes the machine becomes robust and maintenance free.

- The efficiency of the PMSM in comparison with an Electrically Magnetized Synchronous Machine (EMSM) is higher since the rotor copper losses disappear as there is no rotor winding.
- Higher torque to weight ratio compared to other AC machines.
- Better dynamic performance than the electrically magnetized synchronous machines [28].

However, the PMSM has some disadvantages:

- At high temperature or at powerful magnetic fields inside a generator, the permanent magnets could be demagnetized (although this is rarely a problem today) [29].
- Difficulties for transportation and security in delivery as well as high cost of permanent magnet material.

2.1.2 Construction of PMSM

The magnets of the permanent magnet machines can be placed in different parts of the rotor. The most common rotor configurations of the permanent magnet synchronous machines which are shown in Fig. 2.1 are:

- Surface mounted magnet rotor (Fig. 2.1(a)).
- Interior mounted magnet rotor (Fig. 2.1(b)).
- Inset mounted magnet rotor (Fig. 2.1(c)).

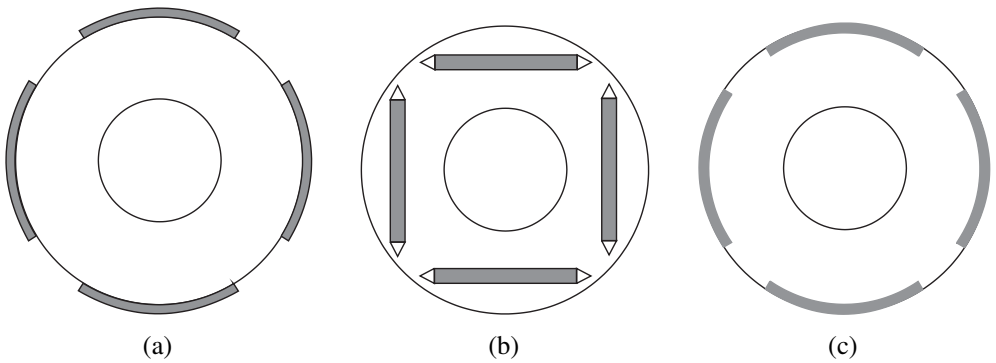

Figure 2.1: Rotor configurations for PMSM; (a) surface mounted magnet, (b) interior mounted magnet, (c) inset mounted magnet.

Surface mounted permanent magnet synchronous machines can more easily have a lower torque ripple while interior and inset mounted permanent magnet synchronous machines on the other hand generate flux concentration in the rotor that can allow thinner or weaker magnets [15]. Interior and inset mounted permanent magnet synchronous machines have unequal direct and quadrature inductance which produces a reluctance torque in addition to the magnet torque. Interior mounted permanent magnet machines more easily have robustness against magnet demagnetization. However, the vibration and noise production in surface mounted permanent magnet synchronous machines is less than in interior permanent magnet machines [30].

2.1.3 Dynamic model of PMSM

According to [31] the mathematical model of a PMSM in the dq synchronously rotating reference frame for assumed sinusoidal stator excitation is

$$u_{sd} = R_s i_{sd} + L_d \frac{i_{sd}}{dt} - \omega_{el} L_q i_{sq} \tag{2.1}$$

$$u_{sq} = R_s i_{sq} + L_q \frac{i_{sq}}{dt} + \omega_{el} L_d i_{sd} + \omega_{el} \Psi_m \tag{2.2}$$

$$T_e = \frac{3}{2} p[\Psi_m i_{sq} + (L_d - L_q) i_{sq} i_{sd}] \tag{2.3}$$

where u_{sd} and u_{sq} are d- and q-axis stator voltages, R_s is the resistance of the stator windings, L_d and L_q are d- and q- axis inductances, ω_{el} is the angular velocity of the rotor, i_{sd} and i_{sq} are d- and q-axis stator currents, Ψ_m is the permanent magnet flux linkage, T_e is the electromagnetic torque and *p* is the number of pole pairs.

As can be seen in (2.3), in PMSMs the torque consists of two terms. The first term is called alignment torque (or magnet torque) and the second term is called reluctance torque.

Based on (2.1) and (2.2) the equivalent circuit of a PMSM can be obtained. See Fig. 2.2.

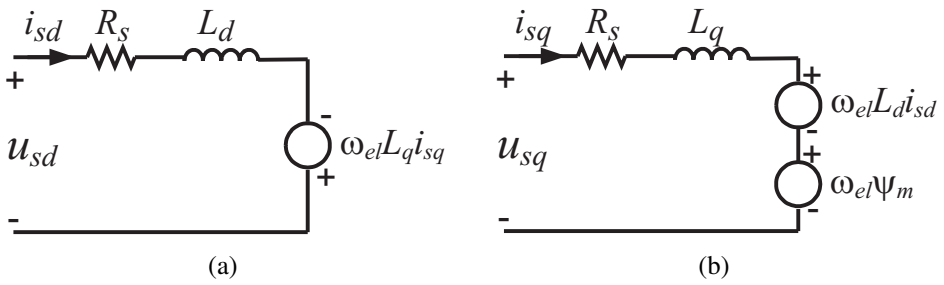

Figure 2.2: Equivalent circuit of a PMSM; (a) d-axis circuit, (b) q-axis circuit [31].

In steady state (2.1) and (2.2) become

$$u_{sd} = R_s i_{sd} - \omega_{el} L_q i_{sq} \tag{2.4}$$

$$u_{sq} = R_s i_{sq} + \omega_{el} L_d i_{sd} + \omega_{el} \Psi_m \tag{2.5}$$

2.1.4 Operation of PMSM

In interior permanent magnet synchronous machines, $L_q > L_d$, so to have both terms in the same direction, the stator current (i_s) should be in the second quadrant (Q_2) for the motoring mode and in the third quadrant (Q_3) for the generating mode.

For constant current using the phasor diagram given in Fig. 2.3 and noting that γ (the current phase angle) is measured from the q-axis in the positive (anticlockwise) direction in the phasor diagram, the d- and q-axis currents can be written

$$i_{sd} = -i_s \sin\gamma; \;\; i_{sq} = i_s \cos\gamma \tag{2.6}$$

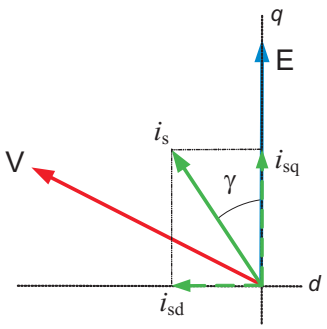

Figure 2.3: Phasor diagram for motoring mode.

2.1.5 MTPA control strategy

There are several control strategies to improve the performance and reduce the losses of a PMSM [32]. The copper losses can be minimized by the Maximum Torque Per Ampere (MTPA) control strategy which consequently increases the efficiency [33]. For this control method there must be a sufficient voltage from the inverter to be able to have the current which is needed to obtain the desired torque. When the converter voltage is limited, there might be a need of more negative i_{sd} current to achieve the desired torque, since the voltage required to get MTPA is not sufficient from the converter. This is known as flux weakening. In [34], it is shown that the voltage limits are in the shape of ellipses in an id/iq-diagram and these ellipses shrink as the speed increases. The reason for this is that the back-emf is high at high speeds, and according to (2.4) and (2.5), there is less voltage available for achieving the initially desired current. Figure 2.4 shows the voltage limit ellipses for different speeds, as well as a desired operating point. The green curve represents the MTPA operating points. As can be seen, when the speed is low (blue voltage limit ellipse), the desired torque using MTPA is possible. However, as the speed increases (red and purple voltage limit ellipses) a more negative *d* current and also a

higher current is needed to obtain the desired torque. The torque is determined using (2.3). In this thesis this type of control is used to control the generators.

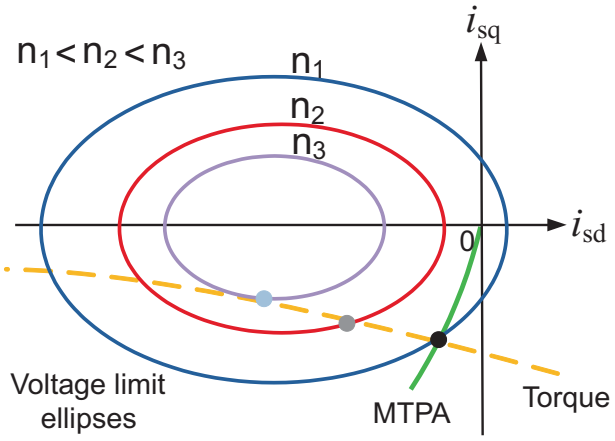

Figure 2.4: Voltage limits and MTPA curves for a generator.

MTPA operation of IPMSG

The voltage limits ellipses, the MTPA line (green line) and the torque lines for an IPMSG are shown in Fig. 2.5. From the figure it can be seen that when the speed is low and the voltage limit is the blue ellipse, all the torques in Fig. 2.5 are achievable using MTPA, since the MTPA line is inside this voltage limit. When speed increases and the voltage limit is the red ellipse, it is possible to achieve T_1 at MPTA operation. However, to achieve T_2 and T_3 we need to follow the gray line. If the speed increases more and the voltage limit is the purple ellipse, to achieve T_1, T_2 and T_3 we need to follow the black line. Therefore, more current is needed to obtain the required torque compared to the MTPA case.

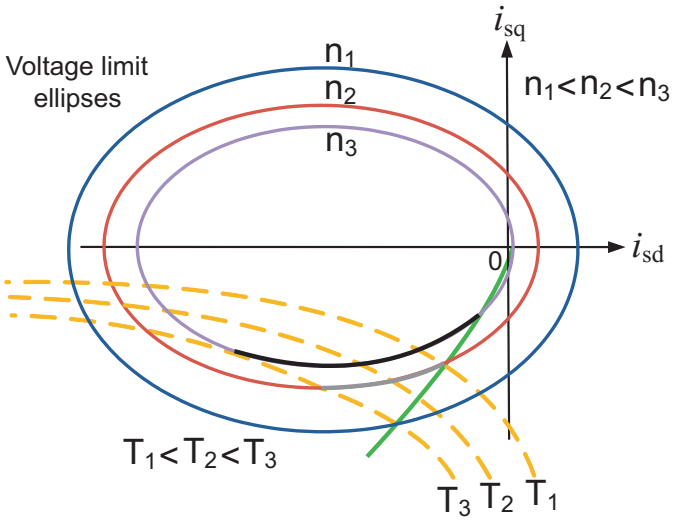

Figure 2.5: Voltage limits, MTPA and torques curves for an IPMSG.

2.2 Permanent magnet assisted synchronous reluctance machine (PMa-SynRM)

In IPMSMs usually one layer of magnet (single-layer IPMSM) is placed inside the rotor which is easy to manufacture [19], however, the reluctance torque contribution is moderate, since the saliency ratio is small. Therefore, most of the developed torque originates from the rare-earth permanent magnets which can make them costly due to the high amount of needed magnet material. The magnets can also be placed in two or more layers, creating a multi-layer rotor structure. In this way, the contribution of reluctance torque will be increased and the amount of used magnet material could be smaller compared to single-layer IPMSMs. A double-layer PMSM can also be effective to reduce torque ripple and cogging torque compared to a single-layer IPMSM [21]. A multi-layer IPMSM can also be called a permanent magnet assisted synchronous reluctance machine (PMa-SynRM), since the machine is similar to an IPM machine, however, the reluctance torque has the most contribution in the developed torque [35], [36] and [37]. PMa-SynRMs can be employed in a wide range of applications [22], [23] and [24]. A PMa-SynRM has a higher power factor capability compared to a SynRM and like the SynRM can have lower cost in comparison with the other PM machines.

The amount of magnet material used, the choice of magnet material as well as the position of the magnets vary widely for different types of PMa-SynRGs. In some versions, the magnets are used to decrease the q-axis flux [38] and [39] (see Fig. 2.7), and in some designs the magnets are used to increase the d-axis flux. A schematic picture as well as the d- and q-axis of the machine with permanent magnets placed to increase the d-axis flux are shown in Fig. 2.6.

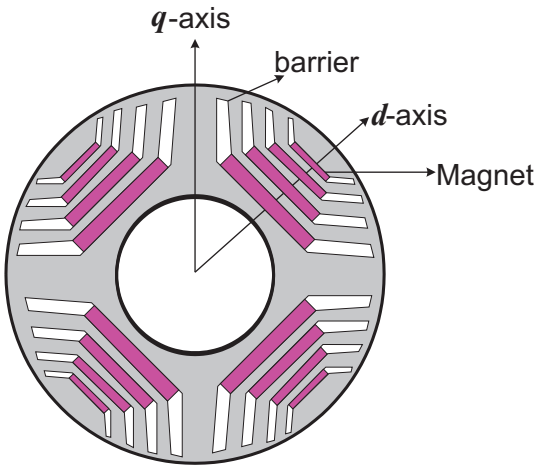

Fig. 2.6 d- and q-axis in a PMa-SynRM. Magnets are included in the d-axis flux path.

In [25], the placement of magnets along the q-axis is compared to the same magnet volume placed along the d-axis. It is shown that the torque ripple is significantly higher when the magnets are placed along the q-axis. Therefore, in this thesis, the magnets are placed to increase the d-axis flux. When permanent magnets are included in the d-axis flux path as in Fig. 2.6, (2.3) can be used to calculate the electromagnetic torque. However, if the permanent magnets are placed in the direction of counteracting q-axis flux as shown in Fig. 2.7 , the torque is formed

[38] as

$$T_e = \frac{3}{2} p[\Psi_m i_{sd} + (L_d - L_q) i_{sq} i_{sd}] \tag{2.7}$$

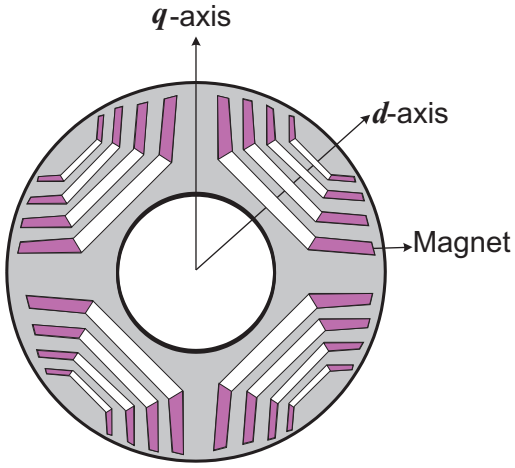

Fig. 2.7 Magnets are placed along the q-axis in a PMa-SynRM.

The rotor of a conventionally (also referred to as transversally of radially) laminated PMa-SynRM must have tangential bridges to hold the whole structure of the lamination together. Radial bridges might also be needed to support the structure of the rotor when the machine is used for high speed applications [40]. Tangential and radial bridges are shown in Fig. 2.8.

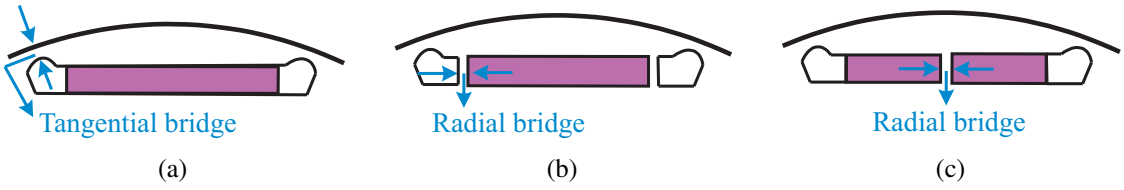

Fig. 2.8 Tangential and radial bridge in a PMa-SynRM; (a) Tangential bridge, (b) Radial bridge on the sides of the magnet, (c) Radial bridge in the middle.

If the magnet is placed in the d-axis flux path, the radial bridges can be placed either besides the magnets as in [41] (see Fig. 2.8(b)) or in the middle of the d-axis as in [42] (see Fig. 2.8(c)). From mechanical forces point of view, the weakest parts in a PMa-SynRM rotor are tangential and radial bridges [35], since centrifugal force is concentrated locally in the bridges [43]. Therefore, iron bridges should be chosen thick enough to withstand the mechanical stresses caused by centrifugal force and torque [44]. On the other hand, a thinner tangential and radial bridge will result in a better electromagnetic performance due to less flux leakage [45], [46] and [25]. Therefore, the iron bridge thickness is an important parameter in PMa-SynRMs. In Section 2.5, the influence of mechanical stress on the iron bridge of the rotor is more explained.

2.3 Copper and core loss

The copper losses are calculated according to

$$P_{cu} = 3R_s \left|I_s\right|^2 \tag{2.8}$$

where P_{cu} is the copper loss, R_s is the armature phase resistance and $|I_s|$ is the RMS magnitude value of the phase current.

Core loss is mainly consisting of hysteresis loss and eddy current loss. Hysteresis loss is due to the materials unwillingness to change its magnetic state; the larger the area of the hysteresis loop, the larger the loss is. Hysteresis loss also depends on the frequency; the higher the frequency, the more times the hysteresis loop is ran through, and the higher is the loss. Hysteresis loss can be reduced by annealing which means a heat-treatment of the material with high temperatures of $\approx 1000\,^{\circ}\mathrm{C}$ [47]. The hysteresis loss may be calculated with the formula

$$P_{hy} = K_{hy} f B^{\beta}\ \mathrm{W/m^3} \tag{2.9}$$

where k_{hy} and β are constants (β =1.6-2.4) which depend on the magnetic properties of the material.

In a similar way, the eddy current loss may be calculated with

$$P_{ec} = K_{ec} f B^2\ \mathrm{W/m^3} \tag{2.10}$$

where k_{ec} is a constant that depends on the magnetic properties of the material but it also varies with lamination thickness. Common values of lamination thickness are 0.35 to 0.65 mm [47], but thinner ones exist, like 0.27 mm and even 0.1 mm. For thicker laminations, the constant k_{ec} is higher and consequently, the eddy current loss is higher.

Core loss is difficult to measure as it is difficult to separate core loss and mechanical loss. It is also difficult to calculate the core loss. Empirical formulas, like (2.9) and (2.10) can be used but then we have to know not only values of the constants but also values of the flux density and the frequency. The flux density may vary inside the core parts, and the flux wave also contains harmonics. So, often calculations of the core loss are very approximate. An alternative is to do FEM calculations in order to find proper values of *B* for each element, and then calculate the core loss for each element and frequency using either (2.9) and (2.10), or graphs from the manufacturer showing core loss per weight, as seen in Fig. 2.9.

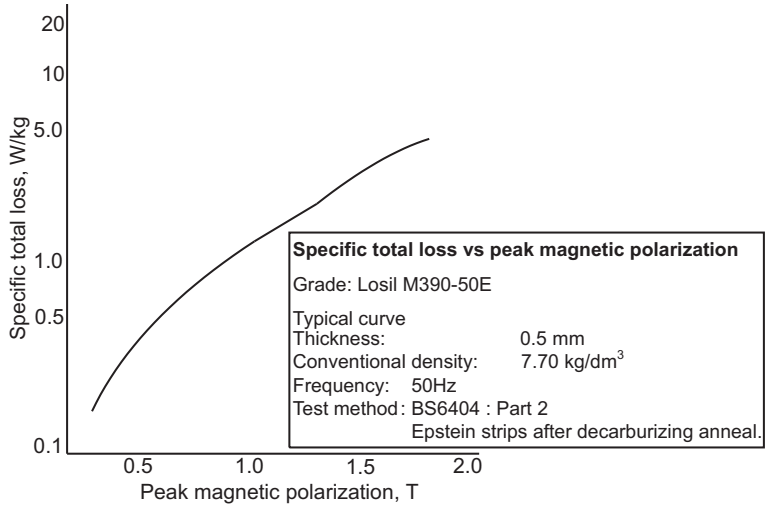

Figure 2.9: Loss curve showing core loss per weight for different flux densities at 50 Hz, for the material Losil M340-50E, where E stands for alloyed steel and the rest of the name implies that it has a guaranteed loss value of 3.4 W/kg at 1.5 T, and 50 Hz, being 0.5 mm thick [47].

This procedure will anyway give only an estimate of the core loss considering that electrical steels are tested and graded under pure sinusoidal conditions. These ideal conditions hardly represent the magnetising conditions in an electric machine. As the presence of flux harmonics increases the core losses of electrical steels, it is likely that the calculated loss will be lower than the actual core loss.

In this work, to calculate the core losses, for each wind speed the core losses are taken from Maxwell. Information about how the core loss calculation is done in Maxwell can be found in [48]. In [49], it is shown that for kW machines, the cutting influence on iron losses are significant, and therefore this will increase the iron losses given in the material catalogue. However, in MW machines, the cutting influence is of minor importance and the loss data provided in the manufacturer's catalogue can be assumed to be accurate. Since in this work 5 MW generators are investigated, the iron losses taken from Maxwell are assumed to be good enough.

2.4 Magnet loss and demagnetization

The eddy current losses in the rotor magnet of high-speed and large permanent magnet machines can be considerable. Therefore, predicting magnet losses can be important in order to avoid thermal stress and demagnetization [50] and [51].

The eddy currents produced in the rotor permanent magnets are caused by the stator flux harmonics (time harmonics due to the non-sinusoidal stator currents and space harmonics due to stator slots) [52], [53], [54] and [55]. There are different ways to reduce the magnet losses.

- Placing the magnets away from the air-gap, since the magnets close to the surface of the rotor core have higher eddy currents than magnets buried deeper [56].

- Using a magnet material with lower conductivity as suggested in [53] and [56]. For example, ferrite magnets instead of NdFeB magnets.
- Insulating the permanent magnets [53].
- Segmenting the magnets.

However, if the skin effect is not negligible (skin depth is not greater than both magnet width and magnet radial height), permanent magnet segmentation may lead to an increase rather than a reduction of the eddy current losses. In [50], this is called the anomaly of segmentation. The anomaly with respect to axial segmentation for interior permanent magnet motors is shown in [57]. It is concluded that the axial length of the divided magnet of the interior permanent magnet motor should be smaller than twice of the skin depth of the eddy currents produced by the major harmonic field for an effective loss reduction.

There are three different ways to represent the eddy currents in magnets which are explained in [56]. In this work, the method when eddy currents are circulating in the magnets is used, see Fig. 2.10. For this method a 3D model is needed.

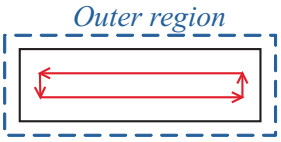

Fig. 2.10 Model of eddy currents in magnet.

Magnet segmentation should be done in a direction that limits eddy currents but not magnet flux. Segmentation makes the paths of the eddy currents longer, and decreases the available cross section area for the eddy currents, thus increasing the resistance and thereby reducing the induced eddy currents. The eddy current loss is proportional to the resistance and the square of the current, so the loss will be reduced due to the segmentation [56]. Or one can also say that the eddy current loss is proportional to the square of the induced voltage and inversely proportional to the resistance, since the resistance increases by segmenting the magnet, and accordingly the loss will be reduced.

A magnet can be segmented in the circumferential, axial and radial direction. However, in a radial flux machine the radial segmentation might add to the effective air-gap, and is thus to be avoided (in transverse flux machine, magnets are magnetized axially, thus radial segmentation does not add to the effective air-gap.). In [58], [59] and [60], the effect of circumferential and axial segmentation of permanent magnets on the rotor loss in different machines is investigated.

In the next sections, the effect of different type of magnet segmentations regarding the direction of the stator flux is investigated. The derivation of the formulas can be found in Appendix A.

2.4.1 Stator flux in the radial direction

If the stator flux is entering the magnet in the radial direction which is shown in Fig. 2.11, it creates eddy currents in the circumferential and axial direction (the red paths in Fig. 2.11(a)).

These eddy current paths have resistances that are shown in Fig. 2.11(b).

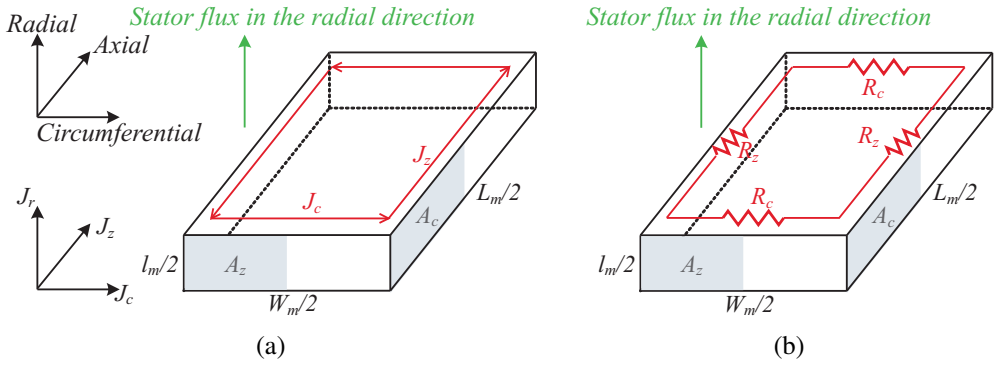

Fig. 2.11 The stator flux is in the radial direction; (a) The eddy current paths are in the circumferential and axial direction, (b) Resistances of the eddy current paths.

The total resistance of the eddy current paths created by the stator flux in the radial direction is

$$R_{NoSegment\_FluxRadial} = \rho \left(\frac{W_m}{A_c} + \frac{L_m}{A_z} \right) \tag{2.11}$$

Circumferentially segmented

If the stator flux is in the radial direction and the magnet is segmented in the circumferential direction then there will be two closed eddy current paths that are shown in Fig. 2.12(a). Each of these closed eddy current paths include two eddy current paths in the circumferential and two paths in the axial direction. The resistances of the eddy current paths are illustrated in Fig. 2.12(b).

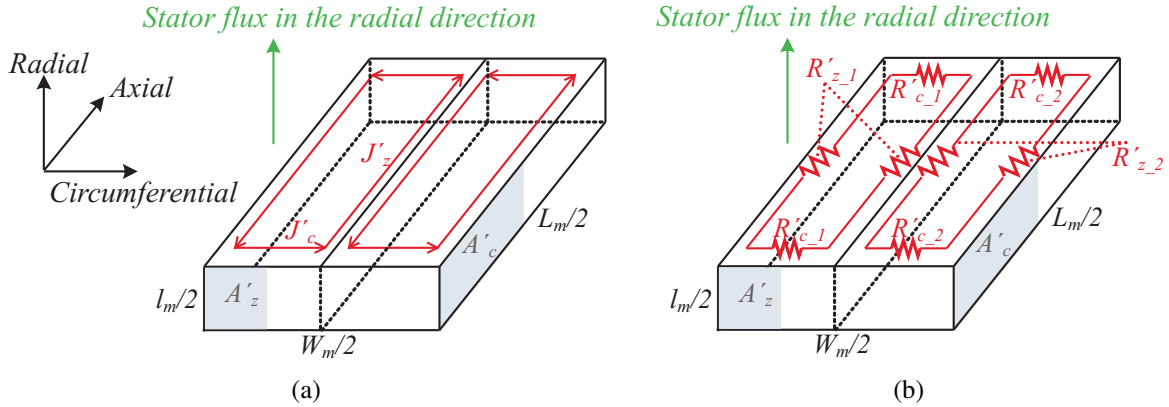

Fig. 2.12 Stator flux in the radial direction for a magnet segmented circumferentially into two; (a) The eddy current paths, (b) Resistances of the eddy current paths.

The total resistance of the two magnet segments is

$$R'_{TwoCirSegments\_FluxRadial} = \rho\left(\frac{W_m}{A_c} + \frac{4L_m}{A_z}\right) \tag{2.12}$$

As can be seen from (2.12) and (2.11), the total resistance of the segmented magnet has increased compared to the total resistance of the non-segmented magnet. Therefore, the magnet losses will decrease.

Axially segmented

The stator flux is kept in the radial direction but the magnet is segmented in the axial direction as shown in Fig. 2.13(a).

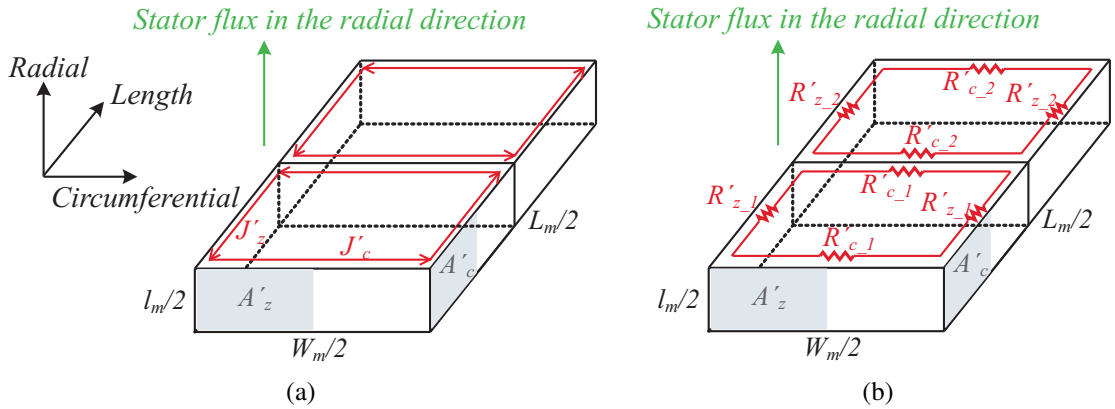

Fig. 2.13 Stator flux in the radial direction for a magnet segmented axially into two; (a) The eddy current paths, (b) Resistances of the eddy current paths.

The total resistance of the two magnet segments is

$$R'_{TwoAxialSegments\_FluxRadial} = \rho\left(\frac{4W_m}{A_c} + \frac{L_m}{A_z}\right) \tag{2.13}$$

Comparing (2.13) and (2.11), it can be seen that axial segmentation is also effective to decrease magnet loss, if the stator flux is in the radial direction.

Radially segmented

The stator flux is still kept in the radial direction but the magnet is segmented in the radial direction as shown in Fig. 2.14.

The total resistance of the two magnet segments is

$$R'_{TwoRadialSegments\_FluxRadial} = \rho\left(\frac{W_m}{A_c} + \frac{L_m}{A_z}\right) = R_{NoSegmentFlux\_Radial} \tag{2.14}$$

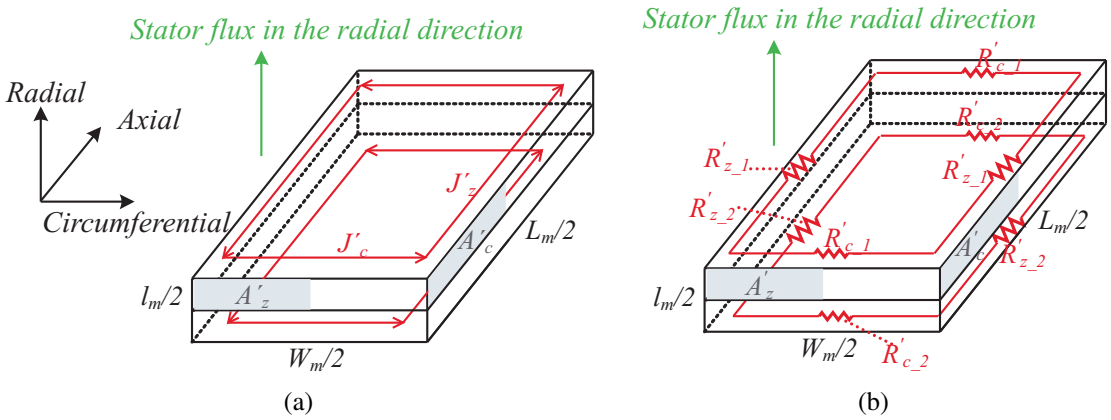

Fig. 2.14 Stator flux in the radial direction for a magnet segmented radially into two; (a) The eddy current paths, (b) Resistances of the eddy current paths.

As can be seen in (2.14), the radial segmentation is not effective at all. The radial segmentation also adds to the effective air-gap, decreasing the output performance. Still, for the radial segmentation, the most loss is in the upper segment that is closest to the stator flux. Therefore, the losses potentially decreases slightly.

2.4.2 Stator flux in the circumferential direction

If the stator flux is in the circumferential direction (see Fig. 2.15), it creates eddy currents in the radial and axial direction (the red paths in Fig. 2.15(a)). The resistances of these eddy current paths are shown in Fig. 2.15(b).

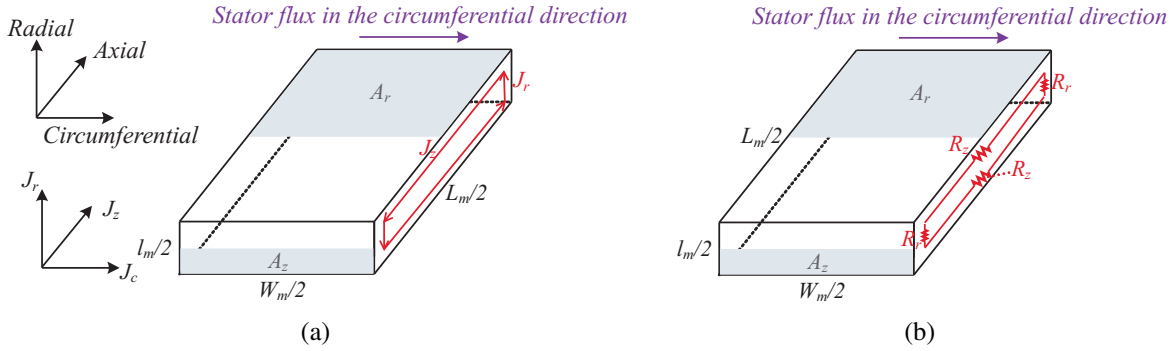

Fig. 2.15 Stator flux in the circumferential direction; (a) The magnet eddy current paths are in the radial and axial direction, (b) Resistances of the eddy current paths.

The total resistance of the eddy current paths created by the stator flux in the circumferential direction is

$$R_{NoSegment\_FluxCircumferential} = \rho \left(\frac{l_m}{A_r} + \frac{L_m}{A_z} \right) \tag{2.15}$$

Circumferentially segmented

If the stator flux is in the circumferential direction and the magnet is also segmented in the circumferential direction, the two closed eddy current paths (red loops) that are shown in Fig. 2.16(a) consist of paths in the radial and axial directions. The resistances of the eddy current paths are shown in Fig. 2.16(b).

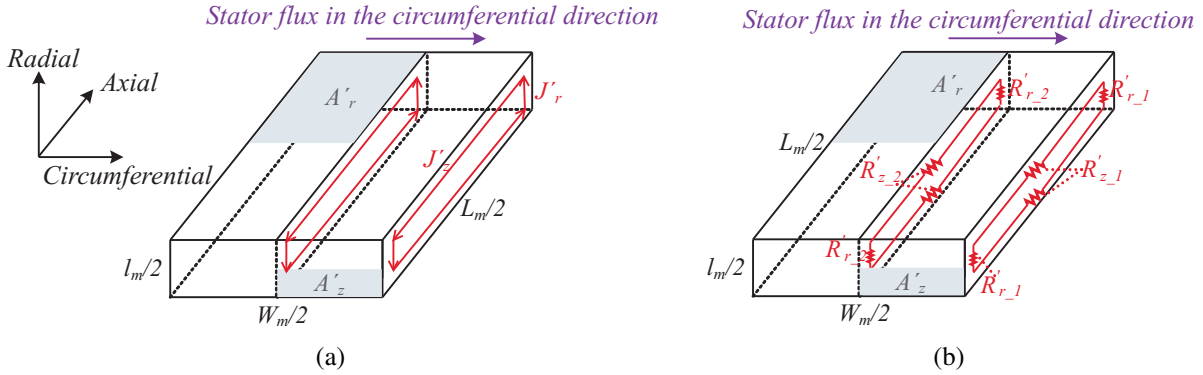

Fig. 2.16 Stator flux in the circumferential direction for a magnet segmented circumferentially into two; (a) The eddy current paths, (b) Resistances of the eddy current paths.

The total resistance of the two magnet segments is

$$R'_{TwoCirSegments\_FluxCircumferential} = \rho\left(\frac{W_m}{A_c} + \frac{L_m}{A_z}\right) = R_{NoSegment\_FluxCircumferential} \tag{2.16}$$

As can be seen, if the stator flux is in the circumferential direction, segmenting magnet circumferentially doesn't help to reduce the magnet losses.

Axially segmented

Figure 2.17 shows the eddy current paths and their resistances when stator flux is in the circumferential direction and the magnet is segmented axially.

The total resistance of the two magnet segments can be calculated

$$R'_{TwoAxialSegments\_FluxCircumferential} = \rho\left(\frac{4l_m}{A_r} + \frac{L_m}{A_z}\right) \tag{2.17}$$

Comparing (2.15) and (2.17), it can be seen that if the stator flux is in the circumferential direction, axial segmentation is effective to decrease magnet loss.

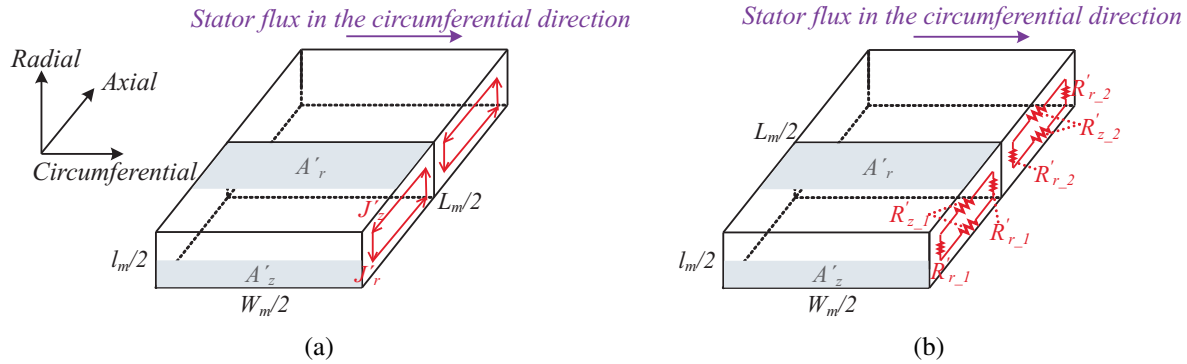

Fig. 2.17 Stator flux in the Circumferential direction for a magnet segmented axially into two; (a) The eddy current paths, (b) Resistances of the eddy current paths.

Radially segmented

The stator flux is kept in the circumferential direction. However, the magnet is segmented radially as shown in Fig. 2.18.

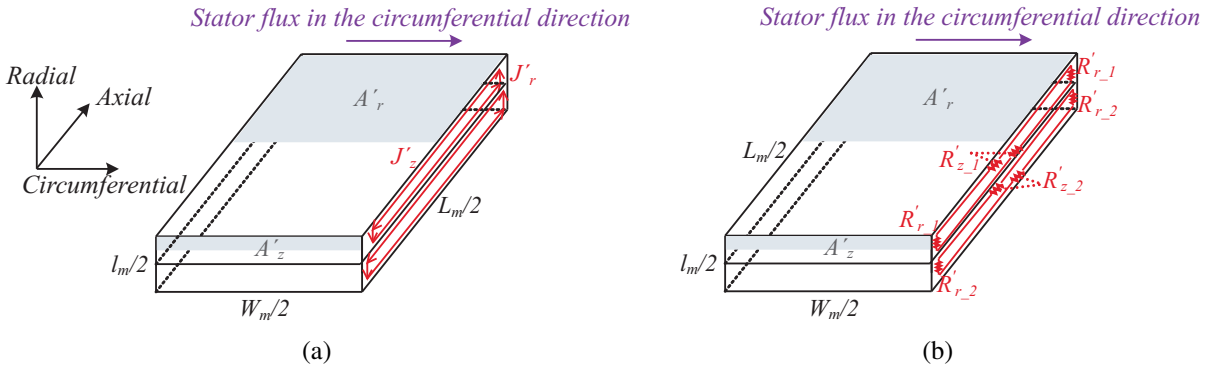

Fig. 2.18 Stator flux in the circumferential direction for a magnet segmented radially into two; (a) The eddy current paths, (b) Resistances of the eddy current paths.

The total resistance of the two magnet segments is

$$R'_{TwoRadialSegments\_FluxCircumferential} = \rho \left(\frac{l_m}{A_r} + \frac{4L_m}{A_z} \right) \tag{2.18}$$

Comparing (2.18) and (2.15), it can be seen that if the stator flux is in the circumferential direction, radial segmentation is also effective to decrease magnet loss. However, this type of segmentation can increase the effective air-gap thus decreasing the output performance.

2.4.3 Stator flux in the axial direction

If the stator flux is entering the magnet in the axial direction which is shown in Fig. 2.19, it creates eddy currents in the circumferential and radial direction (the red paths in Fig. 2.19(a)). These eddy current paths have resistances that are shown in Fig. 2.19(b).

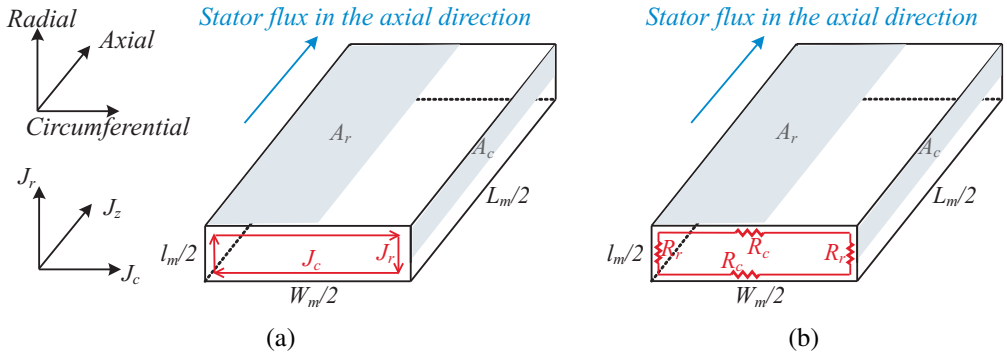

Fig. 2.19 Stator flux in the axial direction; (a) The magnet eddy current paths are in the radial and circumferential direction, (b) Resistances of the eddy current path.

The total resistance of the eddy current paths created by the stator flux in the axial direction is

$$R_{NoSegment\_FluxAxial} = \rho \left(\frac{l_m}{A_r} + \frac{W_m}{A_c} \right) \tag{2.19}$$

Circumferentially segmented

Stator flux is in the axial direction and magnet is segmented circumferentially. The eddy current paths are shown in Fig. 2.20(a).

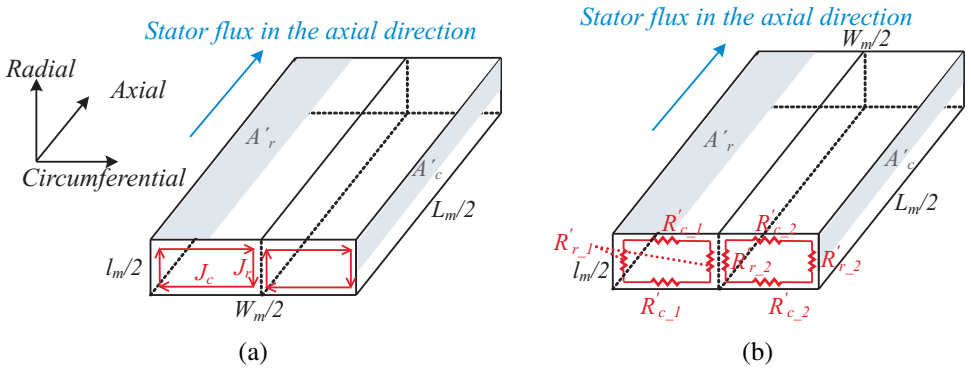

Fig. 2.20 Stator flux in the axial direction for a magnet segmented circumferentially into two; (a) The eddy current paths, (b) Resistances of the eddy current paths.

The total resistance of the two magnet segments is

$$R'_{TwoCirSegments\_FluxAxial} = \rho\left(\frac{4l_m}{A_r} + \frac{W_m}{A_c}\right) \tag{2.20}$$

Comparing (2.20) and (2.19), it can be seen that if the stator flux is in the axial direction, circumferential segmentation is effective to decrease the magnet losses.

Axially segmented

Stator flux is in the axial direction and magnet is segmented axially as well as shown in Fig. 2.21.

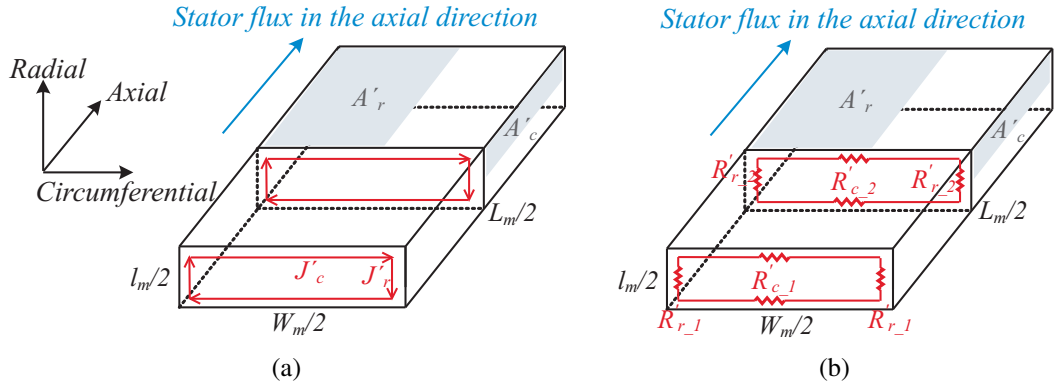

Fig. 2.21 Stator flux in the axial direction for a magnet segmented axially into two; (a) The eddy current paths, (b) Resistances of the eddy current paths.

The total resistance of the two magnet segments is

$$R'_{TwoAxialSegments\_FluxAxial} = \rho\left(\frac{l_m}{A_r} + \frac{W_m}{A_c}\right) = R_{NoSegment\_FluxAxial} \tag{2.21}$$

As can be seen from (2.21), if the stator flux is in the axial direction, segmenting magnet axially doesn't help to reduce the magnet losses.

Radially segmented

Stator flux is in the axial direction and magnet is segmented radially. The eddy current paths and their resistances are shown in Fig. 2.22.

The total resistance of the two magnet segments is

$$R'_{TwoRadialSegments\_FluxAxial} = \rho\left(\frac{l_m}{A_r} + \frac{4W_m}{A_c}\right) \tag{2.22}$$

Comparing (2.22) and (2.19), it can be seen that if the stator flux is in the axial direction, radial segmentation is effective to decrease the magnet losses. However, this method may add to the effective air-gap and thus decreasing the performance of the machine.

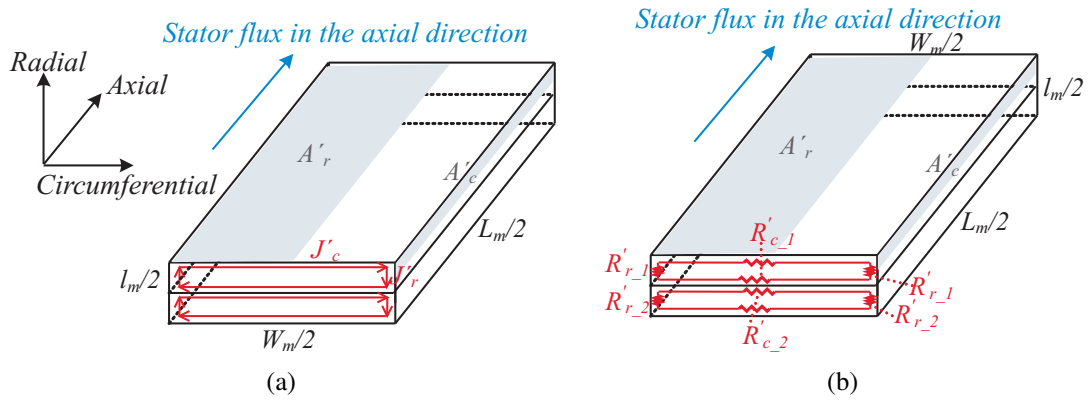

Fig. 2.22 Stator flux in the axial direction for a magnet segmented radially into two; (a) The eddy current paths, (b) Resistances of the eddy current paths.

2.4.4 Magnet loss calculation in FEM program Maxwell

In this work, the magnet losses of the machine for different speeds are calculated using FEM. To be able to calculate the magnet losses in Maxwell, the following steps are done:

- Setting a coil for the magnet with zero current.
- Magnet conductivity is considered to be 625 ksiemens/m.
- The permanent magnet loss in Maxwell 2D can be calculated as

$$PM\ loss = \int surface(magnet), totalloss \tag{2.23}$$

- Total magnet loss in Maxwell is

$$P_{magnet} = PM\ loss \times number\ of\ fractions \times machine\ length \tag{2.24}$$

When calculating the core and magnet loss, it has been considered that it is very important to have a high mesh density in the magnets and a high number of time-steps per period in the transient solutions [61].

2.4.5 Demagnetization

Permanent magnets are ferromagnetic material and ferromagnetic materials contain magnetic domains which can be organized by exposure to a magnetic field, so that the domains are aligned. When magnetizing this material, the applied field moves the domain walls through the material against different microstructural and crystallographic obstacles. After removing the external magnetic field, the domains are still aligned and the ferromagnetic material has an inherent magnetic field. The required magnitude of the magnetic field to align the domains

determines whether the material is classified as soft or hard (the value is lower for soft magnet material). All permanent magnet materials used for electric machines are hard [47] and [62].

A ferromagnetic material can be represented by two hysteresis loops, the normal and the intrinsic. The intrinsic loop represents the added magnetic flux density that the PM material produces. The normal curve represents the total magnetic flux density which is carried in combination by the air and by the PM. The difference between the intrinsic line and the normal line is thus the flux density $B_0 = \mu_0 H$, which is the flux density that we would have in the air at the field intensity *H* if we had no permanent magnet. Thus, $B_{normal} = B_0 + B_{\mathrm{intrinsic}}$. This is illustrated in Fig. 2.23 where the hatched line is the normal loop and the solid line is the intrinsic loop. As we are interested in the second quadrant (where $B > 0$ and $H < 0$, the normal lines are always below the intrinsic lines.

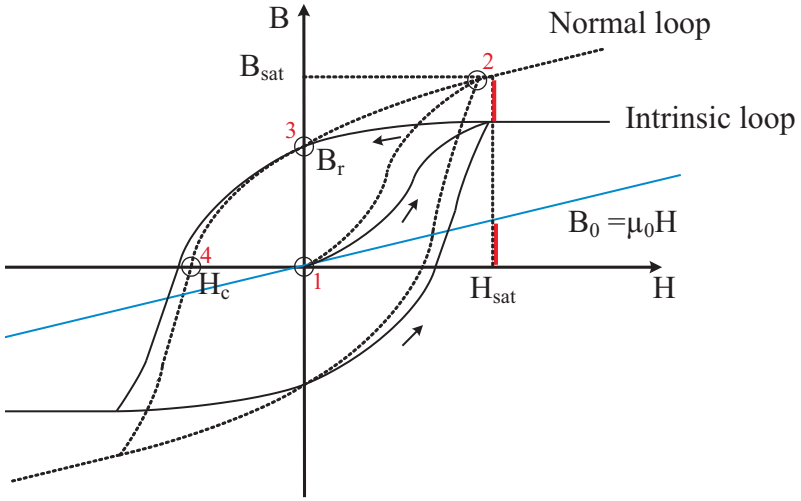

Fig. 2.23 Visualization of normal and intrinsic loops [47].

The full normal hysteresis loop of the ferromagnetic material, showing the magnetic flux density (*B*), versus the field intensity (*H*) is illustrated in Fig. 2.23. At point 1 where *B* and *H* are both zero the material is not magnetized (domains are not aligned). Applying an external magnetic field, H_{ext}, to the material, we move towards point 2 where domains become aligned. Here the maximum flux density is reached. The value of *B* in this point is called B_{max}. When comparing values of B_{max} for different materials, we should observe at what *H*-value the B_{max} value is given, so to make the comparison fair [47]. Since this affects the losses, the lower the *H*-value, the lower the hysteresis loss.

If the external field is removed , the flux density of the material goes down, and we end up in point 3 in Fig. 2.23. This value of the flux density (when *H=0*) is called the remanence, B_r. Thus now the material is magnetized. If an external magnetic field, in the opposite direction towards the magnetized direction is applied, it forces the materials flux density to zero (point 4 in Fig. 2.23). The *H*-value in point 4 is called the coercivity, H_c. The line between point 3 and point 4 in Fig. 2.23 is important, since here the operation of the magnet typically occurs.

Permanent magnets are designed to operate between point 3 and 4 in Fig. 2.23. The line between point 3 and 4 is liner until the magnetic field density reaches B_{knee}. When the flux density

becomes lower than B_{knee}, the PM is irreversibly demagnetized. The minimum flux density in the PMs has to be verified during the magnetic analysis of the machine [63]. B_{knee} depends on the temperature and increases with the temperature, see Fig. 2.24. The higher the temperature, the higher B_{knee} and therefore, the easier demagnetization is.

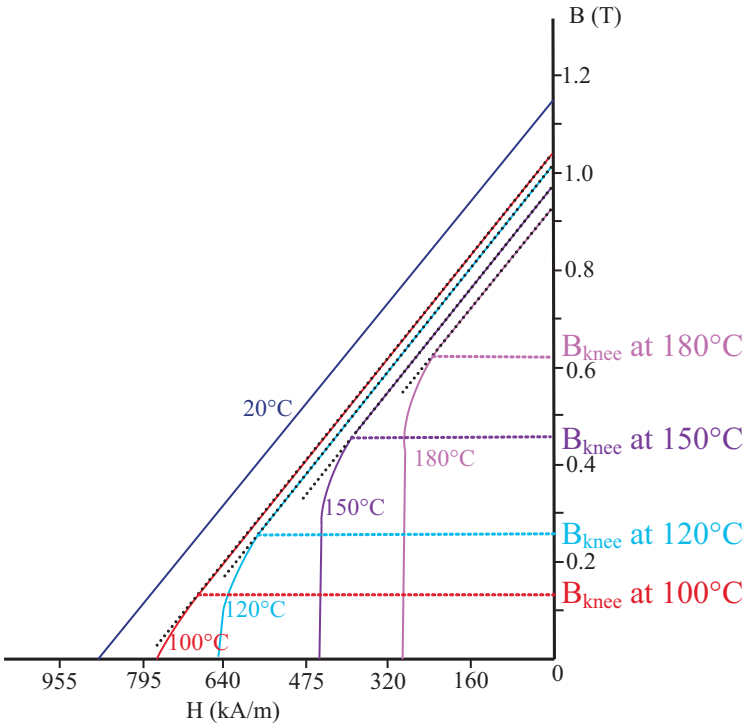

Fig. 2.24 B-H curve of a PM including the variation of temperature [63].

2.5 Mechanical stress on rotor barriers

In [64], it is discussed that the main force components present during motor operation are the centrifugal force from angular velocity, the radial attractive force between the permanent magnet and the stator, and the tangential force that produces the torque of the machine. Tangential stress establishes the relationship between the total electromagnetic torques developed by the machine per unit of rotor volume and is strongly related to the cooling method. Different types of electrical machines have different acceptable stress ranges for proper operation. In addition, acceleration and deceleration creates stresses due to the circumferential inertia loads. Finally, differential thermal expansion can result in internal structural stresses. Three types of forces for two IPM motors (radial IPM and V-shape IPM) are investigated in [65]. It is shown that the centrifugal forces are the most dominant forces in creating stress.

In order to compare the maximum stresses or to predict yielding of materials of different designs at different operating conditions, the values of the von Mises stress or equivalent tensile stress, σ_ν, is often used. The von Mises stress is a scalar value, resulting from consideration of the stress components (both normal and shear stresses) in three dimensions according to [66]

$$\sigma_\nu = \sqrt{\frac{1}{2}\left[(\sigma_{xx} - \sigma_{yy})^2 + (\sigma_{yy} - \sigma_{zz})^2 + (\sigma_{zz} - \sigma_{xx})^2 + 6\left(\sigma_{xy}^2 + \sigma_{yz}^2 + \sigma_{zx}^2\right)\right]} \tag{2.25}$$

where the normal stress is denoted as σ_{ii}, and shear stress is denoted as sigma σ_{ij}.

The von Mises stress can be calculated from the FEM program package Ansys, using Maxwell to build the model and calculate load forces and Ansys Mechanical to calculate stress due to centrifugal forces and load forces.

Chapter 3

Wind generator system design

3.1 Wind turbine rotor speed and power versus wind speed

The value of the rotor speed in relation to the power is determined from an existing 2 MW wind turbine investigated in [67]. Figures 3.1 and 3.2 show power and rotor speed versus wind speed for the 2 MW wind turbine in [67], respectively.

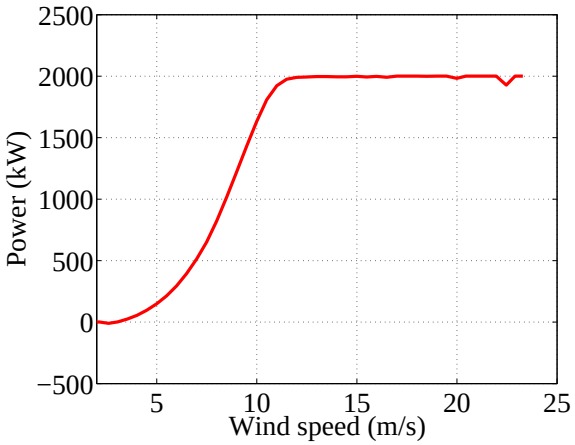

Fig. 3.1 Electric power versus wind speed for the 2 MW turbine [67].

In this work, the attempt is to design 5 MW generators. Therefore, the power of the 2 MW wind turbine is scaled up to get a 5 MW wind turbine, with the same rated wind speed which is 12 m/s. The power of the generator versus wind speed and the rotor speed as a function of wind speed related to the 5 MW wind turbine are shown in Fig. 3.3 and Fig. 3.4.

It should be mentioned that the rotor speed of a 5 MW wind turbine turns slower than a 2 MW wind turbine, since the rotor diameter is bigger. However, since in this work, direct-drive generators are not studied and it is assumed that a gearbox is included in the system, the turbine rotor speed versus wind speed of this 5 MW wind turbine is assumed to be the same as the turbine rotor speed of the 2 MW wind turbine.

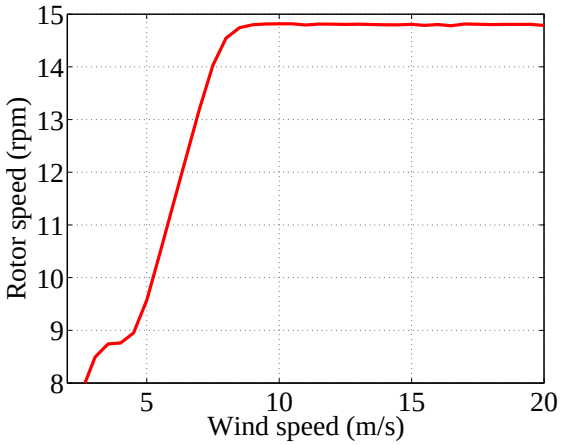

Fig. 3.2 Rotor speed versus wind speed for the 2 MW turbine [67].

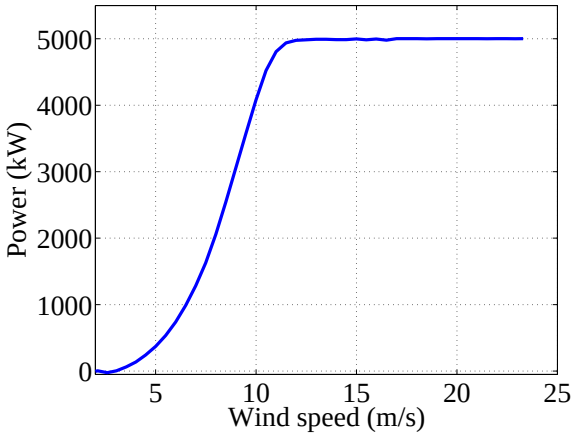

Fig. 3.3 Power versus wind speed for the investigated wind turbine system.

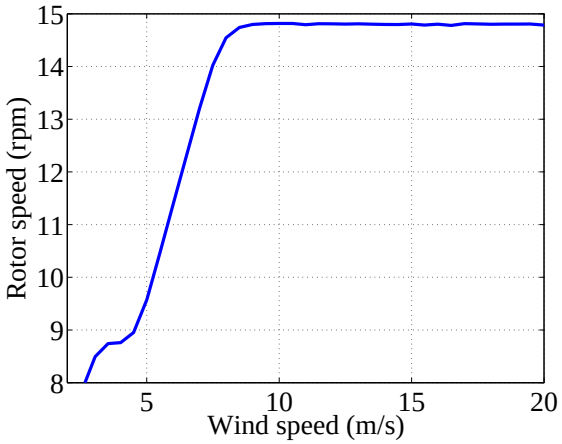

Fig. 3.4 Rotor speed versus wind speed for the investigated wind turbine system.

3.2 Generator speed

As can be seen in Fig. 3.4, the turbine speed at rated wind speed is 14.8 rpm. The gearbox ratio is assumed to be 50.67 and accordingly the generator speed at rated wind speed becomes 750 rpm.

As was mentioned, the rotor speed of a 5 MW wind turbine turns slower than a 2 MW wind turbine. However, as the gearbox losses are not considered in this thesis, we can still use the generator speed of 750 rpm for a 5 MW wind turbine with any rotor speed versus wind speed and just change the gearbox ratio.

3.3 Generator number of poles and frequency

According to [68], by increasing the number of poles, the thickness of the stator yoke can be reduced and therefore the usage of stator core material for the yoke can also be reduced. More power output or torque can be achieved by using more poles for the same frame due to the reduction of yoke thickness. Since the operating frequency increases proportionally to the number of poles in order to achieve the desired speed, both eddy current loss and hysteresis loss increase despite the fact that the mass of the stator core material is reduced. Increasing the number of poles also makes the end windings shorter which leads to less copper losses. However, a SynRM is considered to be best with a pole number of 4 or 6 (see e.g. [14]). As a compromise and as a starting point in the assessment of different designs and machine types in this work, eight poles are selected for all the machine types. For future work, it can be interesting to investigate higher pole numbers, since the recommendation of 4 or 6 poles for SynRMs could be questioned for larger machines such as generators for wind applications.

After defining the number of poles and speed of the machine, the frequency of the machine can be calculated according to

$$f = \frac{n_{rotor} p}{60} \tag{3.1}$$

where n_{rotor} is the rotor speed in rpm and p is the number of pole pairs.

As was explained in Section 3.2, the generator speed is considered to be 750 rpm. Therefore the frequency of the machines is 50 Hz.

3.4 Core material

The stator material properties affects the iron losses of the machine. Here, the material that is used for the generator stator and rotor is selected to be M235−35A (0.35 mm thickness) which is a non-linear material, represented in the library of the used FEM program (Ansys Maxwell). This material is a laminated steel with the stacking factor of 0.95. The thinner the steel laminations are, the lower the iron losses will be while the stacking factor will go down.

However, the cost for a thin lamination will be higher compared to, for example, lamination with a thickness of 0.5 mm. The B-H curve of this material, material data and material loss curves versus different frequencies can be found in [27].

3.5 Permanent magnet material

The permanent magnet material used for the SPMSG, IPMSG and PMa-SynRG investigated in this work is Neodymium Iron Boron (NdFeB). The data of the used permanent magnet material at $100\,^{\circ}\mathrm{C}$ is shown in Table 3.1.

TABLE 3.1: Permanent magnet material data

Parameter	Value
Mass density	7550 kg/m^3
Conductivity	625 kS/m
Relative permeability	1.044
Coercivity	838 kA/m

According to the data in Table 3.1, the remanence of the magnet material can then be calculated as

$$B_r = \mu_0 \mu_r H_c \tag{3.2}$$

where μ_0 is the permeability of air which is $4\pi\times\ 10^{-7}$, μ_r is the relative permeability of the material and H_c is the coercivity. Therefore, the remanence of the selected magnet material is 1.1 T. However, the remanence of some Neodymium magnets can be higher.

The B-H curve of the selected permanent magnet material at different temperatures is shown in Fig. 3.5.

3.6 Geometry

The stator that is used here is the same as the stator of the IPMSG used in [27]. The dimensions of the stator is given in Table 3.2.

TABLE 3.2: Stator size

Parameter	Value
Outer stator diameter	1100 mm
Inner stator diameter	758 mm
Stator length	945 mm

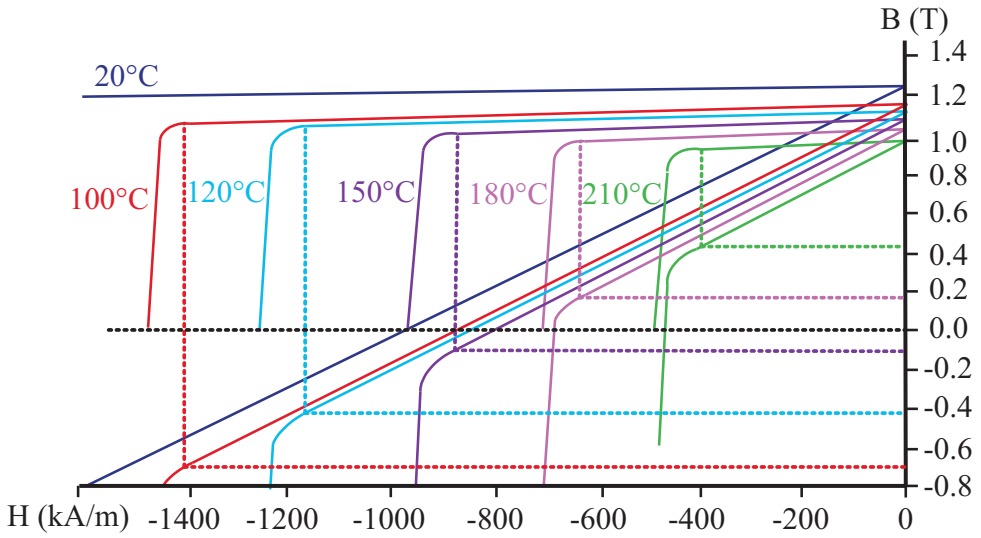

Fig. 3.5 The normal and intrinsic B-H curves of the used magnet for different temperatures.

3.6.1 Air-gap length

The air-gap length influences the characteristics of an electrical machine significantly. In permanent magnet synchronous machines, the air-gap length is determined by mechanical constrains. In [69] it is shown that this value is similar to those values encountered in induction machines and if the number of pole pairs is greater than 1 (p>1), the air-gap length in mm can approximately be calculated as:

$$g = 0.18 + 0.006P^{0.4} \tag{3.3}$$

where P is the power of the machine in Watts. According to (3.3), the air-gap length for this machine can be selected to be 3 mm.

3.6.2 Number of slots

The number of slots are considered to be 72 and since the number of poles are 8, an integer slot winding is used. The stator slot size values are shown in Table 3.3. This type of slot can be used for circular cross-section wires as well as rectangular wires.

In [27], the same size of the stator with 90 slots yielding a fractional slot winding is also investigated. A SPMSG with the fractional slot winding stator is presented in Section 3.6.4 as well.

TABLE 3.3: Stator slot size of the integer winding of the 72 slot machine

Parameter		Value
Hs0	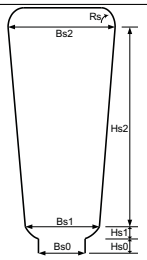	6 mm
Hs1		2 mm
Hs2		90 mm
Bs0		10.4 mm
Bs1		16 mm
Bs2		24 mm
Rs		12 mm

3.6.3 Winding arrangements

A double-layer winding is chosen for this machine, since double-layer windings can be designed with a coil pitch giving a smoother mmf waveform, while single-layer windings have limited possibilities in that regard [70] and armatures of nearly all synchronous machines are wound with double-layer windings [71]. The coils are selected to be short-pitched because the end winding of the short-pitch winding are shorter than the ones of the full-pitch winding which leads to lower cost of copper, lower resistance (higher efficiency) as well as it reduces certain harmonics in the air-gap field and the back-emf. The connection of phase A is illustrated in Fig. 3.6. Table 3.4 shows the winding data of the machine.

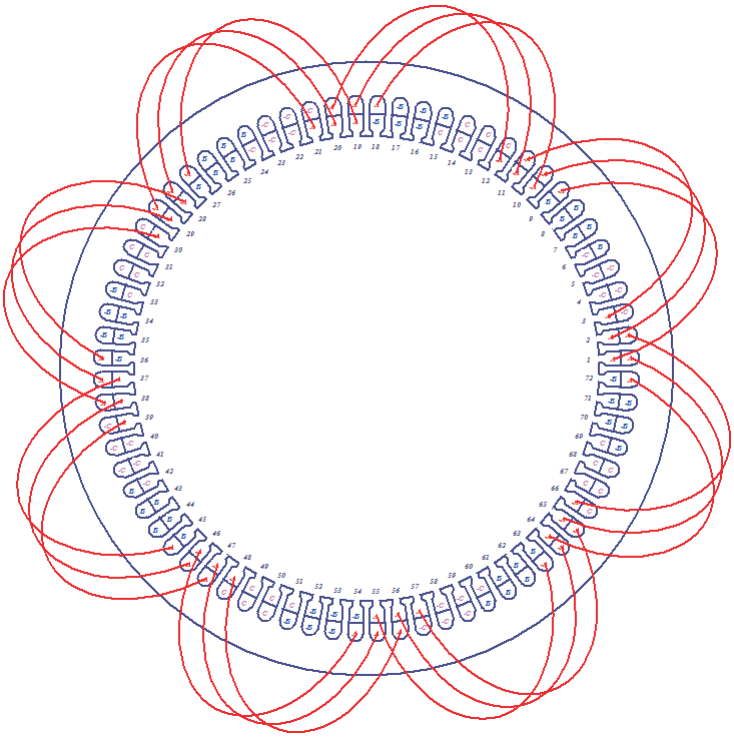

Figure 3.6: Phase A winding connection.

TABLE 3.4: Winding data for the integer slot winding stator

Symbol	Parameter	Value
$2N_c$	Number of conductors per slot	14
N_c	Number of conductors per slot per phase	7
y	Coil pitch	8
a	Number of parallel branches	2
SF_g	Slot fill factor	50%

According to [27], the copper area (A_{copper}) is

$$A_{copper} = 72.434 \times 10^{-6} m^2 \tag{3.4}$$

The wires are assumed to consist of strands. So the skin effect is strongly reduced. In [27], the skin depth is calculated and the conclusion drawn was that skin effect can be neglected.

3.6.4 Magnet coverage

The choice of the magnet width and coverage, apart from affecting the average torque of the machine, has also a direct effect on iron losses, since it affects the tooth and yoke eddy current losses of the machine. Therefore, it is important to choose a good ratio of the magnet width to the pole pitch. Figure 3.7 shows the pole pitch (τ_p) and magnet width (W_m) of a surface permanent magnet synchronous machine (SPMSM). In [72], it is shown that if this ratio ($\frac{W_m}{\tau_p}$) is high (close to 1.0), the tooth eddy current increases and if it is very low (magnet width less than one slot pitch, τ_s , shown in Fig. 3.8), no tooth has constant flux density. The range for this ratio in [73] is recommended to be around 0.8. In [74], [75], [76] and [77], the effects of magnet width on cogging torque and torque ripple are discussed.

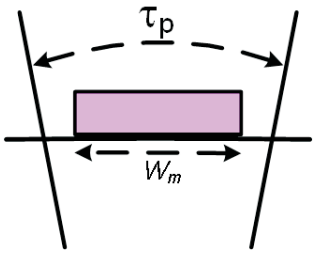

Fig. 3.7 Pole pitch and magnet width in a SPMSM [73].

The ratio of $\frac{W_m}{\tau_p}$ can also be expressed as magnet coverage. If the polar arc (θ) which is the angle that the magnet covers on the surface of the rotor (see Fig. 3.8) is given in mechanical degrees, the magnet coverage (α) is

$$\alpha = \frac{p\theta}{180} \tag{3.5}$$

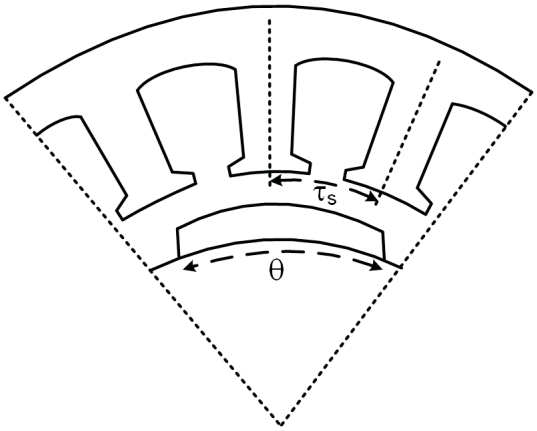

Fig. 3.8 Polar arc (θ) and slot pitch (τ_s) of a SPMSM.

In SPMSMs the magnets can be shaped. The curved magnets with the largest thickness in the center and the thinnest thickness at the two ends can improve the curvature of the flux waveforms and in this way, the eddy current losses can be reduced [78]. Fig. 3.9 shows the shape of one magnet with and without curving. If the magnet was to be completely curved (with no cut edges) then the magnet coverage may be as high as almost 100% of the pole pitch, whereas magnets with cut edges have a lower maximum limit.

Fig. 3.9 Magnet shape. Black without curving and red curved magnet.

As the relative permeability of the magnet material is close to one, SPMSM has a large effective air-gap which influences the magnetizing inductance. Using a thicker magnet results in a higher effective air-gap which consequently results in a decrease of the magnetizing inductance of the machine. This also affects the air-gap flux density and the torque of the machine.

In [77], it is suggested that for a permanent magnet motor, the optimum magnet coverage is

$$\frac{1}{mq} \leq \alpha \leq \frac{mq-1}{mq} \tag{3.6}$$

where *m* is the number of phases and *q* is the number of slots per pole per phase.

According to [74], the fundamental sinusoidal component of the cogging torque can be eliminated by an appropriate choice of the magnet width. The optimum magnet coverage to achieve the least cogging torque is [68]

$$\alpha = \frac{n+0.14}{mq} \tag{3.7}$$

where *n* is any integer number which satisfies $\alpha < 1$.

In this work, to find the best selection of magnet coverage to get the highest torque and lowest loss, torque ripple and cogging torque from the machine, two SPMSMs from [27] are consid-

ered. However, in contrast to the machine in [27], here the magnets of the machine are not curved in order to focus the investigation on the magnet coverage. Both machines have the same rotor. One has an integer slot winding and the other one has a fractional slot winding. The integer slot winding stator is the same stator that is designed in Section 3.6.2. The winding arrangement is discussed in Section 3.6.3. The objective is to use the same magnet weight, thus by decreasing the magnet coverage, the thickness of the magnet increases to keep the magnet weight constant. The air-gap is kept constant in all cases and the rotor outer diameter changes when α is varied.

Analysis on an integer slot machine with different magnet coverage

The data of the integer winding SPMSG which is used in this section to investigate the effect of magnet coverage on average torque, torque ripple, losses and magnetizing inductance is given in Table 3.5. The cross-section of this machine for a magnet coverage of 0.7 is shown in Fig. 3.10. As can be seen from the data, the number of slots per pole per phase, *q=3*.

TABLE 3.5: SPMSG with integer slot winding data

Parameter	Value
Rated output power	5 MW
Number of poles	8
Number of slots	72
Number of phases	3
Frequency	50 Hz
Rated speed	750 rpm
Outer stator diameter	1100 mm
Inner stator diameter	758 mm
Stator length	945 mm
Air-gap length	5 mm
Pole pitch	293.7 mm
Tooth width	22.7 mm
RMS stator line current	635 A
Current density	4.4 A/mm^2
Electric loading	135 kA/m
Magnet weight	329 kg

Combining (3.6) and (3.7), the optimum magnet coverage for this SPMSG (where *m=3* and *q=3*) would be 0.13, 0.23, 0.35, 0.46, 0.57, 0.68 and 0.79. The choice of α is then also considering that the yoke eddy current loss is inversely proportional to the magnet coverage, as suggested in [68]. Therefore, the optimum magnet coverage for this machine seems to be 0.79.

Magnet coverage of this SPMSG is varied from 0.52 to 0.93 with 0.1 in each step. By increasing the magnet coverage, the magnet thickness is reduced so that the magnet weight is the same. The full load current (635 A) at the rated speed is applied. The tooth and yoke losses are taken from the FEM program Maxwell and magnet losses are calculated using (2.23) and (2.24) in

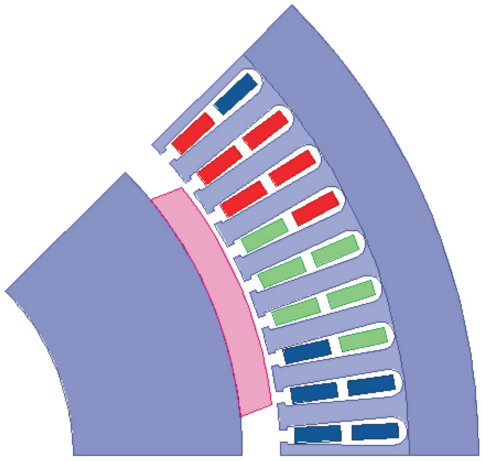

Fig. 3.10 Cross-section of the integer slot winding machine for a magnet coverage of 0.7.

Maxwell. Figure 3.11 shows the average torque versus magnet coverage for this machine. In Fig. 3.11 it is clearly seen that average torque has a maximum value when α is between 0.7 and 0.8, and for this machine maximum average torque occurs at $\alpha = 0.76$.

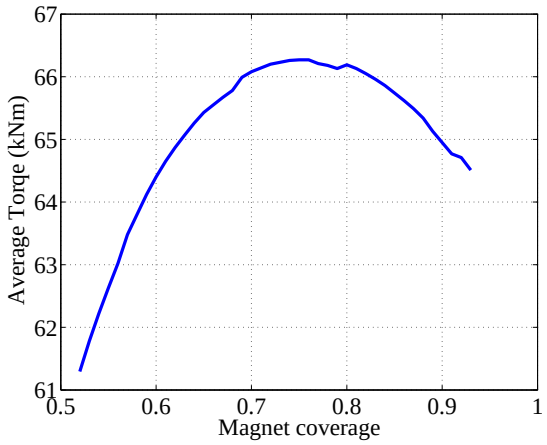

Fig. 3.11 Average torque as a function of magnet coverage for the integer winding machine.

The torque ripple (peak to peak) for different magnet coverages is shown in Fig. 3.12. It should be noted that the torque ripple is rather high for this machine without shaping of the magnets (between 4% and 11%). In fact, the same machine but with curved magnets gives only a torque ripple of 2.4% when the magnet coverage is 0.7 [27], compared to 6.1% without curved magnets at the same magnet coverage of 0.7.

From Fig. 3.12, it can be seen that the maximum torque ripple occurs when α=0.6 and α=0.86. This should be when both magnet edges coincide with slot edges. In that case, there should be extra torque ripple when

$$\alpha = nW_s + W_t \qquad n = 0, 1, 2, ... \tag{3.8}$$

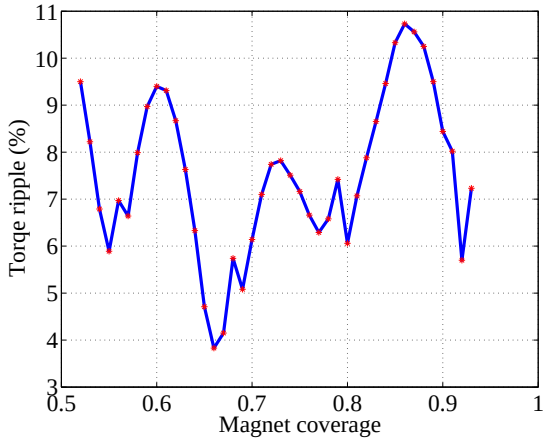

Fig. 3.12 Torque ripple as a function of magnet coverage for the integer winding machine.

where W_s and W_t is the slot pitch and tooth width normalized to the pole pitch. As can be seen from Table 3.5, this machine has 72 slots and 8 poles, hence 9 slots per pole. Therefore, $W_s = \frac{1}{9} pole\ pitch$. The tooth width and pole pitch values are also given in Table 3.5. From that $W_t = 0.077 pole\ pitch$. According to (3.8), the magnet coverage of 0.19, 0.3, 0.41, 0.52, 0.63, 0.74, 0.85, and 0.96 yield higher values for torque ripple. As can be noted in Fig. 3.12 the match is very good, although not always exactly accurate.

The iron loss as a function of magnet coverage is shown in Fig. 3.13 where the stator loss is separated as tooth loss and yoke loss. From the figure, it is seen that the yoke eddy current loss is inversely proportional to the magnet coverage (as stated in [68]) only if $\alpha > 0.72$. It can also be seen from Fig. 3.13 that the tooth loss increase for increasing α, as stated in [72], and that the total stator loss increase up to a magnet coverage of 0.8 where it levels out at a constant value.

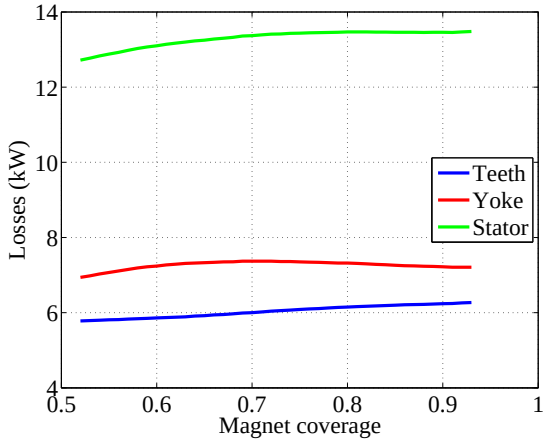

Fig. 3.13 Iron loss as a function of magnet coverage for the integer winding machine.

In Fig. 3.14 it is seen that the permanent magnet loss increases with increasing magnet coverage.

The influence of the change in effective air-gap on the magnetizing inductance is illustrated in Fig. 3.15, showing L_m as a function of α. As expected, L_m, increases with increasing α.

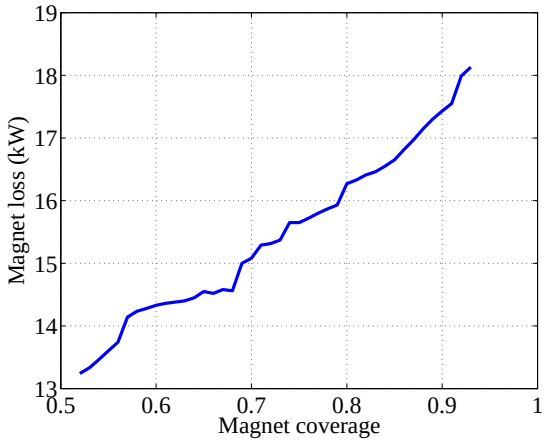

Fig. 3.14 Permanent magnet loss as a function of magnet coverage for the integer winding machine.

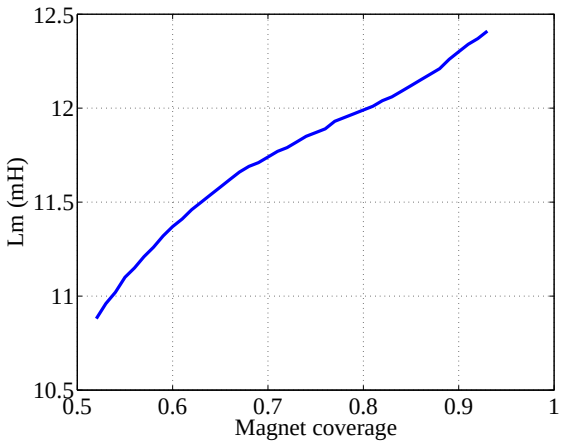

Fig. 3.15 Magnetizing inductance, L_m, as a function of magnet coverage for the integer winding machine.

The cogging torque (the maximum torque at no load), see Fig. 3.16, of the integer slot winding machine is also calculated from Maxwell to investigate (3.7). It was seen that a lower cogging torque occurs when

$$\alpha = \frac{n}{mq} \tag{3.9}$$

meaning that if the magnet coverage is an integer value of a slot pitch angle, a lower cogging torque will be obtained. For this machine, (3.9) yields the magnet coverage of 0.11, 0.22, 0.33, 0.44, 0.56, 0.67, 0.78, 0.89. This also agrees with (3.7).

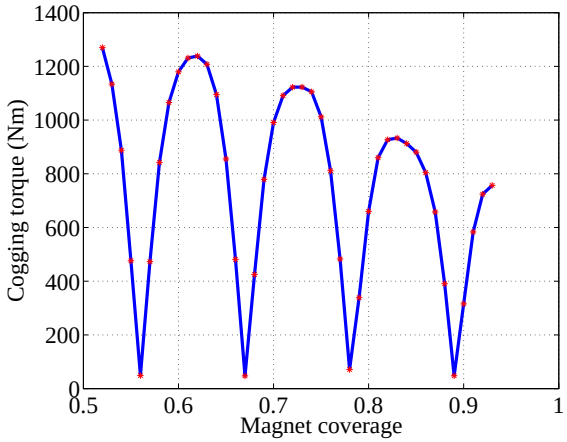

Fig. 3.16 Cogging torque as a function of magnet coverage.

Analysis on a fractional slot machine with different magnet coverage

The same investigations as in the previous section is done for a fractional slot winding SPMSM. The rotor of the machine is the same as the rotor of the integer slot winding machine. The dimension of the stator is also the same as the dimension of the integer slot winding SPMSM investigated before. However, the stator has 90 slots. Therefore, the number of slots per pole per phase, *q=3.75*. The current density of this machine is the same as the current density of the integer slot machine ($4.4\ A/mm^2$). Figure 3.17 shows the cross-section of the machine for $\alpha = 0.8$.

As the number of slots in this SPMSG has increased to 90 compared to 72 in the integer winding SPMSG, the stator slot size will be smaller. The stator slot size values are shown in Table 3.6.

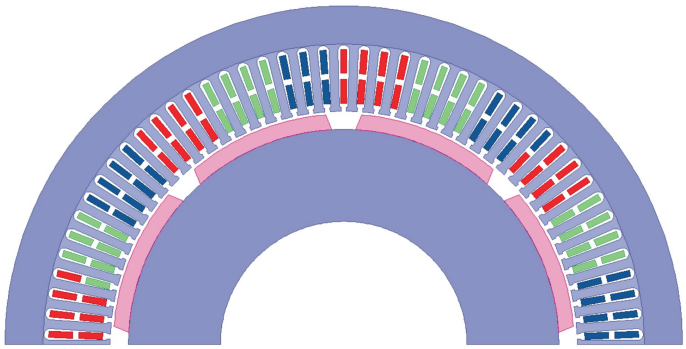

Fig. 3.17 Cross-section of the fractional slot winding machine for a magnet coverage of 0.8.

TABLE 3.6: Stator slot size for the fractional slot SPMSG

Parameter		Value
Hs0	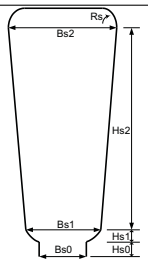	6 mm
Hs1		2 mm
Hs2		90 mm
Bs0		8.32 mm
Bs1		12.8 mm
Bs2		19.2 mm
Rs		12 mm

To keep the current density value for this machine the same as the current density in the integer slot winding SPMSG, the number of conductors in the slot needs to be changed. The winding data is given in Table 3.7.

TABLE 3.7: Winding data for the fractional slot stator

Symbol	Parameter	Value
$2N_c$	Number of conductors per slot	12
N_c	Number of conductors per slot per phase	6
y	Coil pitch	11
a	Number of parallel branches	2
SF_g	Slot fill factor	50%

The phase A winding connection for this fractional slot SPMSM is shown in Fig. 3.18. More information about the stator of this machine can be found in [27].

Combining (3.6) and (3.7) and considering that according to [68] the yoke eddy current loss is inversely proportional to the magnet coverage, the optimum magnet coverage should be 0.9. However the following results show that this is not the optimum magnet coverage.

Magnet coverage of this fractional slot winding SPMSG is also varied from 0.52 to 0.93 with 0.1 in each step. In the same way as before, by increasing the magnet coverage, the magnet

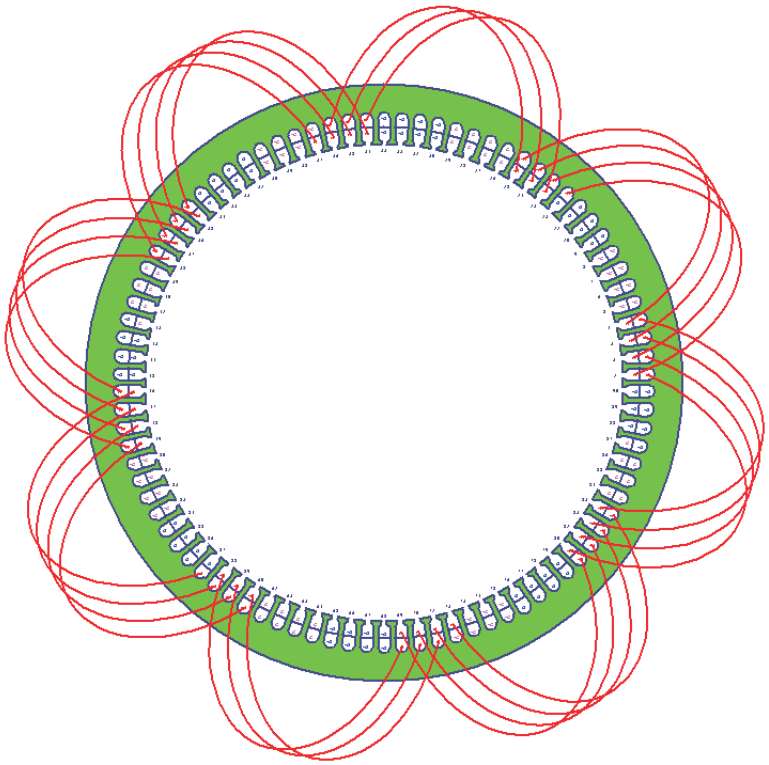

Figure 3.18: Phase A coil side distribution for the fractional slot winding for an 8-pole, 90-slot machine.

thickness is reduced so that the magnet weight is the same. The full load current (508.6 A) at the rated speed which gives the same current density ($4.4\ A/mm^2$) as the integer slot SPMSG is applied. Figure 3.19 shows the average torque versus magnet coverage for this machine. In Fig. 3.19 it is clearly seen that also for this machine, the average torque has a maximum when α is between 0.7 and 0.8, and incidentally also for this machine, maximum average torque occurs at $\alpha = 0.76$.

The torque ripple for different magnet coverages for this machine is shown in Fig. 3.20. It should be noted that the torque ripple can be reduced with this fractional slot machine compared to the integer slot machine; the lowest value occurs at $\alpha = 0.69$ with 3.2%. Equation (3.8) is not valid for this machine, as the number of slots per pole pitch varies and is not an integer .

The iron loss as a function of magnet coverage behaves very similar for the fractional slot machine as for the integer slot machine, see Fig. 3.21 where the stator loss is separated as tooth loss and yoke loss. It can be seen from Fig. 3.21 that the tooth loss increases with increasing α, as stated in [72], and that the total stator loss increase up to a magnet coverage of 0.8 where it levels out at a constant value.

Permanent magnet loss and magnetizing inductance as a function of magnet coverage are shown in Fig. 3.22 and Fig. 3.23, respectively. It can be seen from the figures that magnet losses and magnetizing inductance increases in this machine as well. The magnetizing inductance increases as the effective air-gap decreases.

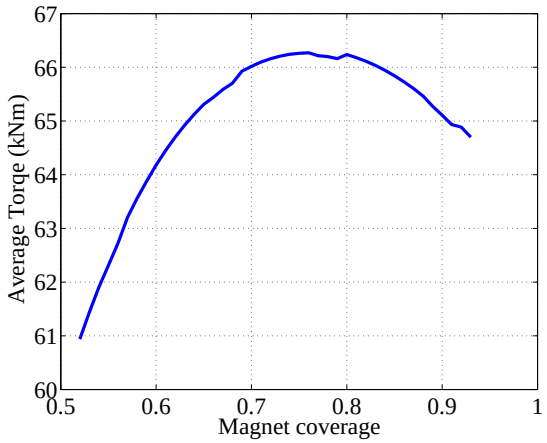

Fig. 3.19 Average torque as a function of magnet coverage for the fractional slot machine.

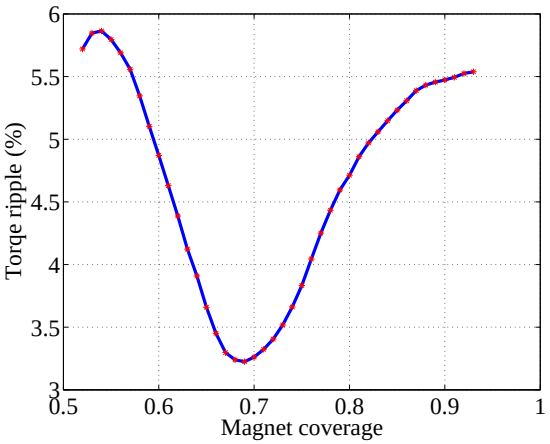

Fig. 3.20 Torque ripple as a function of magnet coverage for the fractional slot machine.

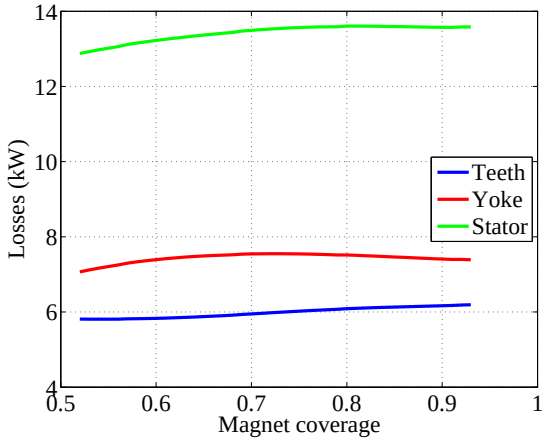

Fig. 3.21 Iron loss as a function of magnet coverage for the fractional slot machine.

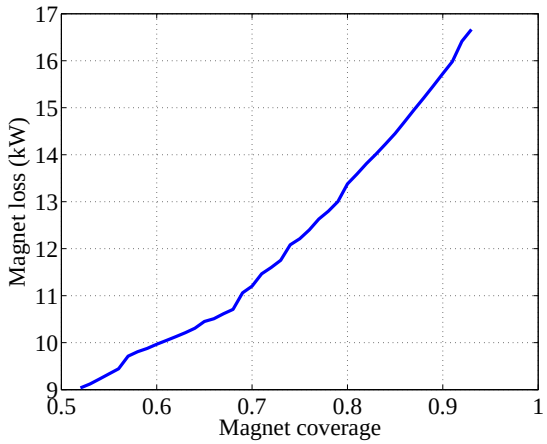

Fig. 3.22 Permanent magnet loss as a function of magnet coverage for the fractional slot machine.

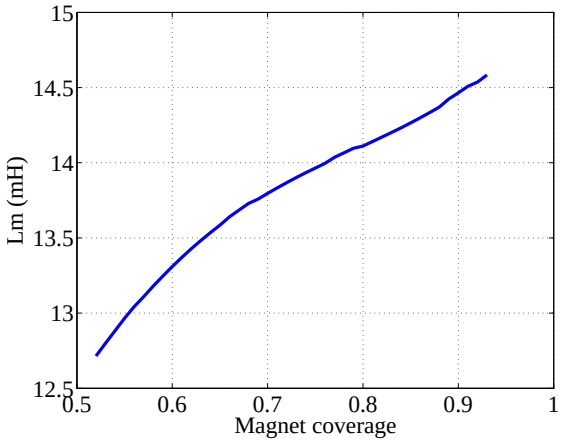

Fig. 3.23 Magnetizing inductance, L_m, as a function of magnet coverage for the fractional slot machine.

The cogging torque of the fractional slot SPMSG is not investigated, since the cogging torque for the fractional slot machine is very low. A comparison of the cogging torque of an integer slot winding IPMSG and a fractional slot winding IPMSG is given in [27].

The conclusion is that the optimal magnet coverage can only be found by extensive investigations for each specific machine. However, an estimate value of a suitable magnet coverage value can be found from recommendations and formulas, including only the number of phases and the number of slots per pole per phase. This estimate value of magnet coverage could either be used directly, yielding acceptable values of torque, torque ripple and losses, or it could be used as a starting value for an optimization procedure. Here, from the figures it can be seen that such an optimization could give 0.2-1.8% higher torque and 17-40% lower torque ripple (at full load), and up to 0.6-0.8% lower core loss, and up to 28% lower magnet loss, compared to using the estimate value for a machine with straight edges and equal weight.

Chapter 4

Rotor design of an interior permanent magnet synchronous generator

4.1 Electromagnetic design

The rotor of the IPMSG that is used here is from [27]. The initial dimensions for designing the machine is explained in [27]. The stator dimensions and air-gap length selection are given in Section 3.6 and Section 3.6.1, respectively. The cross-section of the machine is shown in Fig. 4.1.

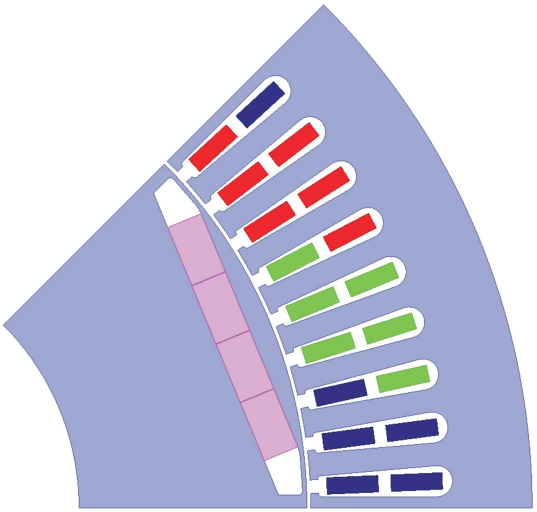

Fig. 4.1 Cross-section of the IPMSG.

4.1.1 Dimensions

The data of the machine is given in Table 4.1.

TABLE 4.1: IPMSG data

Parameter	Value
Rated output power	5 MW
Outer rotor diameter	752 mm
Inner rotor diameter	400 mm
Rotor length	945 mm
Air-gap length	3 mm
RMS stator line current	555 A
Armature phase resistance	39.5 mΩ
Current density	3.8 A/m^2
Electric loading	118 kA/m

With this value of electric loading a direct water cooling is needed for this machine according to [69].

The magnet parameters are shown in Fig. 4.2 and given in Table 4.2.

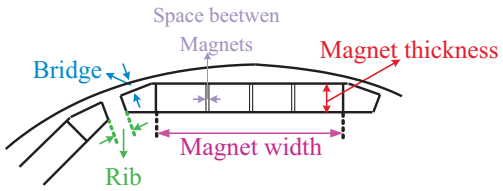

Fig. 4.2 IPMSG magnet parameters.

TABLE 4.2: IPMSG data

Parameter	Value
Magnet thickness	28 mm
Magnet width	195 mm
One magnet segment width	48.45 mm
Bridge	3 mm
Rib	20 mm
Space between magnets	0.4 mm

4.1.2 Magnet loss and segmentation

As was explained in Section 2.4, for a radial machine, segmenting the magnet in the circumferential or axial direction can be useful to reduce the magnet losses depending on the direction of the stator flux. To find out in which direction the segmentation should be done for this IPMSG, theoretical formulas and FEM results are investigated and compared.

Comparison between a theoretical approach and simulation results

If the magnet is segmented into 2 pieces, according to (2.11), (2.12) and (2.13), if the stator flux is in the radial direction, the circumferential segmentation is most useful for this machine.

$$R'_{TwoCirSegments\_FluxRadial} = 3.7 R_{NoSegment\_FluxRadial} \tag{4.1}$$

$$R'_{TwoAxialSegments\_FluxRadial} = 1.2 R_{NoSegment\_FluxRadial} \tag{4.2}$$

If the stator flux is in the circumferential direction, according to (2.15), (2.16) and (2.17):

$$R'_{TwoCirSegments\_FluxCircumferential} = R_{NoSegment\_FluxCircumferential} \tag{4.3}$$

$$R'_{TwoAxialSegments\_FluxCircumferential} = 1.002 R_{NoSegment\_FluxCircumferential} \tag{4.4}$$

As can be seen, neither circumferential segmentation nor axial segmentation will reduce the magnet losses if the stator flux is in the circumferential direction for this machine.

If the stator flux is in the axial direction, according to (2.19), (2.20) and (2.21):

$$R'_{TwoCirSegments\_FluxAxial} = 1.06 R_{NoSegment\_FluxAxial} \tag{4.5}$$

$$R'_{TwoAxialSegments\_FluxAxial} = R_{NoSegment\_FluxAxial} \tag{4.6}$$

To compare the theoretical values with simulation, a 2D as well as a 3D model of the IPMSG are used. As was mentioned in Section 2.4.4, to calculate the magnet loss accurately it is very important to have a high mesh density in the magnets and a high number of time-steps per period in the transient solutions [61].

First a 2D model of the IPMSG with magnets divided into 4 pieces circumferentially is considered. The width of each magnet and the space between the magnets are given in Table 4.2. The total loss (W/m^3) in the magnets is plotted in Fig. 4.3. Flux-lines are also plotted in the magnets. As can be seen, the loss is concentrated to the top surface of the magnets.

A 3D model of the IPMSG with magnets divided into 4 pieces in the circumferential direction is also considered. To save time, half of the machine length (472.5 mm) is modelled. Figure 4.4 shows the model of the IPMSG in 3D.

The total loss in the magnets in 3D is plotted in Fig. 4.5. As can be seen, the loss is just like for the 2D model concentrated to the top surface of the magnets.

The magnet loss and torque value of the IPMSG with magnet segmented into 4 pieces circumferentially in 2D and 3D are given in Table 4.3. As can be seen the 2D and 3D results agree fairly well.

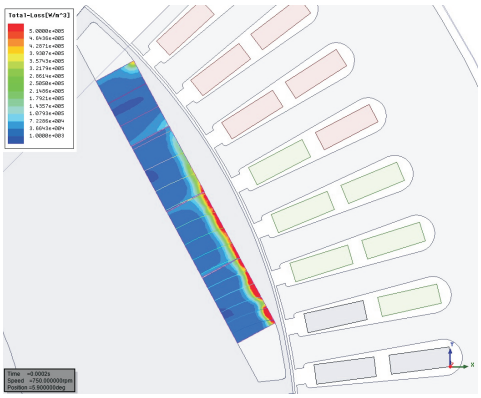

Fig. 4.3 The loss density in the IPMSG magnets with 4 circumferential segments.

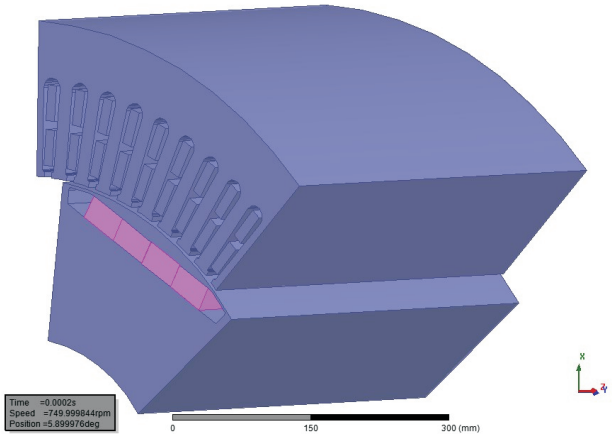

Fig. 4.4 The half-length IPMSG model.

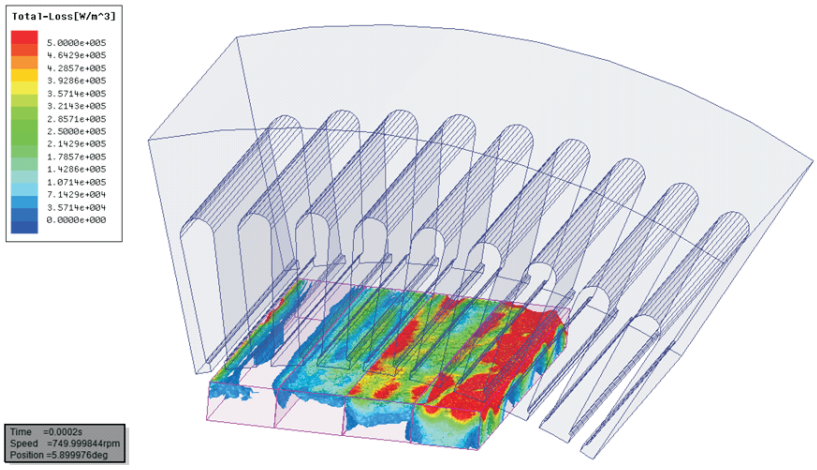

Fig. 4.5 The total loss in the IPMSG magnets with 4 circumferential segments in 3D.

TABLE 4.3: Comparison of the 2D and 3D results for the IPMSG with the magnets segmented into 4 pieces circumferentially.

model	Torque (kNm)	PM loss (kW)
2D	-64.7	2.4
3D	-64.2	2.5

To compare the simulated loss values and the values calculated with the theoretical approach of the magnet segmented into 4 pieces circumferentially, the magnet loss of a 2D model of the IPMSG with no magnet segmentation is investigated. From Maxwell, the magnet loss of the IPMSG without segmentation is

$P_{magnet\_NoSegment} = 3.2\ kW$

Therefore,

$$\frac{P_{magnet\_NoSegment}}{P_{magnet\_FourCirSegments}} = 1.3 \tag{4.7}$$

From the 2D formula, if the magnet is divided into 4 pieces circumferentially

$$R'_{FourCirSegments\_FluxRadial} = 16R_{NoSegment\_FluxRadial} \tag{4.8}$$

$$R'_{FourCirSegments\_FluxCicumferential} = R_{NoSegment\_FluxCicumferential} \tag{4.9}$$

Comparing (4.7), (4.8) and (4.9), it can be concluded that the flux from the stator (armature flux) is both in the radial and in the circumferential direction when it enters the magnets, and that simulations are to be preferred over using the approximative formulas, in this case.

In order to investigate the axial segmentation, only the 3D model of the IPMSG can be used.

The total loss in the magnets with magnets divided into 4 pieces in the circumferential direction and 2 pieces in the axial direction in 3D is plotted in Fig. 4.6.

Table 4.4 shows the comparison of the simulated and calculated results with and without axial segmentation with 2 pieces axially. As can be seen, the numbers agree well between the calculated loss ratio according to (4.2), and the simulated loss ratio.

TABLE 4.4: IPMSG axial segmentation

	Simulated loss without/with axial segmentation	Calculated loss without/with axial segmentation
IPM	1.18	1.17

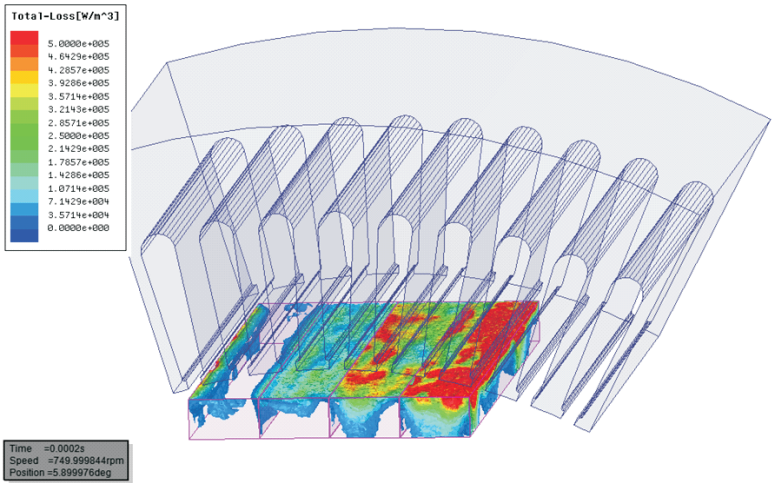

Fig. 4.6 The total loss in the IPMSG magnets with 4 circumferential segments and 2 axial segments in 3D.

4.2 Mechanical restriction

It is observed that the selection of the bridge length (shown in Fig. 4.2) is an important parameter, since decreasing the length of the bridge will increase the air-gap flux density due to saturation of the iron bridges and therefore a higher torque can be obtained from that machine. However, due to the mechanical strength, this parameter cannot be chosen to be very small. In [25] and [26] the importance of the investigation of this parameter at maximum speed for mechanical robustness is discussed. Thus, the structural strength of the rotor is evaluated using FEM simulations (Ansys Workbench).

4.2.1 No-load investigation

The rotor of the IPMSG is simulated at no-load at maximum speed, 750 rpm, and the gravity force is also applied. The yield strength of the material used for the rotor (M235-35A) is 450 MPa [79]. The ambition is to have at least a safety factor of 3 for the stress (This safety factor is used in [25]). The strength analysis of the IPMSG is shown in Fig. 4.7. As can be seen, the magnets get thrown outwards due to centrifugal forces which may create too much stress for the iron bridges to handle without breaking.

It can be seen that the highest stress imposed to the bridge is 135 MPa, which is within the safety limit. Therefore, this rotor can be chosen for the design.

It was observed that the selection of the mesh density is a very important issue. However, a very fine mesh might bring uncorrect results if sharp edges exist.

If the iron bridge is decreased to 1 mm (instead of 3 mm), Fig. 4.8 shows that the stress in the bridges can go up to 350 MPa which is above the safety limit.

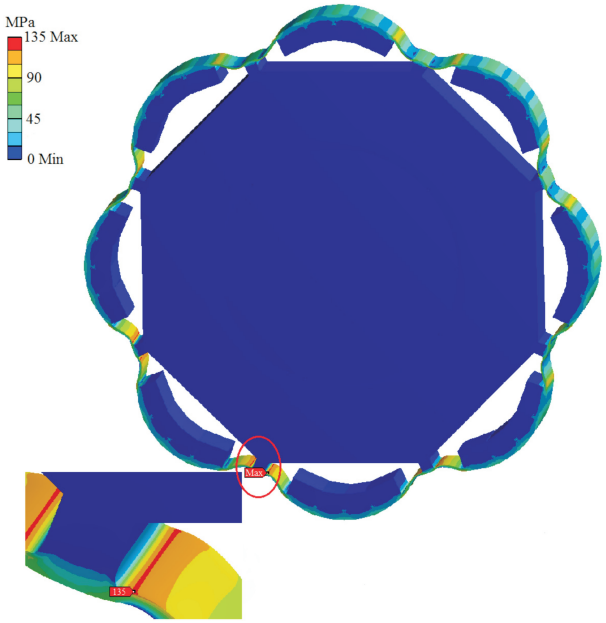

Fig. 4.7 Stress analysis of the IPMSG at no-load and 750 rpm. The deformation of the rotor is exaggerated by a factor of 380 to see the results more clearly.

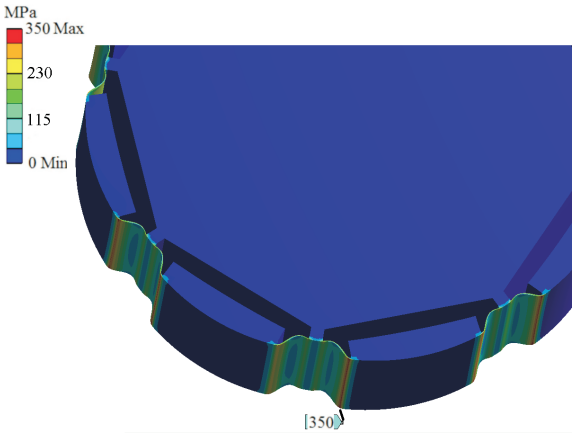

Fig. 4.8 Stress analysis of the IPMSG at no-load and 750 rpm for the iron bridge of 1mm.

4.3 Torque, torque ripple and induced voltage

The torque waveform of the IPMSG can be obtained using Maxwell. By applying sinusoidal currents

$$\begin{aligned} i_a &= \sqrt{2} I_{rms} \cos(2\pi f t + \gamma) \\ i_b &= \sqrt{2} I_{rms} \cos(2\pi f t + \gamma - 120^\circ) \\ i_c &= \sqrt{2} I_{rms} \cos(2\pi f t + \gamma - 240^\circ) \end{aligned} \tag{4.10}$$

to the stator windings the full load torque is obtained in Maxwell. In (5.1), $I_{rms} = 555\ A$, $\gamma = -125^\circ$ and $f = 50\ Hz$. Here, γ (the current phase angle) is the optimal angle which gives the highest torque for the input current. In this way, the MTPA control is used for the machine. This angle that gives the MTPA can be calculated with a formula given in [27]. However, here this angle is calculated through FEM analysis. Different angles are tested for the specific current levels, and the angle that gives the highest torque is chosen.

Figure 4.9 shows the torque waveform as a function of time in one period for the designed IPMSG. As can be seen from the figure, the torque is negative which shows that the machine is operating as a generator. The generator torque is not constant and varies with rotor position. The average torque is -64.5 kNm which corresponds to 5.07 MW power. The torque ripple (peak to peak value of torque) is 15% of the average rated torque.

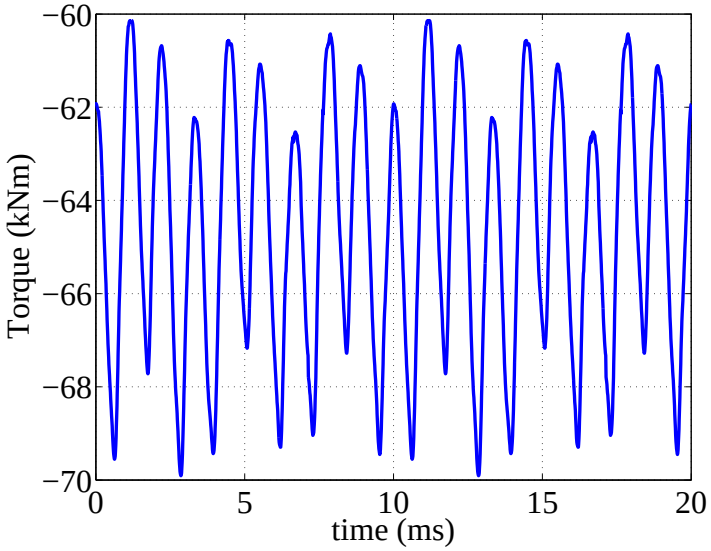

Fig. 4.9 Torque waveform for the IPMSG during one period.

The 3-phase induced voltages of this IPMSG are shown in Fig. 4.10. As can be seen, the induced voltages contain harmonics. The fundamental of the peak phase value of the induced voltages at full load is 5.04 kV. The FFT of different harmonics are shown in Fig. 4.11. The Total Harmonic Distortion (THD) of the induced voltage is 7%.

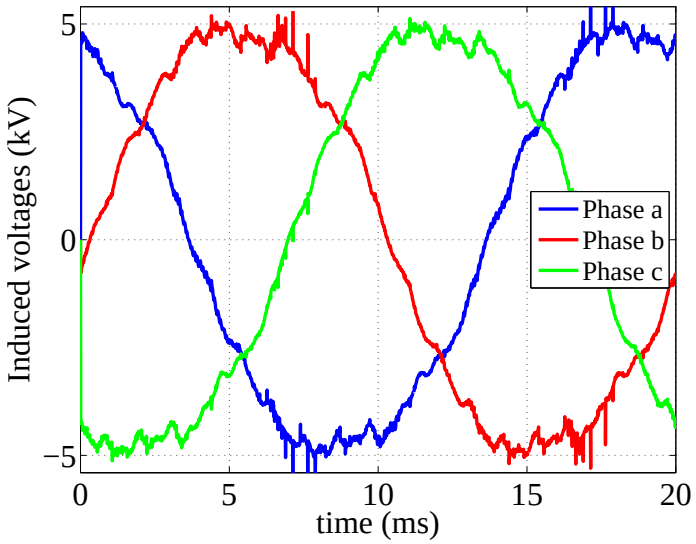

Fig. 4.10 Induced voltage waveforms for IPMSG at full load during one period.

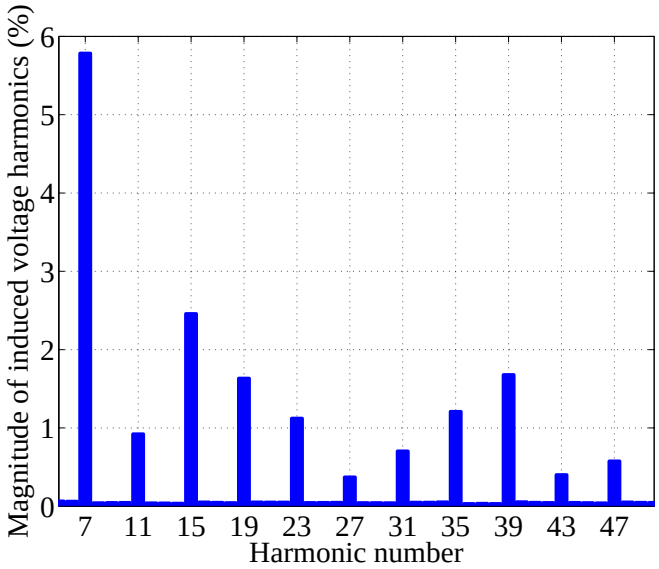

Fig. 4.11 Harmonics amplitude of the induced voltage for the IPMSG in percentage of the fundamental.

4.4 Active material weight

The active material weight for the IPMSG used in this thesis is given in Table 4.5.

TABLE 4.5: Active material weight

Parameter	Value
Stator core steel weight	2397 kg
Rotor core steel weight	1815 kg
Copper weight	1024 kg
Permanent magnet weight	310 kg
Total active material weight	5546 kg

4.5 Demagnetization analysis

As was shown in Section 2.4.5, during the design of the machine the minimum flux density in the PMs has to be verified, in order to not be lower than B_{knee} of the material at the maximum temperature of the machine. Therefore, in this section, this issue is checked. The B-H curve of the permanent magnet used in this thesis is given in Fig. 3.5. As the thermal investigation is not done for the machine in this thesis, it is assumed that the maximum temperature is $100\,^{\circ}\mathrm{C}$. Therefore, according to Fig. 3.5, $B_{knee} = -0.7\ T$. This means that if the flux density in the magnet is in the reverse direction of the magnet magnetization but less than 0.7 T, the magnet won't be demagnetized.

The flux density on the surface of the magnet at no-load is shown in vector form in Fig. 4.12(a). The normal component of this flux density is shown in Fig. 4.12(b), starting at the lower corner of the magnet, for the rotor position shown in Fig. 4.12(a).

The following procedure is done to check demagnetization in the PM. A line is drawn on the surface of each magnet segments (a bit inside the magnet) closer to the air-gap, since this is assumed to be the most vulnerable place of the magnet for demagnetization. In fact, at normal load conditions, it is the trailing edge of the magnet that is the part that is mostly exposed to the armature reaction field (assuming that the armature reaction field is mostly in the q-direction), see [80]. Here, the armature flux is completely in the negative d-direction, and thus the magnet is more evenly exposed to the armature flux. Still, there can be some end effects at magnet upper corners, depending on the rotor position relative to the stator teeth, and any such effects can be studied when the line is drawn in the upper part of the magnet.

To begin with, the full load current (555 A) is applied in the negative d-direction opposite to the direction of magnetization of the magnet. The flux density along the line is checked for different rotor positions. Figure 4.13(a) shows the flux density on the surface of the magnet for the rotor position with the lowest value of flux density. As can be seen, the flux density is still in the direction of magnetization. The normal value of the flux density is shown in Fig. 4.13(b).

For the next step, twice the full load current is applied in the negative direction. Figure 4.14(a)

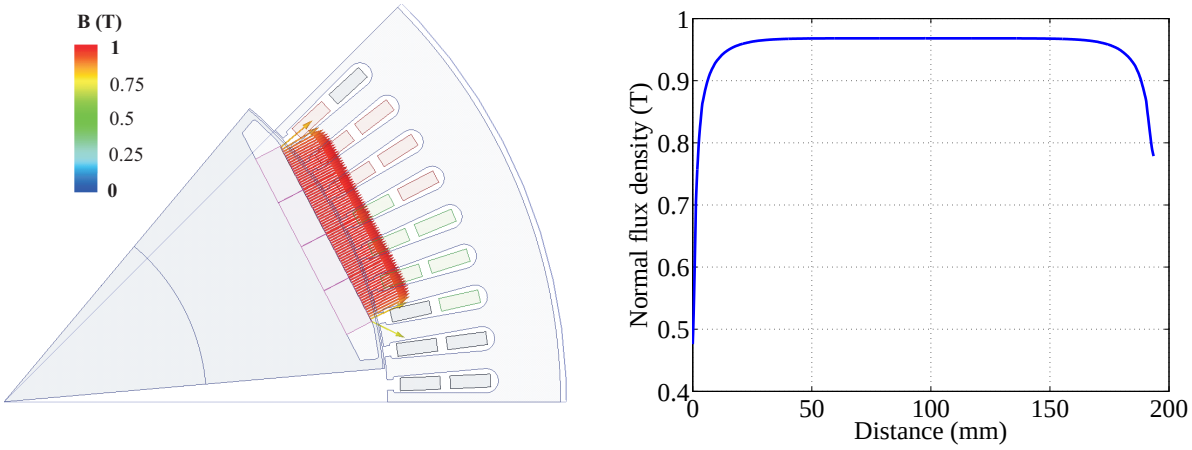

(a) (b)

Fig. 4.12 Magnet flux density at no-load; (a) Magnitude, (b) Normal value.

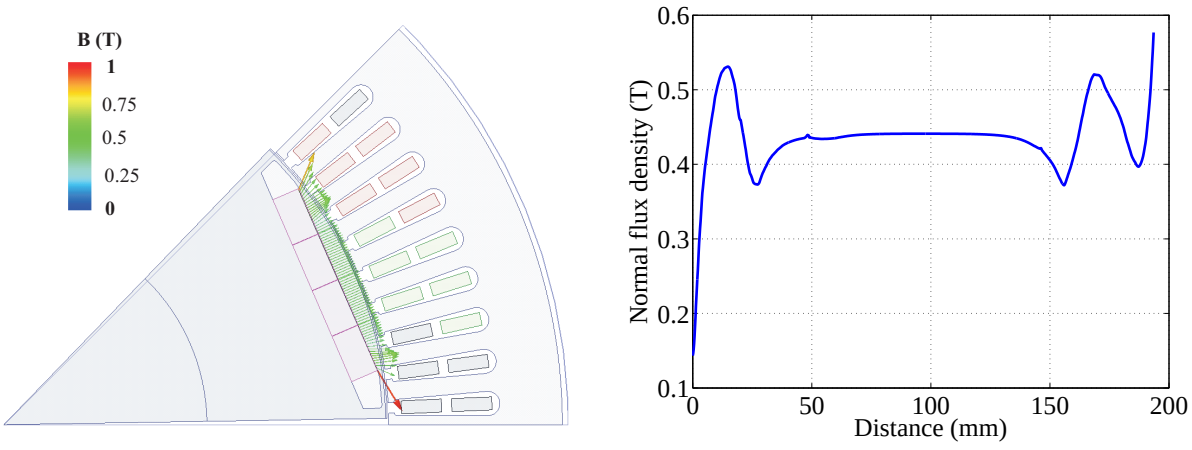

(a) (b)

Fig. 4.13 Magnet flux density at negative full load current; (a) Magnitude, (b) Normal value.

shows the flux density on the surface of the magnet for the rotor position with the lowest value of flux density. As can be seen, the flux density is opposite to the magnetization direction in some areas. The normal value of the flux density is shown in Fig. 4.14(b). As can bee seen, the flux density is greater than B_{knee}. If the temperature goes up to $150\,^{\circ}\mathrm{C}$, this magnet will be demagnetized, since from Fig. 3.5, $B_{knee} = -0.1$ at $150\,^{\circ}\mathrm{C}$.

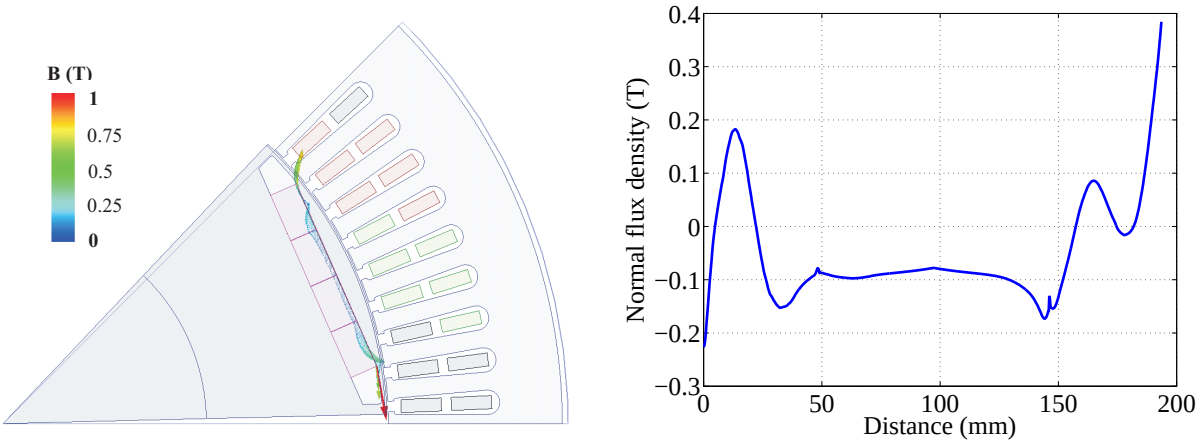

(a) (b)

Fig. 4.14 Magnet flux density at negative twice full load current; (a) Magnitude, (b) Normal value.

4.5.1 Short-circuit current

Using values given in Table 4.6, the short-circuit current in the worst case is

$I_{sc} = 823\ A$

So, the short-circuit current is in the worst case less than twice the rated current (as rated current is 555 A).

TABLE 4.6: Inductance and induced voltage values

Parameter	Value
No-load RMS phase induced voltage	3 kV
No-load L_d	18 mH
Full load L_d	11.6 mH
Frequency	50 Hz

Chapter 5

Rotor design of a permanent magnet assisted synchronous reluctance generator

5.1 One-layer PMa-SynRG

5.1.1 Effect of magnet coverage

The barrier shape of the IPMSG designed in Chapter 4 is modified to be suitable for a multi-layer IPMSG (a PMa-SynRG). The rib (shown in Fig. 5.1) is kept the same as the IPMSG in Chapter 4 (20 mm). The bridge thickness is selected according to the mechanical restriction which will be explained in Section 5.1.4. The bridge thickness is chosen to be 3 mm.

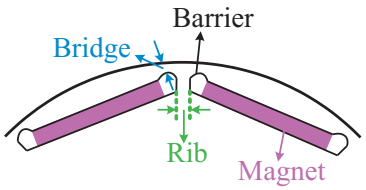

Fig. 5.1 Rib and bridge in a one-layer PMa-SynRM.

When designing barriers for a PMa-SynRM, the barrier thickness radially and circumferentially (see Fig. 5.2) can be different. However, here for the investigation of magnet coverage (defined in Section 3.6.3), the barrier is chosen to have the same thickness both radially and circumferentially. Here, these values are 26 mm.

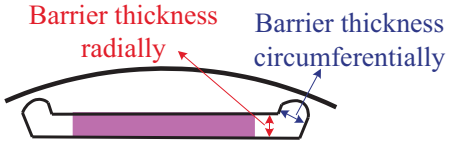

Fig. 5.2 Barrier thickness radially and circumferentially.

For the investigation of the magnet coverage, the magnet width for the highest magnet coverage machine is chosen to be the same as the barrier width (the whole barrier width is filled with a magnet, see Fig. 5.3). The magnet weight for all the different magnet coverages is kept constant (with 0.1% error) and the same as the magnet weight of the IPMSG (310 kg). The lower the magnet coverage (magnet width), the thicker the magnet. So the barrier thickness radially is constant and only magnet thickness increases. Figure 5.3 shows the changes of the magnet thickness in relation to the magnet width.

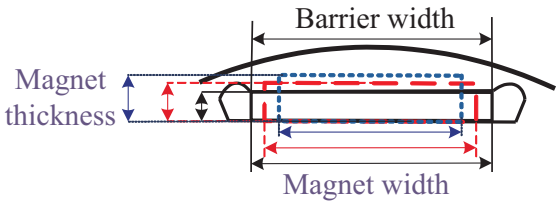

Fig. 5.3 Magnets with different width and thickness but with the same weight.

As was mentioned, the barrier thickness radially is the same as the barrier thickness circumferentially (26 mm). To keep the same thickness for the barrier radially and circumferentially, the magnet coverage could not be more than 74.5%. In order to increase the magnet coverage, the thickness of the barrier circumferentially needs to be decreased. Figure 5.4 shows the two investigated magnet coverages for the one-layer PMa-SynRG.

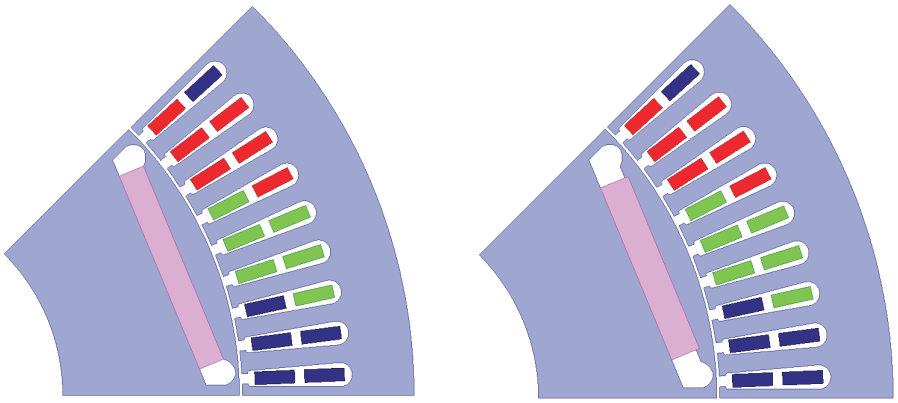

(a) (b)

Fig. 5.4 One-layer PMa-SynRG; (a) Magnet coverage=74.5%, (b) Magnet coverage=68.3%.

Table 5.1 shows the effect of magnet coverage on the MTPA current angle, average torque, torque ripple and magnet loss for the full load current of the IPMSG, which is 555 A.

TABLE 5.1: Effect of magnet coverage on average torque, torque ripple and magnet loss

Coverage (%)	Current angle (deg)	Average torque (kNm)	Torque ripple (%)	Magnet loss (kW)	Magnet weight (kg)	Magnet width (mm)	Magnet thickness (mm)
74.5	-129	-63.37	8.3	0.94	310	209	26
73	-128.5	-63.41	9.2	0.95	310	205	26.5
71.5	-128	-63.13	8.8	0.95	310	201	27.1
70	-128	-62.76	9.1	0.94	310	197	27.6
69.3	-127.5	-62.38	10	0.94	310	195	27.9
68.3	-127.5	-62.21	10	0.934	310	192	28.3
67.3	-127	-62.05	10	0.98	310	189	28.7
66	-127	-61.63	12	0.97	310	186	29.2
65.3	-126.5	-61.46	10	0.99	310	184	29.5

As can bee seen from Table 5.1, higher magnet coverages seem to give a higher average torque and a lower torque ripple. Meanwhile, it does not affect the magnet losses significantly. The maximum torque is found at a magnet coverage above 70%, and more specifically, in this case, the optimum value seems to be 73%. This can be compared to the best magnet coverage for the SPMSGs, which are 76%, as seen in Section 3.6.3.

5.1.2 Effect of the thickness of the barrier circumferentially

Here the thickness of the barrier circumferentially (see Fig. 5.2 and Fig. 5.5) in the machine with the magnet coverage of 68.3% in the previous section is varied to see the effect on average torque, torque ripple and magnet loss. The barrier thickness radially is kept constant.

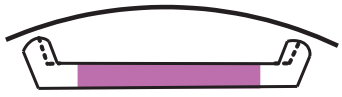

Fig. 5.5 Variation of the barrier thickness circumferentially.

Figure 5.6 shows two of the investigated barrier thickness circumferentially for the one-layer PMa-SynRG.

The results of different barrier thickness circumferentially are given in Table 5.2. The full load current of the IPMSG which is 555 A is used here as well. As can be seen, the average torque is higher if the barrier thickness circumferentially is bigger than the barrier thickness radially. The reason could be that the magnet flux leakage goes down when the barrier thickness circumferentially increases, and therefore the alignment torque becomes more powerful.

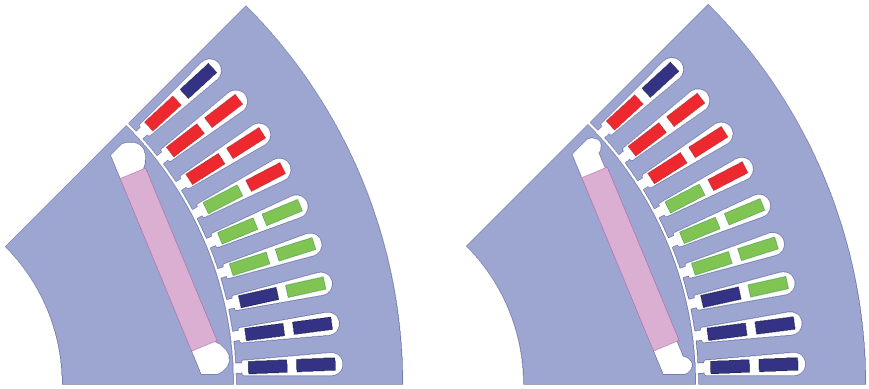

(a) (b)

Fig. 5.6 Different barrier thickness circumferentially; (a) 33.6 mm, (b) 18.3 mm.

TABLE 5.2: Effect of barrier thickness circumferentially on average torque, torque ripple and magnet loss

Barrier thickness circumferentially (mm)	Barrier thickness radially (mm)	Current angle (deg)	Average torque (kNm)	Torque ripple(%)	Magnet loss (kW)	Magnet weight (kg)
33.6	26	-127.5	-62.8	13	0.94	310
26	26	-127.5	-62.2	10	0.93	310
18.3	26	-127	-61.8	20	0.92	310
9.8	26	-126.5	-60.9	27	0.91	310

5.1.3 Effect of barrier depth

The one-layer PMa-SynRG with the magnet coverage of 68.3% in Section 5.1.1 is chosen for the investigation of the effect of the depth of the barrier. The barrier and magnet thicknesses are kept constant. The barrier end length is increased to position the barrier closer to the shaft (see Fig. 5.7).

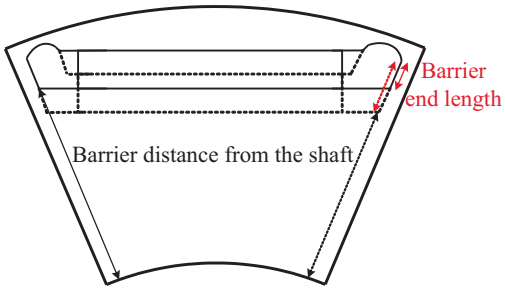

Fig. 5.7 Varying barrier distance from the shaft.

The effect of the barrier depth for full load current (555 A) is shown in Table 5.3. As can be

seen, the closer the barrier is to the shaft, the less magnet loss. Also, as expected, the average torque decreases (as the magnet flux path is increased), however, moderately. The torque ripple stays fairly constant. Figure 5.8 shows two of the investigated barrier depths.

TABLE 5.3: Effect of barrier depth on average torque, torque ripple and magnet loss

Distance from shaft (mm)	Current angle (deg)	Average torque (kNm)	Torque ripple (%)	Magnet loss (kW)
143	-127.5	-62.2	10.3	0.93
138	-129	-62.1	8.8	0.68
133	-131	-62.1	9	0.51
128	-133	-61.3	10	0.38
123	-135	-61.4	10.8	0.3

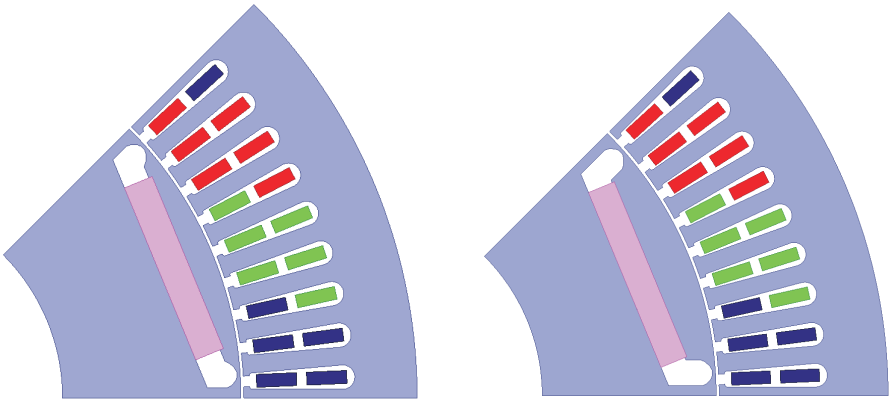

(a) (b)

Fig. 5.8 Varying barrier distance from the shaft; (a) Distance to the shaft=143 mm, (b) Distance to the shaft=128 mm.

5.1.4 Effect of bridge thickness on mechanical stress and average torque

The bridge thickness in Section 5.1.1 was chosen according to the mechanical stress requirement. As in Section 4.2.1, for the mechanical investigation, the rotor of the machine is simulated at no-load and at maximum speed, 750 rpm, and the gravity force is also applied. The material that is used for the one-layer PMa-SynRG is the same as the material of the IPMSG. Therefore, the yield strength of the material is 450 MPa [79]. To keep the safety factor of 3 as in the IPMSG, the maximum stress should not be more than 150 MPa.

Variation of magnet coverage did not have a significant effect on the selection of the bridge thickness. Therefore, the results that are shown here are for the machine with a magnet coverage of 74.5% from Section 5.1.1. The stress for three different bridge thicknesses (1, 2 and 3 mm) is investigated. If the bridge thickness is chosen to be 1 mm, as can be seen from Fig. 5.9, the

maximum von Mises stress is almost 400 MPa which is higher than the assumed safety limit. Therefore, the bridge thickness must be increased to be able to handle the stress without a risk of breaking.

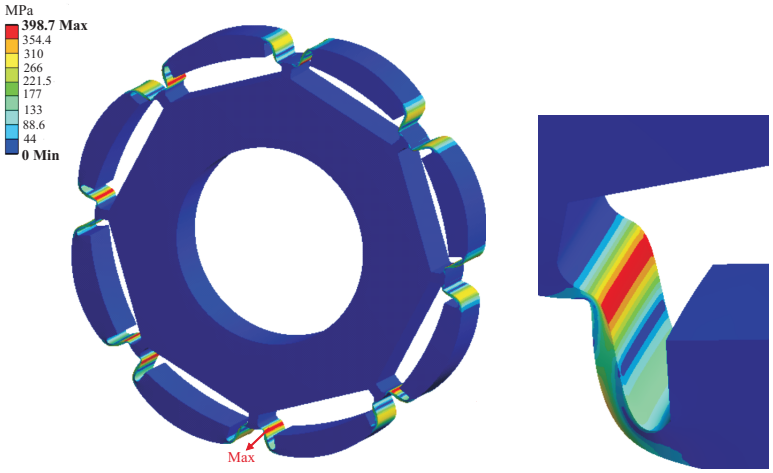

(a) (b)

Fig. 5.9 Stress investigation for a one-layer PMa-SynRG with bridge thickness=1; (a) Whole machine, (b) Maximum stress magnified.

Figure 5.10 shows the stress analysis for a bridge thickness of 2 mm. As can be seen in the figure, the maximum stress is still not within the safety limit.

The bridge thickness is therefore increased to 3 mm. As can be seen in Fig. 5.11, the maximum stress is now in the safety limit. Therefore, this bridge thickness is used in Section 5.1.1.

The increase in the bridge thickness has an effect on the average torque. Table 5.4 shows the decrease of the average torque in relation to the bridge thickness for this machine.

TABLE 5.4: Effect of bridge thickness on average torque for one-layer machine

Bridge thickness (mm)	Average torque (kNm)
3	-63.4
2	-64.1
1	-64.3

5.2 Two-layer PMa-SynRG

The magnet thickness of the IPMSG designed in Chapter 4, is divided into two to make the initial two layer PMa-SynRG. For the first case, the effort is to keep the width of the magnets equal. As the magnet thickness for the IPMSG was 28 mm, the thickness of each magnet should

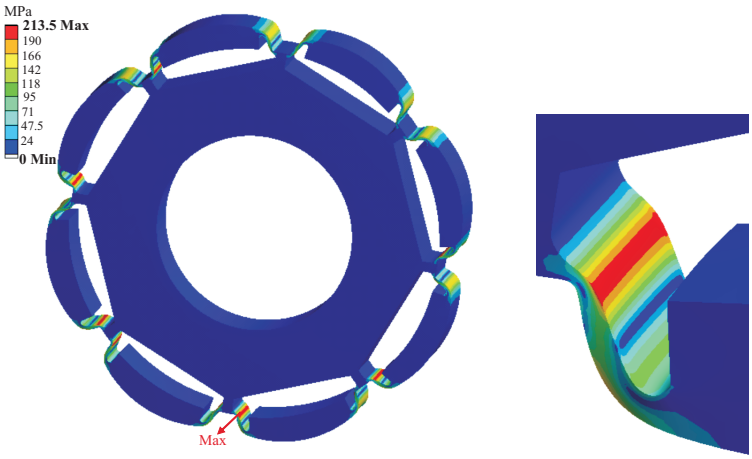

(a) (b)

Fig. 5.10 Stress investigation for a one-layer PMa-SynRG with bridge thickness=2; (a) Whole machine, (b) Maximum stress magnified.

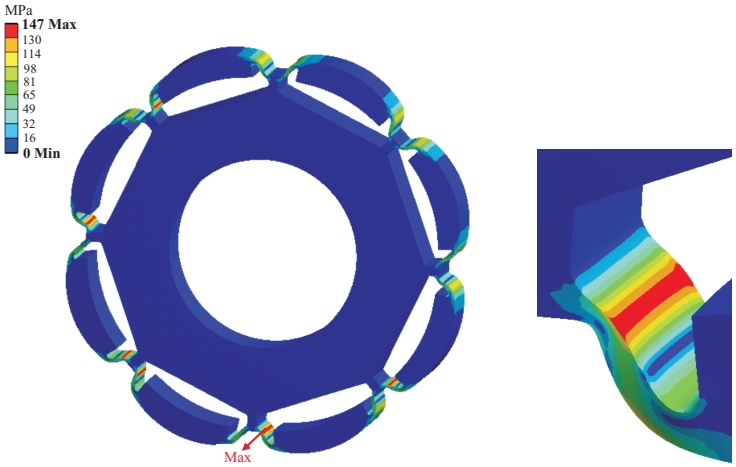

(a) (b)

Fig. 5.11 Stress investigation for a one-layer PMa-SynRG with bridge=3; (a) Whole machine, (b) Maximum stress magnified.

be 14 mm. The magnet area is kept the same as the magnet area of the IPMSG. For the barrier close to the air-gap (barrier 1), the magnet fills the whole barrier and the magnet in barrier 2 has the same width as the magnet in barrier 1. Since the magnet area of the IPMSG per pole is 5426 mm^2, the magnet width should be 193.8 mm. The thickness of the barrier circumferentially is the same as the thickness of the barrier radially, as well as the magnet thickness, which is 14 mm. The space between barrier 1 and barrier 2 radially and circumferentially is 9 mm. In this way, the rib is kept to be 20 mm. The parameters are shown in Fig. 5.12. This two-layer PMa-SynRG with the same magnet width in both layers is called 2-layer1. Figure 5.13(a) shows the cross-section of the 2-layer1. The bridge thicknesses values are given in Table 5.5. The selection of the bridge thickness is explained in Section 5.2.1.

TABLE 5.5: Bridge thickness values for two-layer machine

Bridge 1 thickness (mm)	Bridge 2 thickness (mm)
2	3

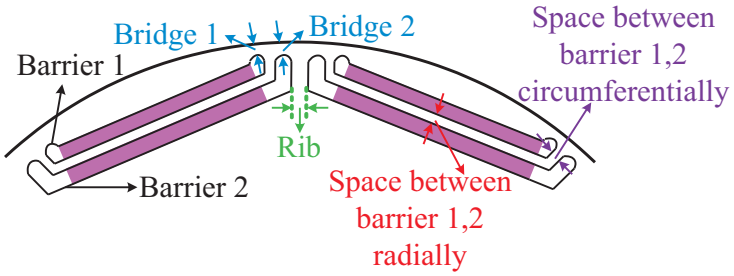

Fig. 5.12 Two-layer PMa-SynRG parameters.

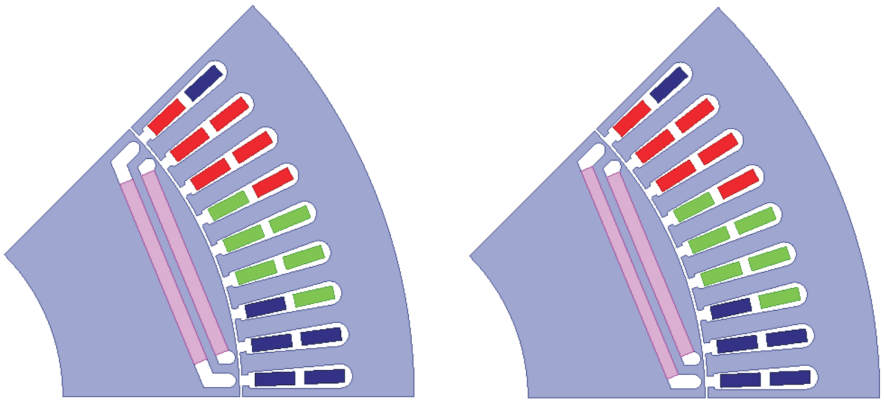

(a) (b)

Fig. 5.13 Cross-section of the two-layer PMa-SynRG; (a) 2-layer1, (b) 2-layer2.

For the second design of the two-layer PMa-SynRG, the magnet width in barrier 2 has increased to fill the whole barrier 2 width. To keep the weight of the magnet constant, the magnet thickness

as well as the barrier thickness radially has been decreased. The space between barrier 1 and barrier 2 radially and circumferentially is kept to be 9 mm as in 2-layer1. To decrease the magnet thickness and barrier thickness radially, the barrier depth has changed. Barrier 1 is the same as the 2-layer1 machine, without any changes. This machine is called 2-layer2. These changes are shown in Fig. 5.14. Figure 5.13(b) shows the cross-section of the 2-layer2. The values of thickness, width and weight of each magnet for both machines are given in Table 5.6.

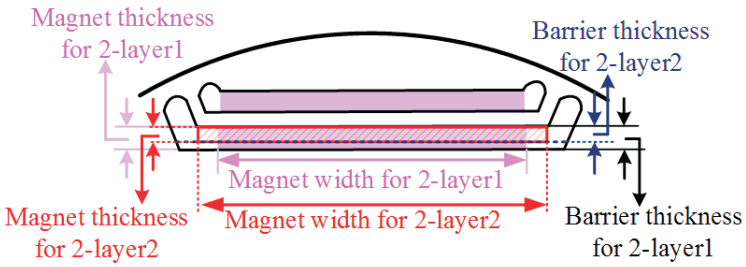

Fig. 5.14 Change of magnet thickness and barrier thickness circumferentially for the design of 2-layer2.

TABLE 5.6: 2-layer PMa-SynRG magnet dimensions and weight

	Magnet 1 thickness (mm)	Magnet 2 thickness (mm)	Magnet 1 width (mm)	Magnet 2 width (mm)	Magnet 1 weight (kg)	Magnet 2 weight (kg)
2layer1	14	14	193	193	155	154
2layer2	14	12	193	224	155	154

The full load current of the IPMSG (555 A) is applied for the two-layer machines as well. Table 5.7 shows the results of the MTPA current angle, average torque, torque ripple and magnet loss for the two-layer machines as well as a comparison with the IPMSG in Chapter 4.

TABLE 5.7: Comparison of the IPMSG, 2-layer1 and 2-layer2

Machine type	Current angle (deg)	Alignment torque (kNm)	Reluctance torque (kNm)	Average torque (kNm)	Torque ripple (%)	Magnet loss (kW)	Magnet weight (kg)
IPMSG	-125	-45.1	-19.5	-64.6	15	2.9	310
2-layer1	-132	-38.2	-27.4	-65.6	21	2.4	310
2-layer2	-132.5	-38.6	-27.7	-66.3	24	2.8	310

The results show that 2-layers are better than one-layer (yielding a higher torque and lower magnet loss), since the reluctance torque is increased. However, the torque ripple is increased. This result confirms investigations conducted by others, for instance [35]. Regarding the different PMa-SynRG designs, 2-layer2 yields slightly higher average torque than 2-layer1 (both the reluctance torque and the alignment (magnet) torque are increased). However, 2-layer2 also

yields higher torque ripple and higher magnet loss. The magnet loss in the 2-layer machines is slightly lower compared to the IPMSG even though the magnet in the IPMSG is segmented.

5.2.1 Effect of bridge thickness on mechanical stress and average torque

In the same way as before, to find out suitable bridge thicknesses, the rotor of the machine is simulated at no-load and at maximum speed, 750 rpm, and the gravity force is applied as well. The same maximum stress limit as in Section 5.1.4 is also applied here. That means that the maximum stress should not be more than 150 MPa. The bridge thickness selection for the 2-layer1 and 2-layer2 are fairly similar. Therefore, here the results of the 2-layer2 are given. The stress for three different bridge thicknesses is investigated. If bridge 1 and 2 are 2 mm (bridge 1 and 2 are shown in Fig. 5.12), then the maximum stress is 230 MPa which is higher than the limit. The stress analysis for this case is shown in Fig. 5.15(a). To have the maximum stress within the limitation, Fig. 5.15(b), shows that bridge1=2 mm and bridge2=3 mm.

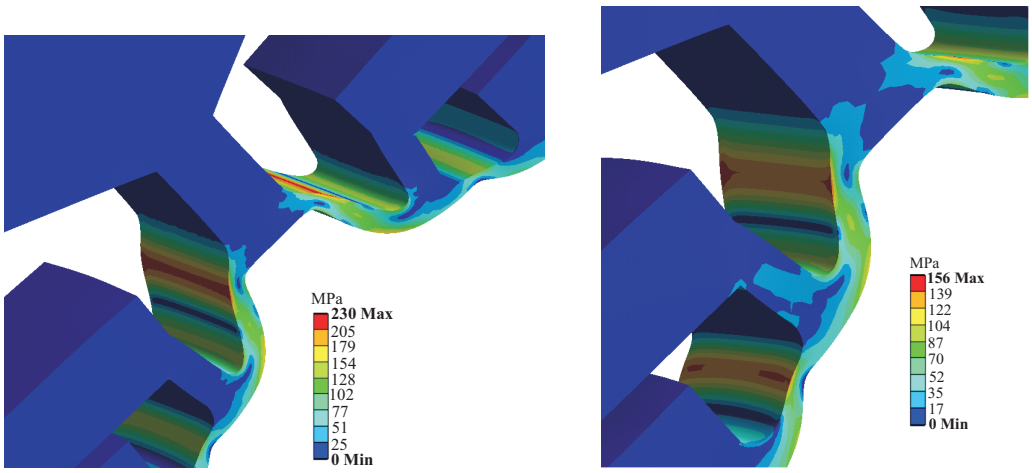

(a) (b)

Fig. 5.15 Stress analysis for the 2-layer2 machine; (a) Bridge1=2 mm and bridge2=2 mm, (b) Bridge1=2 mm and bridge2=3 mm.

The stress analysis is also carried out for bridge1=1 mm and bridge2=3 mm. Figure 5.16 shows this investigation. As can be seen, the maximum stress has shifted to the first bridge and it is higher than the safety limit.

The effect of bridge thickness on average torque for the 2-layer2 machine is shown in Table 5.8.

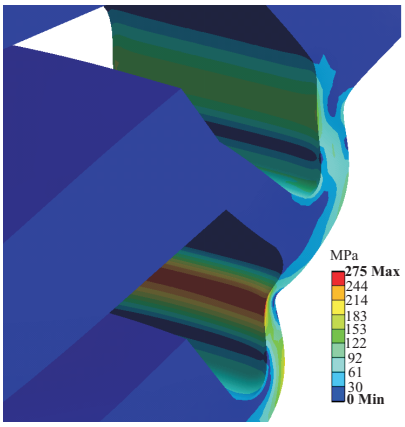

Fig. 5.16 Stress analysis for the 2-layer2 machine with bridge1=1 mm, bridge2=3 mm.

TABLE 5.8: Effect of bridge thickness on average torque for 2-layer2 machine

Bridge 1 thickness (mm)	Bridge 2 thickness (mm)	Average torque (kNm)
2	2	-66.2
1	3	-66.7
2	3	-66.3

5.3 Three-layer PMa-SynRG

In this section, the layers are increased more to see the effect on the performance of the machine. As the number of layers increases, the magnet width in barrier 1 needs to be decreased to be able to fit more layers in the rotor. The initial three-layer PMa-SynRG is designed with the magnets having the same length. The rib and space between the magnets are similar to the two-layer machines. The effort is to keep the total magnet weight in the three barriers the same as the IPMSG. The selection of the bridge thicknesses which are given in Table 5.9 is explained in Section 5.3.1. Bridge 1 is the bridge of the barrier closest to the air-gap. This machine is called 3-layer1. Figure 5.17(a) shows the cross-section of this machine.

TABLE 5.9: Bridge thickness values for three-layer machines

Bridge 1 thickness (mm)	Bridge 2 thickness (mm)	Bridge 3 thickness (mm)
2	2	3

For the second design, magnet and barrier 1 are the same as the magnet and barrier 1 in 3-layer1, without any changes. The magnet width in barrier 2 is increased to fill the whole barrier

2 width. To keep the weight of the magnet constant, the magnet thickness as well as the barrier thickness radially has been decreased. The space between barrier 1 and barrier 2 radially and circumferentially is kept constant as in the two-layer machine. To decrease the magnet thickness and barrier thickness radially, the barrier depth from the shaft has been increased. The magnet width in barrier 3 has also increased to the same width as the magnet width in barrier 2. Consequently, the depth of barrier 3 is also increased from the shaft. This machine is called 3-layer2. Figure 5.17(b) shows the cross-section of this machine.

For the third design, the magnet width in barrier 3 has been increased to fill the whole barrier 3 width. The depth of barrier 3 from the shaft has increased more to keep the magnet weight constant. This machine is called 3-layer3. The cross-section of this machine is illustrated in Fig. 5.17(c). The values of thickness and width as well as the weight of each magnet for three designed machines are given in Table 5.10 and Table 5.11, respectively.

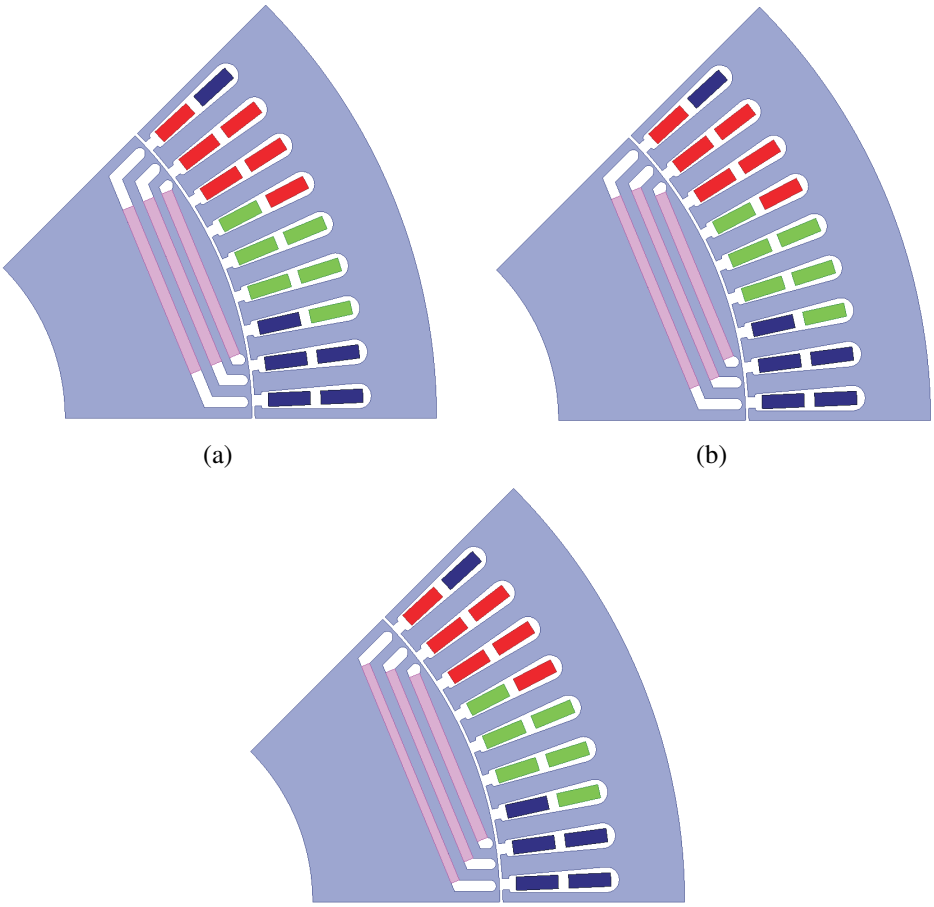

(a) (b)

(c)

Fig. 5.17 Cross-section of the 3-layers machines; (a) 3-layer1, (b) 3-layer2, (c) 3-layer3.

TABLE 5.10: Magnet dimensions for the three investigated 3-layer PMa-SynRG

	Magnet 1 thickness (mm)	Magnet 2 thickness (mm)	Magnet 3 thickness (mm)	Magnet 1 width (mm)	Magnet 2 width (mm)	Magnet 3 width (mm)
3-layer1	10.4	10.8	10.8	167	167	167
3-layer2	10.4	9.4	9.6	167	193	193
3-layer3	10.4	9.4	8.2	167	193	221

TABLE 5.11: Magnet weight for the three investigated 3-layer PMa-SynRG

	Magnet 1 weight (kg)	Magnet 2 weight (kg)	Magnet 3 weight (kg)
3-layer1	100	103	103
3-layer2	100	103	106
3-layer3	100	103	104

As was mentioned, the barrier thickness radially is the same as the magnet thickness which can be found in Table 5.10. The barrier thicknesses circumferentially in the three 3-layer machines are kept similar and close to the magnet thicknesses in 3-layer1. The values are given in Table 5.12. The full load current of the IPMSG which is 555 A is applied to all the three-layer machines and the values of the MTPA current angle, average torque, torque ripple and magnet loss are given in Table 5.13.

TABLE 5.12: Barrier thickness circumferentially for all the three investigated 3-layer PMa-SynRG

	Barrier 1 thickness (mm)	Barrier 2 thickness (mm)	Barrier 3 thickness (mm)
All the 3-layer machines	10.4	10.7	10.9

TABLE 5.13: Three-layer machines performances

Machine type	Current angle (deg)	Alignment torque (kNm)	Reluctance torque (kNm)	Average torque (kNm)	Torque ripple (%)	Magnet loss (kW)	Magnet weight (kg)
3-layer1	-136	-34.3	-32.6	-66.9	7.9	3.8	306
3-layer2	-137.5	-34.7	-34	-68.7	7.3	4.7	309
3-layer3	-137.5	-35.2	-33.7	-68.9	7.2	4.7	307

As can be seen from Table 5.13, spreading the magnet inside the barrier increases both alignment and reluctance torque. The increase of the reluctance torque could be because of the phenomenon which was also seen in Section 5.1.2 (barrier thickness circumferentially is bigger

than the barrier thickness radially). It seems that spreading the magnet inside the whole barrier instead of concentrating the magnet in the middle of the barrier influences the torque ripple as well. As far as the comparison with the 2-layer machine goes, it seems that the 3-layer machine has lower torque ripple. Increasing the layers has also improved the reluctance torque yielding higher average torque. However, increasing the layers (3-layer compared to 2-layer machines) decreases the alignment (magnet) torque due to more leakage.

5.3.1 Effect of bridge thickness on mechanical stress and average torque

For investigating suitable bridge thicknesses, the same as before, the rotor of the machine is simulated at no-load and at maximum speed, with considering the gravity force. The same maximum stress limit (Max. 150 MPa) as in Section 5.1.4 is applied here as well. The results that are given here belong to the 3-layer1 machine. The stress analysis for 3-layer2 and 3-layer3 are almost similar to the 3-layer1 machine. First all the bridges are selected to be 2 mm. As can be seen in Fig. 5.18(a), the maximum stress is higher than the limit. Therefore, bridge 3 which holds the highest stress is increased to 3 mm. The stress analysis for this case is shown in Fig. 5.18(b). Although there are small parts where the stress is higher than the limit, but since it is not in the whole length and most of the stress is lower than 155 MPa, these thicknesses are good enough to select.

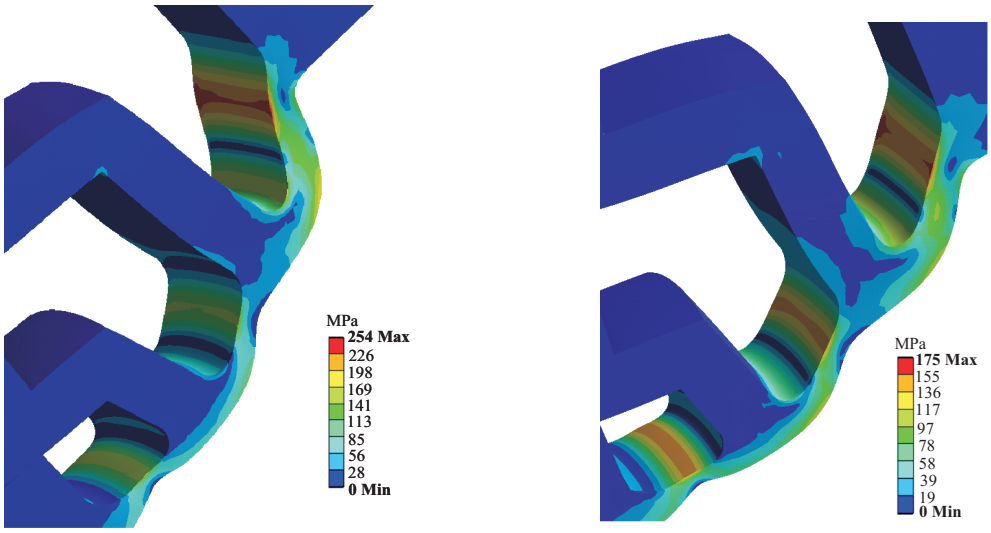

(a) (b)

Fig. 5.18 Stress analysis for the 3-layer1 machine; (a) Bridge1=2 mm, bridge2=2 mm and bridge3=3 mm, (b) Bridge1=2 mm, bridge2=2 mm and bridge3=3 mm.

Table 5.14 shows that average torque is not affected by increasing bridge 3 thickness.

TABLE 5.14: Effect of bridge thickness on average torque for 3-layer1 machine

Bridge 1 thickness (mm)	Bridge 2 thickness (mm)	Bridge 3 thickness (mm)	Average torque (kNm)
2	2	2	-66.9
2	2	3	-66.9

5.4 Four-layer PMa-SynRG

The position of the barriers 1, 2 and 3 towards the stator teeth in the 3-layer1 machine is kept the same and one layer is added in the middle. Magnet 1 and 2 fills the whole barrier, Magnet 3 and 4 follow the length of magnet 2. This machine is called 4-layer1. For the second design, magnet width in barrier 3 is increased to fill the whole barrier 3 width. In the same way as before, to keep the weight of the magnet constant, the magnet thickness as well as the barrier thickness radially has been decreased. The magnet length in barrier 4 is also increased to have the same length as the magnet in barrier 3. Consequently, the thickness of the magnet and barrier 4 radially has been decreased to keep the magnet weight constant. This machine is called 4-layer2. For the third design of the four-layer machine, magnet width in barrier 4 has also increased to fill the barrier 4 width. The magnet thickness as well as the barrier thickness radially has been decreased to keep the magnet weight constant. This machine is called 4-layer3. The cross-sections of these machines are shown in Fig. 5.19. Table 5.15 shows the bridge thicknesses.

TABLE 5.15: Bridge thickness values for four-layer machines

Bridge 1 thickness (mm)	Bridge 2 thickness (mm)	Bridge 3 thickness (mm)	Bridge 4 thickness (mm)
2	2	3	4

The full load current of the IPMSG which is 555 A is applied to all the four-layer machines and the values of the MTPA current angle, average torque, torque ripple and magnet loss are given in Table 5.16.

TABLE 5.16: Four-layer machines performances

Machine type	Current angle (deg)	Alignment torque (kNm)	Reluctance torque (kNm)	Average torque (kNm)	Torque ripple (%)	Magnet loss (kW)	Magnet weight (kg)
4-layer1	-141.5	-28.6	-39.3	-67.9	15.7	4	309
4-layer2	-142	-29.8	-39.4	-69.2	14.4	4	309
4-layer3	-142.5	-30	-39.5	-69.6	14.7	4.1	308

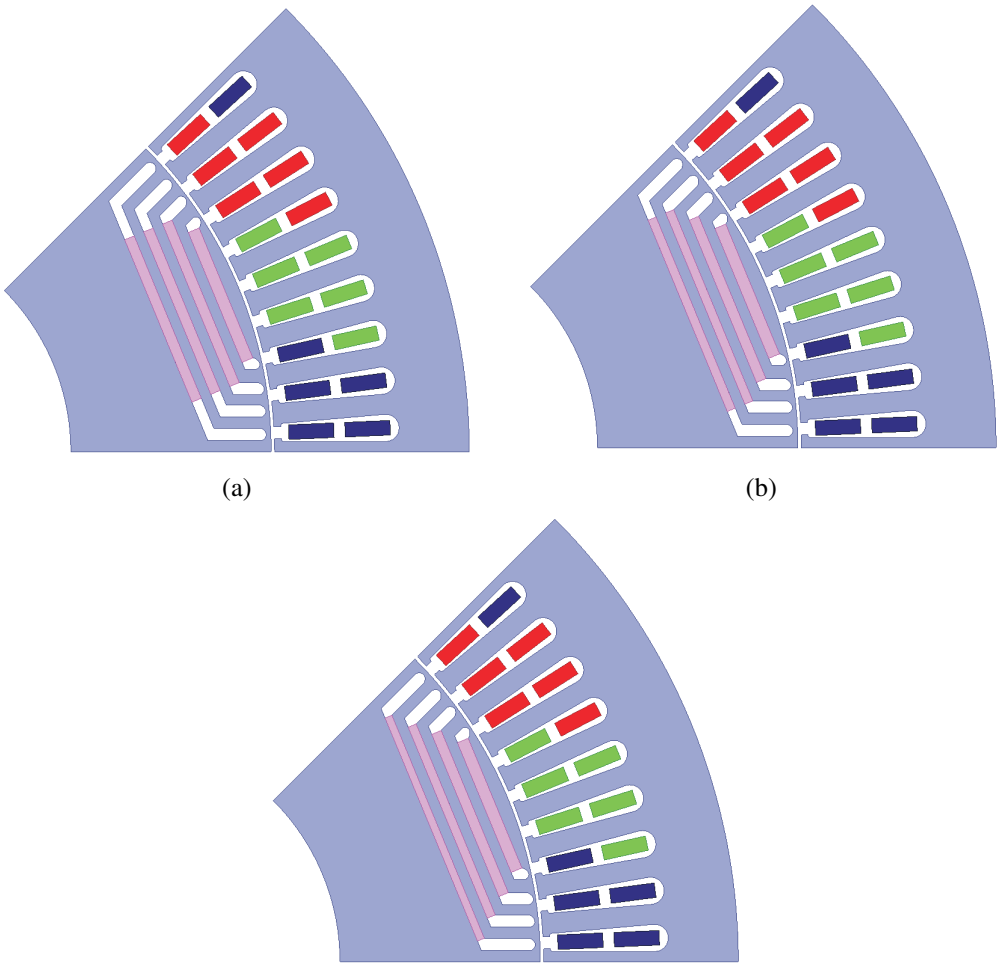

Fig. 5.19 Cross-section of 4-layers machines; (a) 4-layer1, (b) 4-layer2, (c) 4-layer3.

5.5 Five-layer PMa-SynRG

The position of the barriers 1, 2, 3 and 4 towards stator teeth in the 4-layer1 machine is kept the same and one layer is added in the middle. Magnet 1, 2 and 3 fills the whole barrier width, Magnet 4 and 5 follow the width of magnet 3. This machine is called 5-layer1. For the second design, the magnet width in barrier 4 is increased to fill the whole barrier 4 width. Just as before, to keep the weight of the magnet constant, the magnet thickness as well as the barrier thickness radially has been decreased. The magnet length in barrier 5 is also increased to have the same length as the magnet in barrier 4. Consequently, the thickness of the magnet and barrier 5 radially has been decreased to keep the magnet weight constant. This machine is called 5-layer2. For the third design of the five-layer machine, the magnet width in barrier 5 is also increased to fill the barrier 5 width. The magnet thickness as well as the barrier thickness radially has been decreased to keep the magnet weight constant. This machine is called 5-layer3. The cross-sections of these machines are shown in Fig. 5.20. Table 5.17 shows the bridge thicknesses.

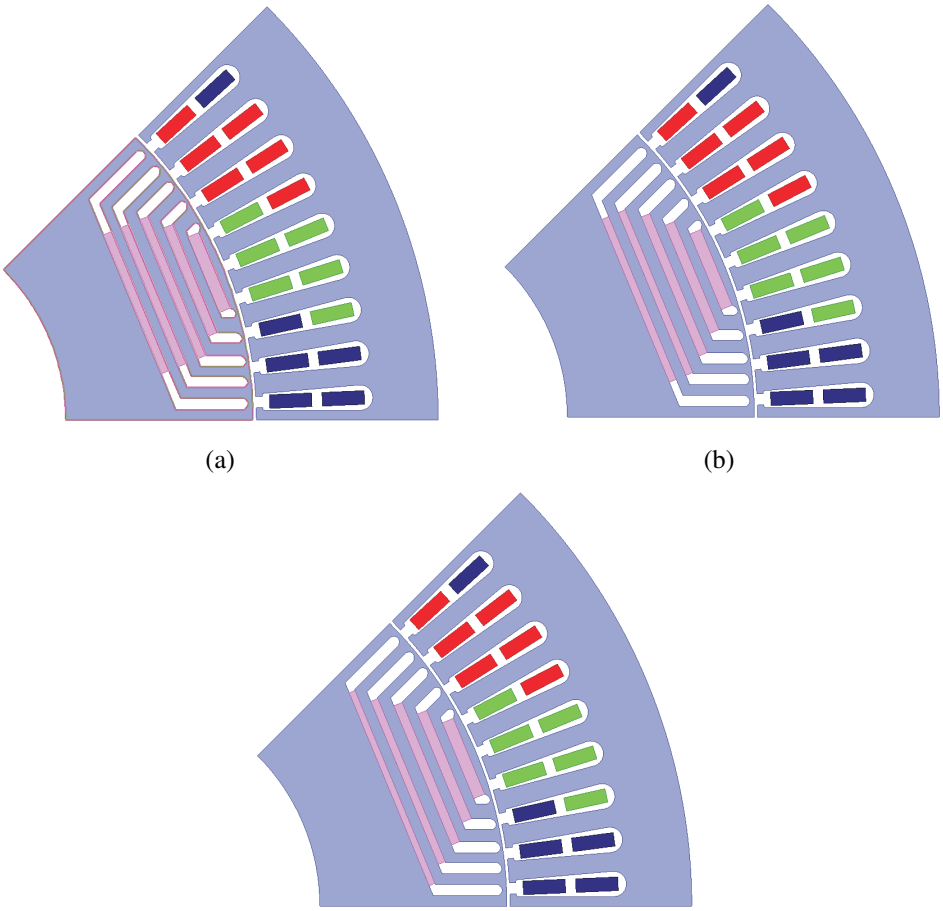

(a) (b)

(c)

Fig. 5.20 Cross-section of 5-layers machines; (a) 5-layer1, (b) 5-layer2, (c) 5-layer3.

TABLE 5.17: Bridge thickness values for five-layer machines

Bridge 1 thickness (mm)	Bridge 2 thickness (mm)	Bridge 3 thickness (mm)	Bridge 4 thickness (mm)	Bridge 5 thickness (mm)
2	2	2	3	4

The full load current of the IPMSG which is 555 A is applied to all the five-layer machines and the values of the MTPA current angle, average torque, torque ripple and magnet loss are given in Table 5.18.

TABLE 5.18: Five-layer machines performances

Machine type	Current angle (deg)	Alignment torque (kNm)	Reluctance torque (kNm)	Average torque (kNm)	Torque ripple (%)	Magnet loss (kW)	Magnet weight (kg)
5-layer1	-145.5	-23.7	-43.7	-67.4	9.8	4.3	310
5-layer2	-145.5	-24.9	-43.6	-68.5	9.5	4.2	310
5-layer3	-145.5	-25.4	-43.5	-68.9	9.7	4.2	310

5.5.1 effect of slope in the end barriers

The slope of the barrier at the end (see Fig. 5.21) might effect the average torque, since it can influence the q inductance. To check this, barrier 4 and 5 in the 5-layer1 are changed a bit to see the effect of the slope of the barriers.

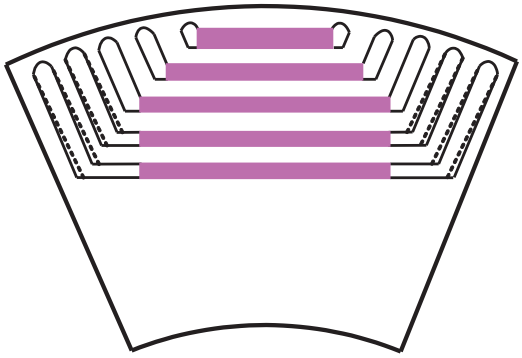

Fig. 5.21 Changing slope of end barriers.

The average torque increased from -67.4kNm to -67.6 kNm, since L_q increases.

5.6 Six-layer PMa-SynRG

The barriers of the 5-layer1 are placed closer together to see that increasing the number of barrier will not help for a better performance. The cross-section of the machine is shown in

Fig. 5.22. Table 5.19 shows the bridge thicknesses.

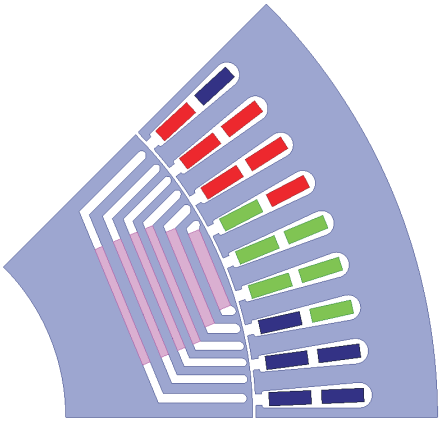

Fig. 5.22 Cross-section of the 6-layer machine.

TABLE 5.19: Bridge thickness values for six-layer machine

Bridge 1 thickness (mm)	Bridge 2 thickness (mm)	Bridge 3 thickness (mm)	Bridge 4 thickness (mm)	Bridge 5 thickness (mm)	Bridge 6 thickness (mm)
2	2	2	2	3	5

The full load current of the IPMSG which is 555 A is applied and the values of the MTPA current angle, average torque, torque ripple and magnet loss are given in Table 5.20.

TABLE 5.20: Six-layer machine performance

Machine type	Current angle (deg)	Alignment torque (kNm)	Reluctance torque (kNm)	Average torque (kNm)	Torque ripple (%)	Magnet loss (kW)	Magnet weight (kg)
6-layer	-147.5	-19.9	-46.9	-66.8	13.4	3.6	309

As can be seen from the table average torque decreases.

5.7 Electromagnetic design of a 5 MW PMa-SynRG

As was seen in the last sections, spreading the magnet in the whole barrier width gives a higher average torque. Therefore, for the design of this PMa- SynRG, magnets fill the whole width of the barriers. It was also seen that the 4-layer3 gives the highest average torque compared to the other machines. The 5-layer3 has 1% lower average torque compared to 4-layer3, however, it has 34% lower torque ripple. Therefore, a 5 layer machine is selected.

The magnet weight of the 5-layer3 is decreased to get approximately the same average torque as the IPMSG (-64.5 kNm) in Chapter 4 for the same full load current as in IPMSG (555 A). The stator of the machine is the same as the stator of the IPMSG.

The position of the end barriers towards the stator slots is slightly adjusted to reduce the torque ripple more. The end of the barriers are slanted, since it was shown in Section 5.5.1 that the slope of the barriers affects the average torque. The cross-section of the machine is shown in Fig. 5.23.

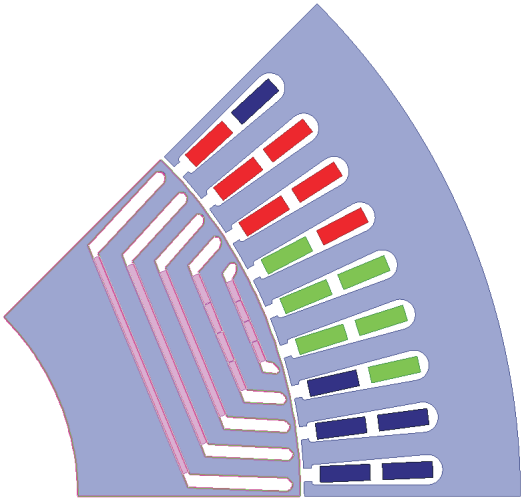

Fig. 5.23 Cross-section of the PMa-SynRG.

As can bee seen from Fig. 5.23, the magnets in barrier 1 and 2 are circumferentially segmented into 4 pieces (Barrier 1 is the barrier with the smallest width). In Section 5.12 the magnet losses of another 5 MW PMa-SynRG is investigated and it is shown that the most effective way to decrease the magnet losses is the circumferential segmentation. Therefore, for this machine the same segmentation is used as well.

The air-gap, rotor outer and inner diameter are the same as the IPMSG.

5.7.1 Barrier dimensions

The circumferential thickness of the barriers of this machine is shown in Table 5.21. The parameters are shown in Fig. 5.24. Rib=8 mm. The radial thickness of the barriers and width of barriers are the same as the magnet thickness and magnet width which is given in the next section.

TABLE 5.21: Barrier thickness circumferentially of the PMa-SynRG

	Barrier 1 (mm)	Barrier 2 (mm)	Barrier 3 (mm)	Barrier 4 (mm)	Barrier 5 (mm)
Barrier thickness circumferentially	9	10	10	10	10.8

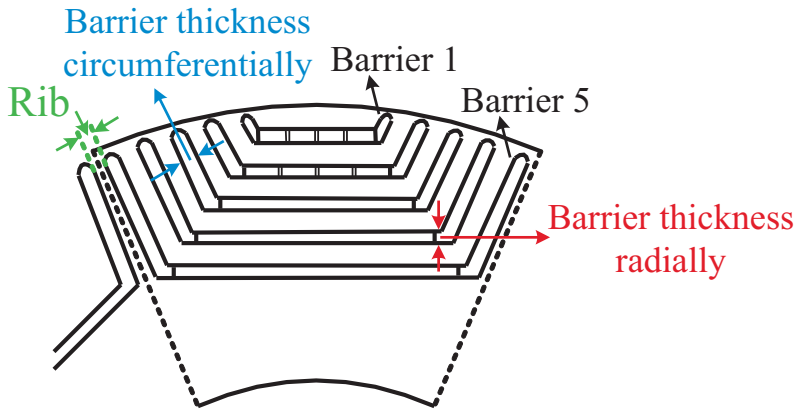

Fig. 5.24 Barrier parameters of the PMa-SynRG.

5.7.2 Magnet dimensions

The magnet dimensions for the PMa-SynRG is given in Table 5.22, Table 5.23 and Table 5.24. The parameters are shown in Fig. 5.25.

TABLE 5.22: Magnet thickness of the PMa-SynRG.

Magnet 1 thickness (mm)	Magnet 2 thickness (mm)	Magnet 3 thickness (mm)	Magnet 4 thickness (mm)	Magnet 5 thickness (mm)
6	6	6	6	5.5

TABLE 5.23: Magnet width of the PMa-SynRG.

Magnet 1 width (mm)	Magnet 2 width (mm)	Magnet 3 width (mm)	Magnet 4 width (mm)	Magnet 5 width (mm)
68	98	123	152	184

TABLE 5.24: Dimension of the segmented magnets of the PMa-SynRG.

Parameter	Value
Space between magnets	0.5 mm
One segment width of magnet 1	16.6 mm
One segment width of magnet 2	24 mm

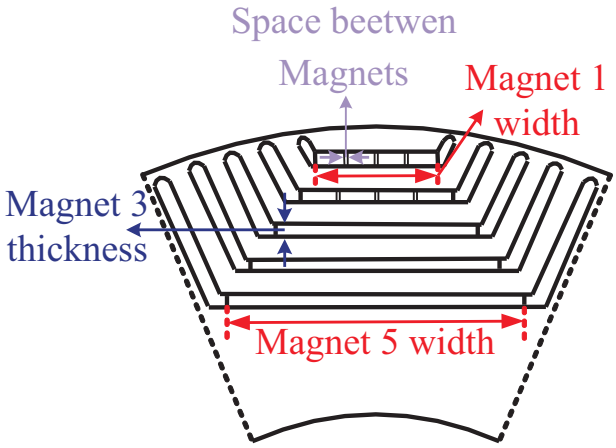

Fig. 5.25 Magnet parameters of the PMa-SynRG.

5.8 Mechanical restriction

5.8.1 No-load investigation

In the same fashion as for the IPMSG, the thickness of the bridges is also important for this machine. As the bridge of the flux barrier closer to the shaft (bridge 5 in Fig. 5.26) is imposed with the highest stress due to that it encloses the largest volume, this bridge thickness is chosen to be the highest. The less volume that the flux barrier encloses the less stress is applied to the bridge. The thickness of these bridges is chosen in order to get a maximum stress of 150 MPa. The values of the different bridge thicknesses are shown in Table 5.25.

TABLE 5.25: Bridge thickness

Parameter	Value
Bridge 1 and 2	3 mm
Bridge 3 and 4	4 mm
Bridge 5	6 mm

The PMa-SynRG is also simulated at no-load and maximum speed (750 rpm) with consideration of gravity force. The strength analysis of the multi-layer IPMSG is shown in Fig. 5.27. As can

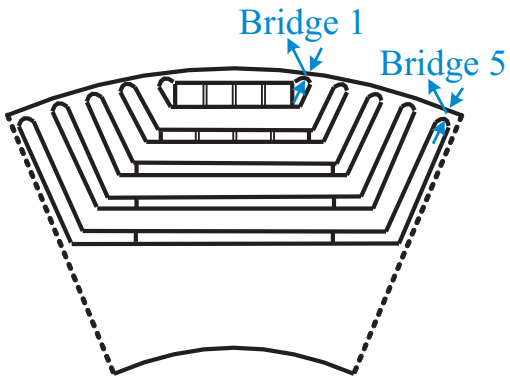

Fig. 5.26 PMa-SynRG bridge thickness.

be seen, the magnets get pushed outwards due to centrifugal forces which may create too much stress for the iron bridges.

5.8.2 Full load investigation

The forces because of the stator current of the PMa-SynRG from Maxwell is exported to Ansys Mechanical. It is found that the stress value is very small compared to the centrifugal force stress (about 2 MPa compared to 140 MPa), which was anticipated in accordance with [44] and [81].

5.9 Torque and torque ripple

The torque waveform of the PMa-SynRG can be obtained using Maxwell. By applying sinusoidal currents

$$\begin{aligned} i_a &= \sqrt{2} I_{rms} \cos\left(2\pi f t + \gamma\right) \\ i_b &= \sqrt{2} I_{rms} \cos\left(2\pi f t + \gamma - 120^\circ\right) \\ i_c &= \sqrt{2} I_{rms} \cos\left(2\pi f t + \gamma - 240^\circ\right) \end{aligned} \tag{5.1}$$

to the stator windings the full load torque is obtained in Maxwell. In (5.1), $I_{rms} = 555\ A$, $\gamma = -149.5^\circ$ and $f = 50\ Hz$.

Figure 5.28 shows the torque waveform as a function of time in one period for the designed PMa-SynRG. The generator torque is not constant and varies with rotor position. The average torque is -64.5 kNm which corresponds to 5.07 MW power which is the same as for the IPMSG. The torque ripple (peak to peak value of torque) is 7.7% of the average rated torque. The torque ripple is reduced almost 50% compared to the IPMSG.

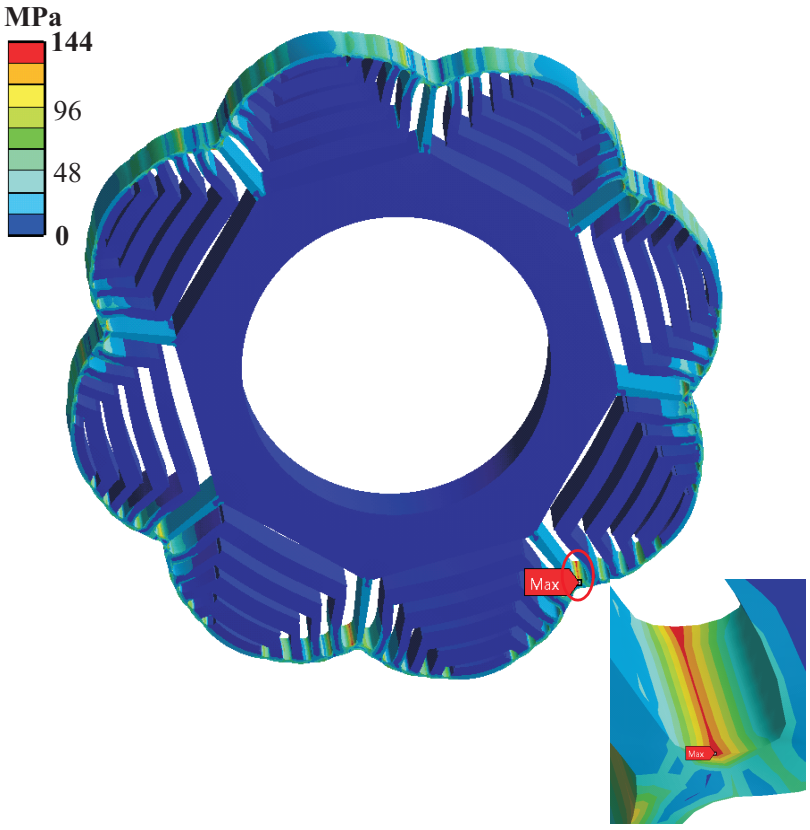

Fig. 5.27 Stress analysis of the PMa-SynRG at no-load and 750 rpm. The deformation of the rotor is exaggerated by a factor of 380 to see the results more clearly.

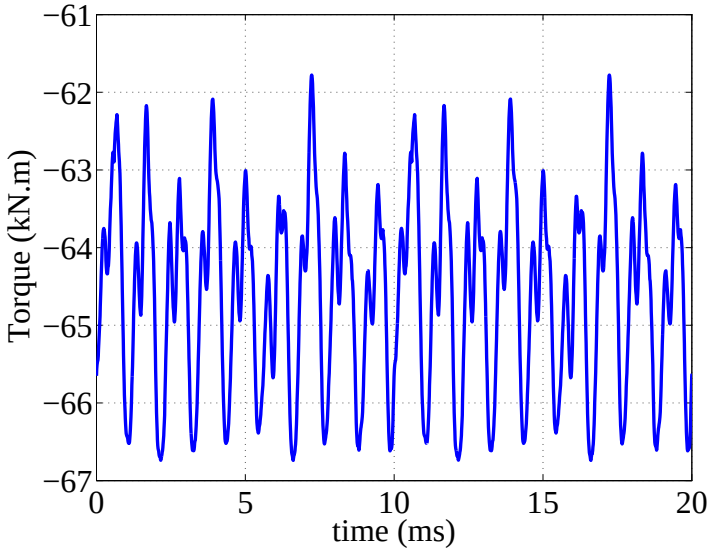

Figure 5.28: Torque waveform for PMa-SynRG during one period.

The 3-phase induced voltages of this IPMSG are shown in Fig. 5.29. As can be seen, the induced voltages are not purely sinusoidal. The fundamental of the peak phase value of the induced voltages at full load are 5.28 kV. The FFT of different harmonics are shown in Fig. 5.30. The Total Harmonic Distortion (THD) of the induced voltage is 10.3%.

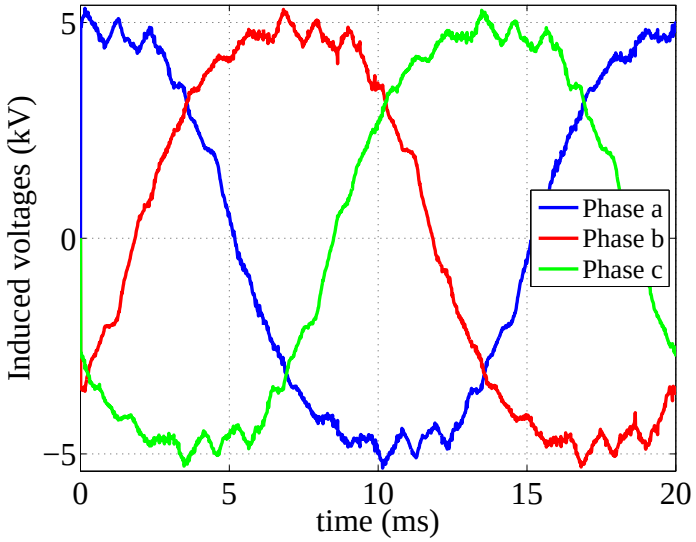

Fig. 5.29 Induced voltage waveforms for PMa-SynRG at full load during one period.

5.10 Active material weight

The active material weight for the PMa-SynRG used in this thesis is given in Table 5.26.

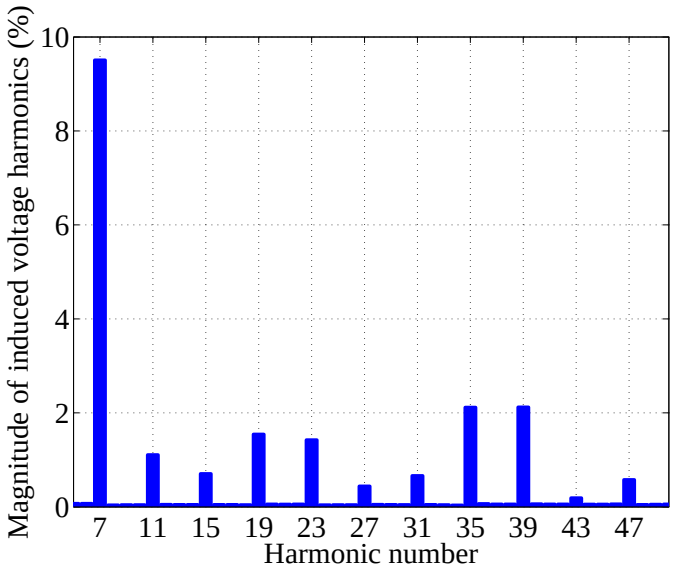

Fig. 5.30 Harmonics amplitude of the induced voltage for the PMa-SynRG in percentage of the fundamental.

TABLE 5.26: Active material weight

Parameter	Value
Stator core steel weight	2397 kg
Rotor core steel weight	1797 kg
Copper weight	1024 kg
Permanent magnet weight	211 kg
Total active material weight	5429 kg

5.11 Demagnetization analysis

A line on the surface of all the 5 layer magnets of the PMa-SynRG is drawn. Similarly as for the IPMSG, if the flux density in the magnets of all the layers is in the reverse direction of the magnet magnetization but less than 0.7 T, the magnets won't be demagnetized.

The flux density on the surface of the magnets at no-load is shown in vector form in Fig. 5.31(a). The normal component of these flux densities is shown in Fig. 5.31(b), starting at the lower corner of the magnets, for the rotor position shown in Fig. 5.31(a).

The full load current (555 A) is applied in the negative d-direction opposite to the direction of magnetization of the magnets. The flux densities along the lines are checked for different rotor positions. Figure 5.32(a) shows the flux densities on the surface of the magnets for one rotor position. As can be seen, the flux densities are in the direction of magnetization. The normal value of the flux densities are shown in Fig. 5.32(b).

Then, twice the full load current is applied in the negative direction. Figure 5.33(a) shows the

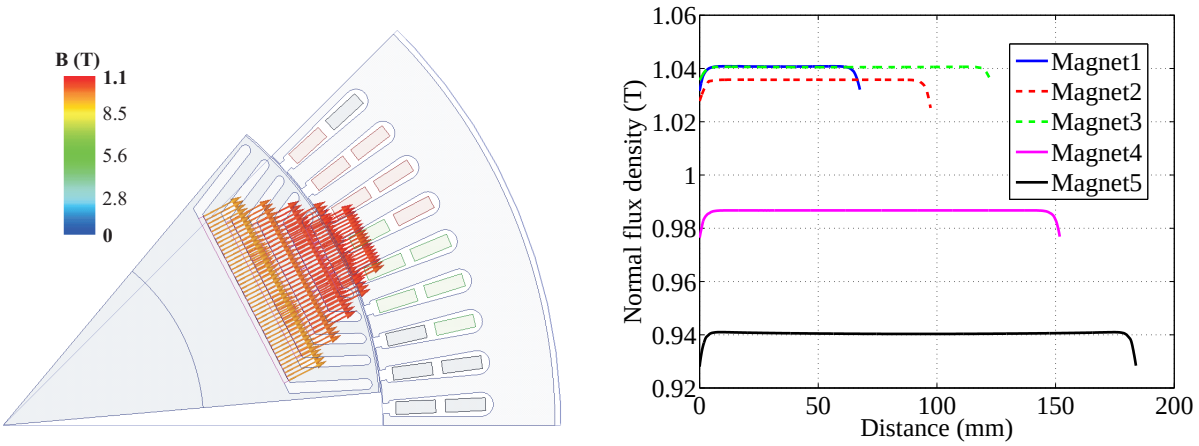

(a) (b)

Fig. 5.31 Magnet flux densities at no-load; (a) Magnitude, (b) Normal values.

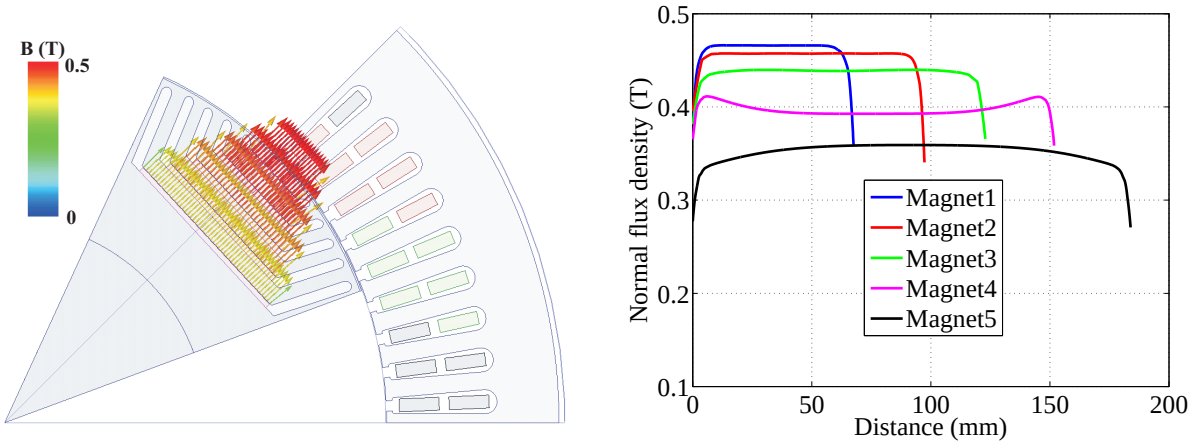

(a) (b)

Fig. 5.32 Magnet flux densities at negative full load current; (a) Magnitude, (b) Normal values.

flux densities on the surface of the magnets for the rotor position with the lowest value of flux densities (magnet 5 has the lowest flux density). As can be seen, for some areas, the flux is in the opposite to the magnetization direction. The normal value of the flux densities are shown in Fig. 5.33(b). since $B_{knee} = -0.7\,T$, there is no risk of demagnetization.

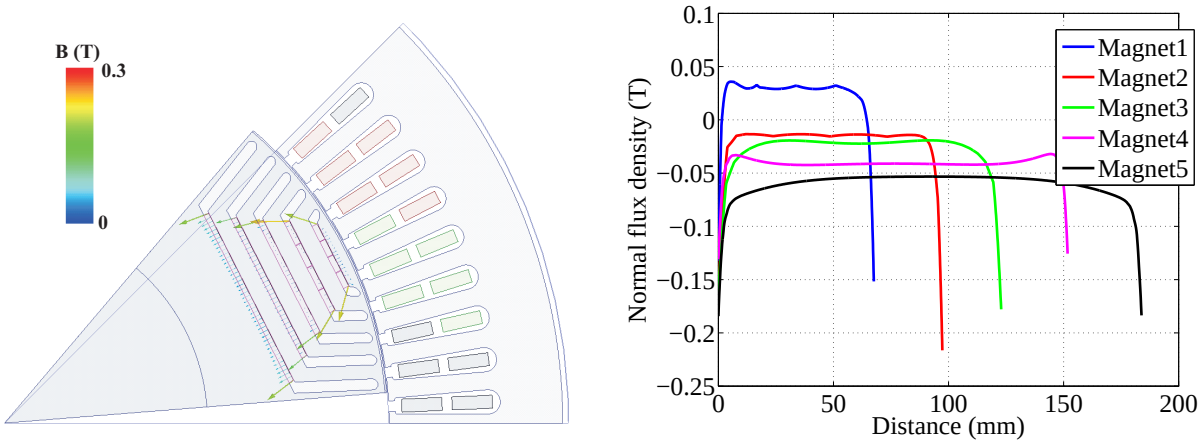

(a) (b)

Fig. 5.33 Magnet flux densities at negative twice full load current; (a) Magnitude, (b) Normal values.

5.12 Magnet loss and segmentation

The magnet losses and effect of segmentation of the magnets on the magnet loss is investigated on a PMa-SynRG from [82]. The results from this section is used for the design of the PMa-SynRG in Section 5.7.

Comparison between a theoretical approach and simulation results

First a 2D model is investigated. The model of the PMa-SynRG with no segments is shown in Fig. 5.34(a). The total loss of the non-segmented magnet machine is shown in Fig. 5.34(b).

Then all the layers of the magnets are divided into 2 pieces circumferentially. Figure 5.35 shows the total loss for the PMa-SynRG with the magnets divided into 2 pieces circumferentially. As can be seen, the loss is concentrated to the top surface of the magnets closest to the air gap and there is also loss on the magnet edges, indicating that there is armature flux entering the magnet in the circumferential direction.

The PMa-SynRG is also modelled in 3D. To save time, half of the machine length (472.5 mm) is modelled. Figure 5.36 shows the model of the PMa-SynRG in 3D.

Figure 5.37 shows the current density in the magnets of the non-segmented PMa-SynRG in 3D. As can be seen, the loss is concentrated to the top surface of the magnets closest to the air gap and there is also loss on the magnet edges. It can also be seen that the loss in the second and third

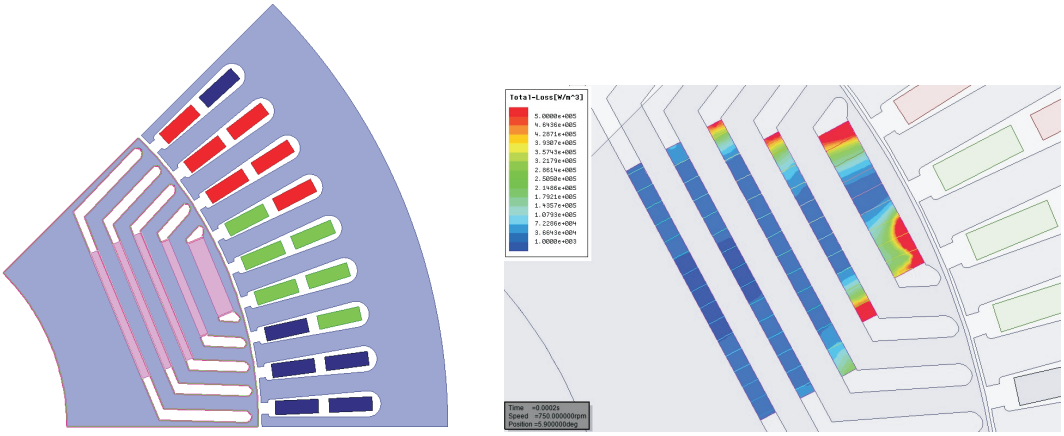

(a) (b)

Fig. 5.34 Non-segmented PMa-SynRG for magnet investigation; (a) Cross-section, (b) Total loss.

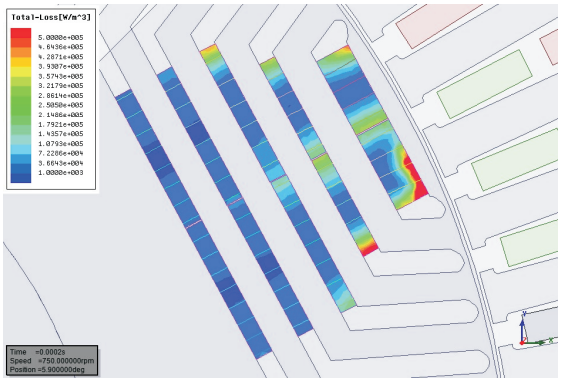

Fig. 5.35 The total loss in the PMa-SynRG magnets with 2 circumferential segments.

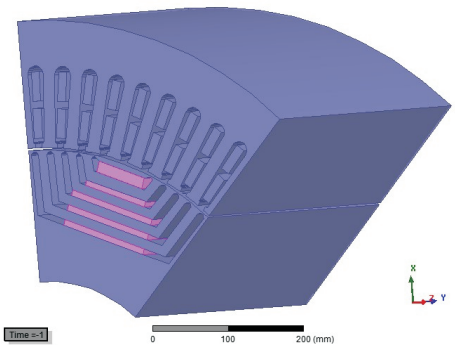

Fig. 5.36 The half-length PMa-SynRM model with no circumferential segments.

magnets of the PMaSynRM is quite large; the loss is not only concentrated to the top magnet even though the upper magnet is closer to the air-gap. This could be because of the larger area of the upper surface of the second and third magnet together with the lower magnet height. The bottom two magnets also have similar shapes but they are further away from the air gap and have thus lower loss.

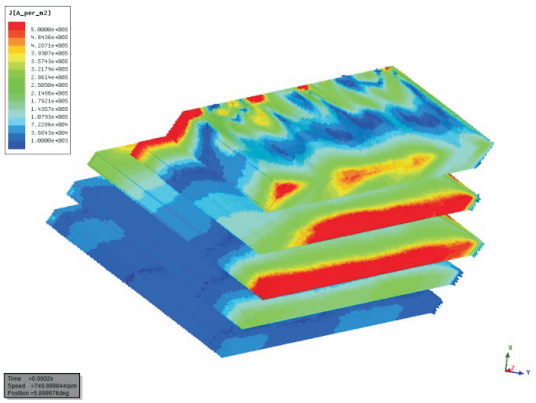

Fig. 5.37 Non-segmented PMa-SynRG in 3D.

The current density in the PMa-SynRM magnets with 2 circumferential segments and no axial segments is shown in Fig. 5.38(a) and with 2 axial segments in Fig. 5.38(b).

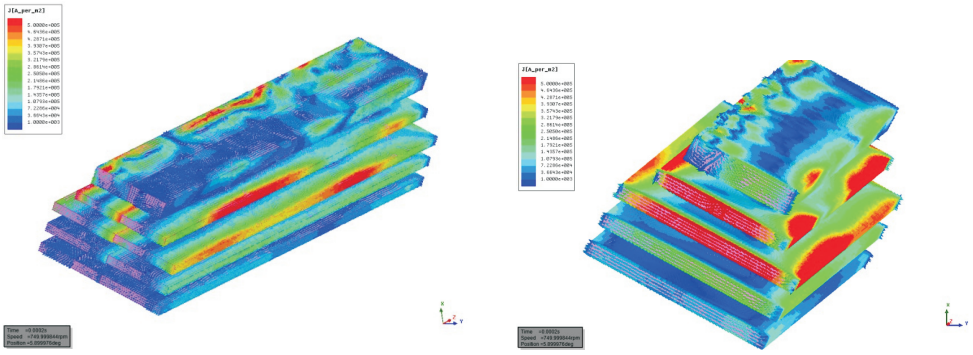

(a) (b)

Fig. 5.38 The current density for the segmented magnet PMa-SynRG; (a) 2 circumferential segments and no axial segments, (b) no circumferential segments and 2 axial segments.

Table 5.27 shows a comparison of the simulated and calculated results with and without axial and circumferential segmentation. As can be realized from Table Table 5.27, the simulations and calculations agree well when it regards the effect of axial segmentation as the ratio of loss without and with 2 axial segments yields for both the simulation and the calculation (using (2.13)) a factor of 1.1. When it comes to circumferential segmentation, the calculations and simulations does not match so well, depending on the shortcomings of the calculations regarding the lack of knowledge of the direction of armature flux. Thus the simulations give a loss ratio (of 1.6) in between the calculated values with mostly radial armature flux (ratio 3.9) and mostly circumferential armature flux (ratio 1.0).

TABLE 5.27: PMa-SynRG segmentation with and without two segments.

	Simulated loss without/with axial segmentation	Calculated loss without/with axial segmentation	Simulated loss without/with circumferential segmentation	Calculated loss without/with circumferential segmentation
PMa-SynRG	1.1	1.1	1.6	1.0 flux in circ. direction 3.9 flux in radial direction

Chapter 6

Energy efficiency and weight assessment

6.1 Machine losses for different wind speed

In this section, copper, iron and magnet losses for the IPMSG and PMa-SynRG are calculated for different wind speeds. Maximum Torque Per Ampere (MTPA) control, respecting the maximum converter voltage, is used for both machines by changing the current angle for the various operating points while the maximum current amplitude is kept the same for the two machines. The operating points are found from the assumed power and rotor speeds at different wind speeds as found in Section 3.1. To calculate the copper losses (2.8) is used. As was mentioned in Section 2.3, the core losses for each wind speed are taken from the FEM program Maxwell and magnet losses are calculated using (2.23) and (2.24) in Maxwell.

Copper, iron and magnet losses for the IPMSG designed in Section 4 and the PMa-SynRG designed in Section 5.7 are illustrated in Fig. 6.1 and Fig. 6.2, respectively. As can be seen, at rated wind speed (12 m/s) and above, the copper losses are the dominant losses for the machines. However, at lower wind speeds (less than 12 m/s), the iron losses are higher. The magnet losses have only a small share of the machine losses.

6.2 Performance comparison of the IPMSG and PMa-SynRG

6.2.1 Losses

The resulting values of some of the operating points of the IPMSG and PMa-SynRG are shown in Table 6.1 and Table 6.2 and the copper losses for different wind speeds are shown in Fig. 6.3. Except at lower wind speeds where the copper loss of the PMa-SynRG is slightly higher, the copper losses are fairly similar for both machines. The reason to the slightly higher copper loss for the PMa-SynRG at lower wind speeds is that the current needs to be higher since the magnet flux is lower (to achieve the same torque). As an example, the current is 31% higher for the wind speed 5 m/s as seen in Table 6.1 and Table 6.2, and the magnet flux, Ψ_m, is 27% lower. Still, the copper loss is very small for both machines at those low current values, so the difference

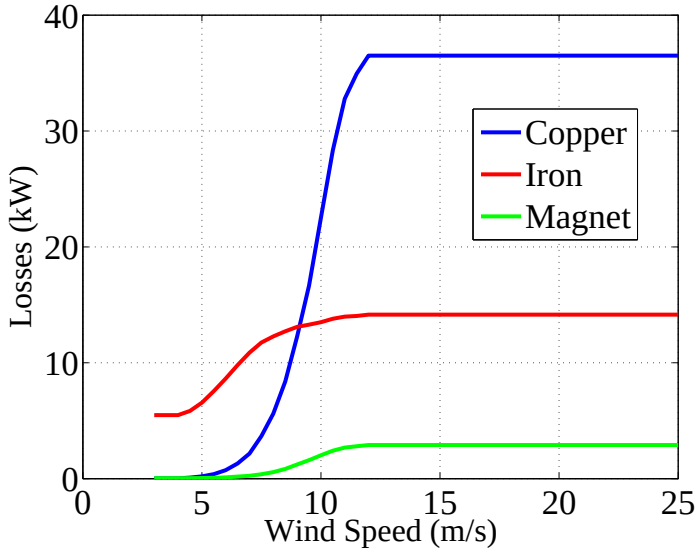

Fig. 6.1 Copper, iron and magnet losses for the IPMSG.

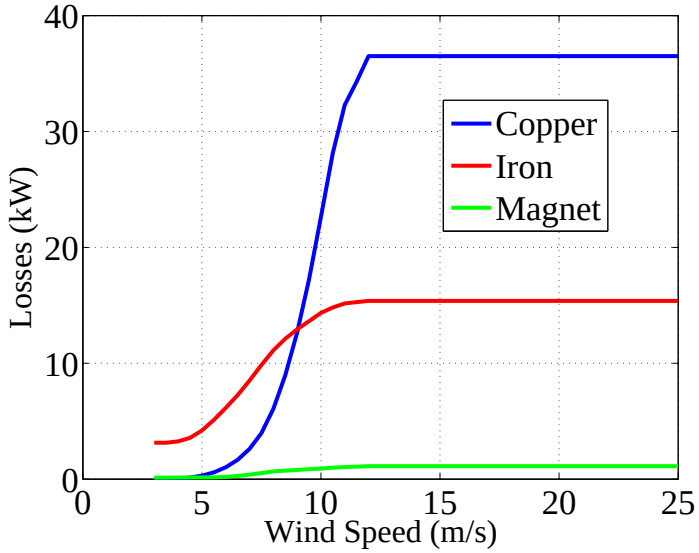

Fig. 6.2 Copper, iron and magnet losses for the PMa-SynRG.

between the machines is nearly not visible. For the higher wind speeds, the current values are fairly similar and at full load (12 m/s), identical.

TABLE 6.1: Operating points for the IPMSG

Wind speed (m/s)	Generator speed (rpm)	average torque (kNm)	Ψ_m (Wb)	Current (A)	Current angle (deg)	Power factor	P_{fe} (kW)	L_d (mH)	L_q (mH)
4	443	1.7	13.5	12.5	-93	1	5.5	18	54
5	485	4.7	13.5	38.6	-99.5	1	6.5	12.9	53.7
6	576	9.5	13.4	78.2	-107	0.99	8.5	13.1	53.2
8	736	26.2	13	213.4	-116.5	0.97	12.1	12.2	35.8
9	750	39	12.6	319.8	-119.5	0.94	12.7	11.9	29.3
10	750	52	12.2	435.3	-122.5	0.9	13.3	11.7	25.5
12-25	750	64.5	11.7	555	-125	0.86	14.2	11.6	22.9

TABLE 6.2: Operating points for the PMa-SynRG

Wind speed (m/s)	Generator speed (rpm)	average torque (kNm)	Ψ_m (Wb)	Current (A)	Current angle (deg)	Power factor	P_{fe} (kW)	L_d (mH)	L_q (mH)
4	443	1.7	10	20	-101	1	3.3	18.4	91.7
5	485	4.7	9.9	50.8	-112.5	0.99	4.2	18.1	87.9
6	576	9.5	9.7	92.8	-121.5	0.97	6.1	17	80
8	736	26.2	9	226	-137	0.93	11.1	16	62.6
9	750	39	8.6	327	-142.5	0.9	13	15.2	54.2
10	750	52	8.3	437	-146.5	0.86	14.3	14.5	47.7
12-25	750	64.5	8	555	-149.5	0.82	15.4	13.9	42

The iron losses of the IPMSG and PMa-SynRG are compared in Fig. 6.4. As can be seen, the iron loss for the PMa-SynRG at higher wind speeds (higher than 9 m/s) is higher. However, at lower wind speeds the value is lower. This is probably because of the lower flux for lower rotational for the PMa-SynRG, as indicated by the lower magnet flux values seen in Table 6.1 and Table 6.2 for low wind speeds (i.e. 5 m/s), together with the low current values (and thus a low contribution of armature flux). To investigate this, the average flux density in the air-gap for different wind speeds for both machines is investigated.

The average flux density in the air-gap for the machines at a wind speed 5 m/s is shown in Fig. 6.5. As can be seen, the average flux density for the IPMSG is, as expected, higher than for the PMa-SynRG (around 30% difference). Therefore, this machine has higher iron loss at the wind speed of 5 m/s.

Figure 6.6 shows the average flux density in the air-gap at full load for the machines. As can be seen, the average flux density at full load for the IPMSG is now lower than that of the PMa-SynRG (around 8% difference). Hence, this machine has lower iron loss at full load.

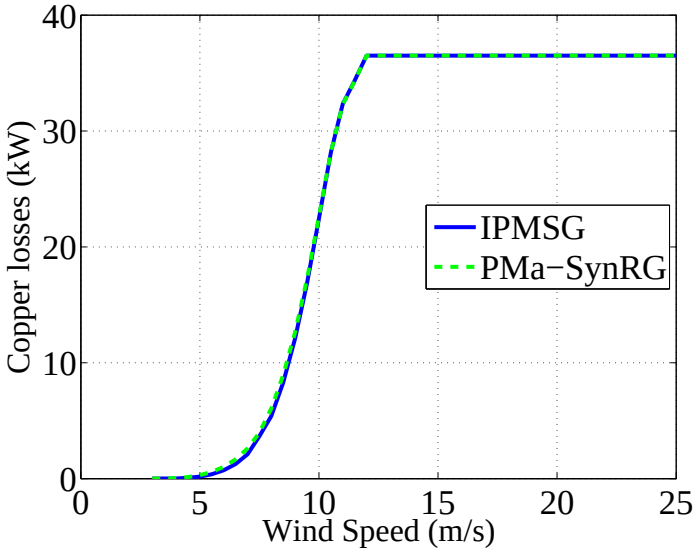

Fig. 6.3 Copper losses for the IPMSG and PMa-SynRG.

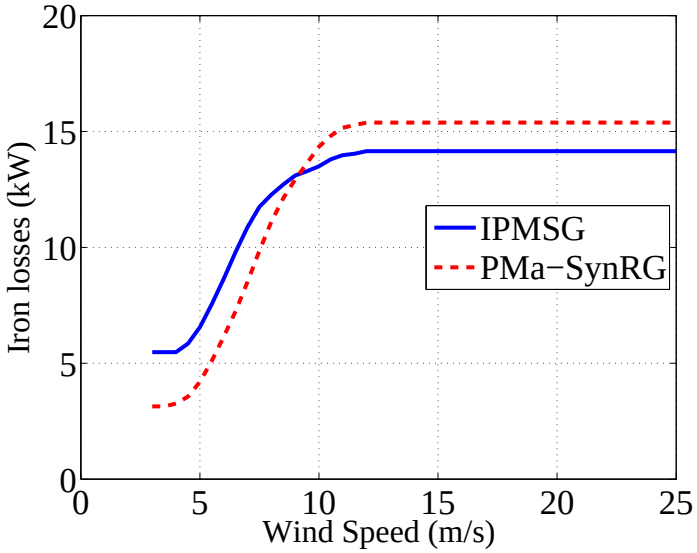

Fig. 6.4 Iron losses for the IPMSG and PMa-SynRG.

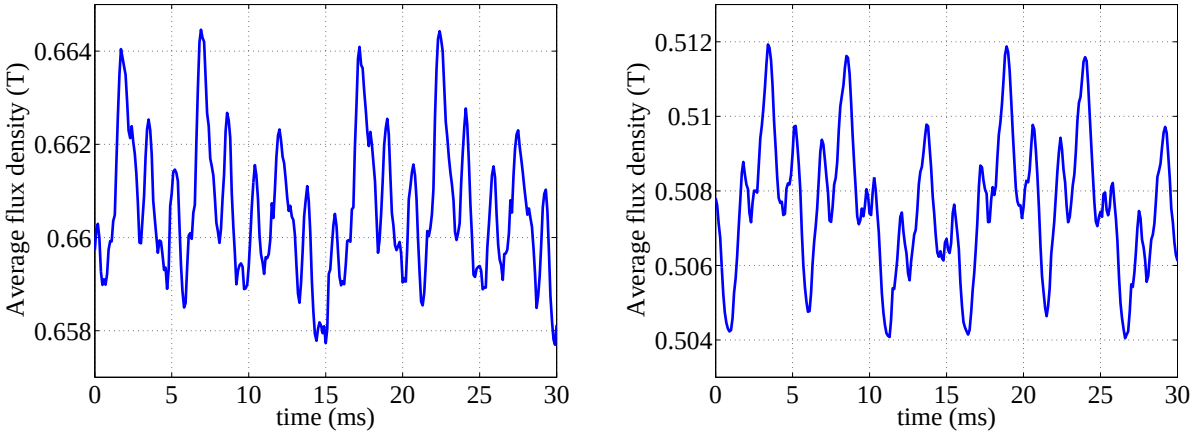

Fig. 6.5 Average flux density at wind speed 5 m/s; (a) IPMSG, (b) PMa-SynRG.

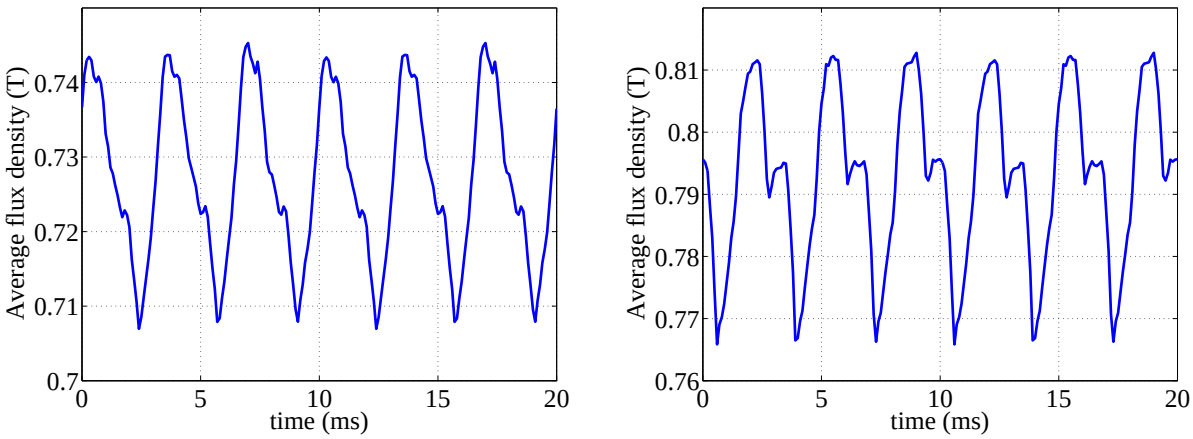

Fig. 6.6 Average flux density at full load; (a) IPMSG, (b) PMa-SynRG.

The flux lines for the IPMSG and the PMa-SynRG at no-load and full load are shown are shown in Fig. 6.7 and Fig. 6.8.

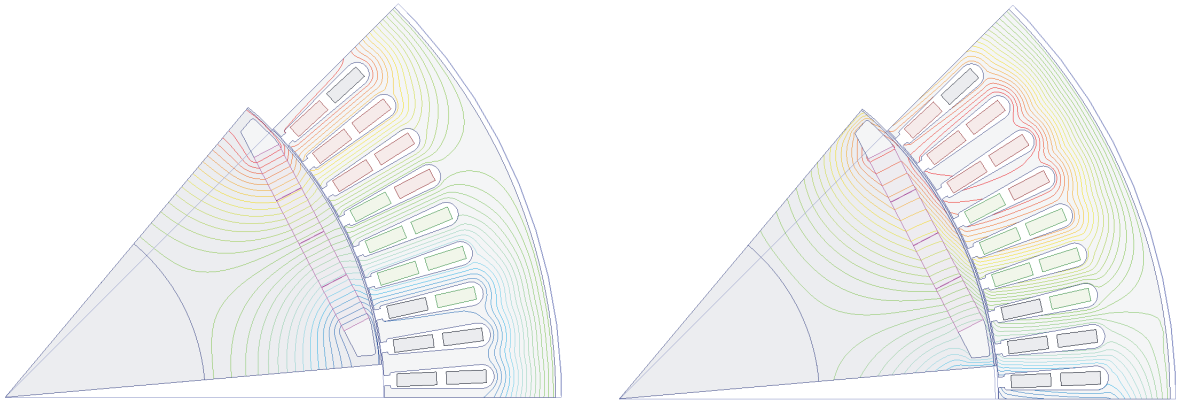

(a) (b)

Fig. 6.7 Flux lines in the IPMSG; (a) No-load, (b) Full load.

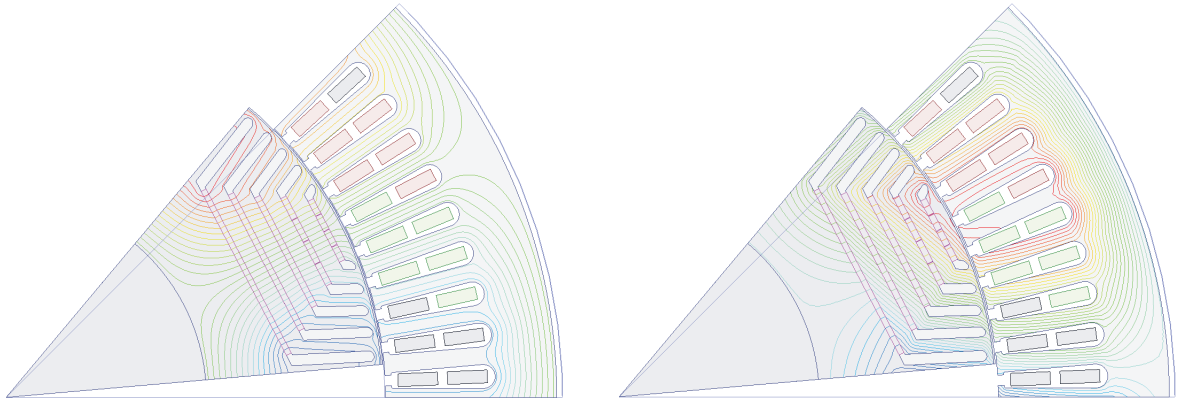

(a) (b)

Fig. 6.8 Flux lines in the PMa-SynRG; (a) No-load, (b) Full load.

Figure 6.9 shows the magnet losses of the IPMSG and PMa-SynRG. As can be seen, the magnet losses for the PMa-SynRG at wind speeds higher than 9 m/s is lower compared to those for the IPMSG. However, at lower wind speeds the magnet losses for the PMa-SynRG is slightly higher. The much lower magnet loss of the PMa-SynRM makes sense since the magnet weight is lower (as shown in Section 6.3), giving that the stator currents are fairly equal, as they are for higher wind speeds (above 9 m/s). At lower wind speeds (below 9 m/s), low power output and lower generator speed, the stator currents are small and the magnet loss is low. However, as mentioned before, there is a difference in current values where the PMa-SynRG has around 31% higher currents for the wind speed of 5 m/s, and therefore, could have slightly higher magnet loss.

The sum of copper, iron and magnet losses of the machines are compared in Fig. 6.10. The

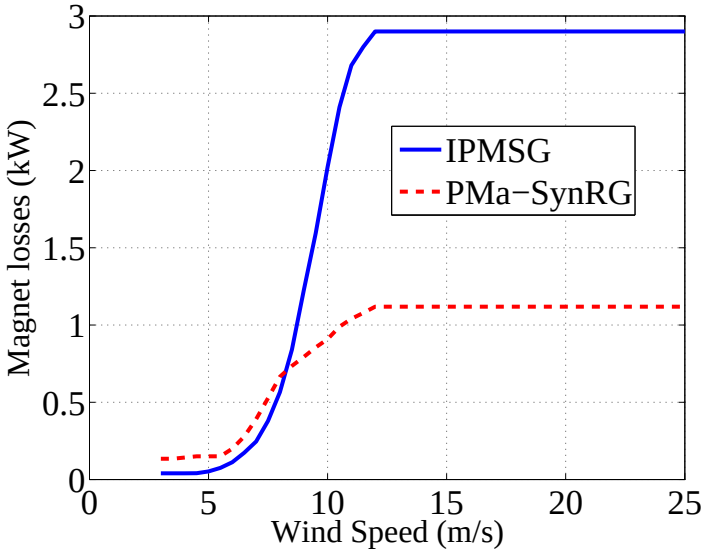

Fig. 6.9 Magnet losses for the IPMSG and PMa-SynRG.

total losses for the PMa-SynRG is lower than for the IPMSG. This is because as was shown in Fig. 6.4, the iron losses of the PMa-SynRG at lower wind speeds are lower.

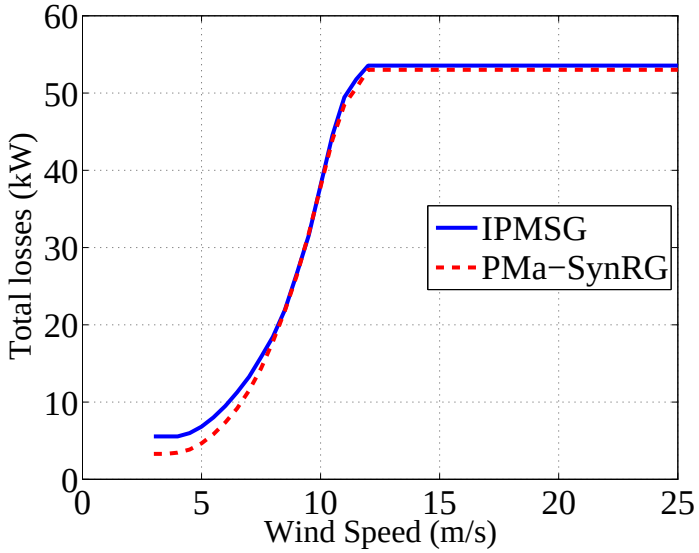

Fig. 6.10 Total losses for the IPMSG and PMa-SynRG.

6.2.2 Power factor

Figure 6.11 shows the power factor comparison of the IPMSG and PMa-SynRG. The power factor of the PMa-SynRG is lower for all the average wind speeds. However, if high power factor is an issue, the design of the PMa-SynRG can be changed to have the same power factor

as the IPMSG by increasing the amount of magnet material, as in the design of the PMa-SynRG in [82].

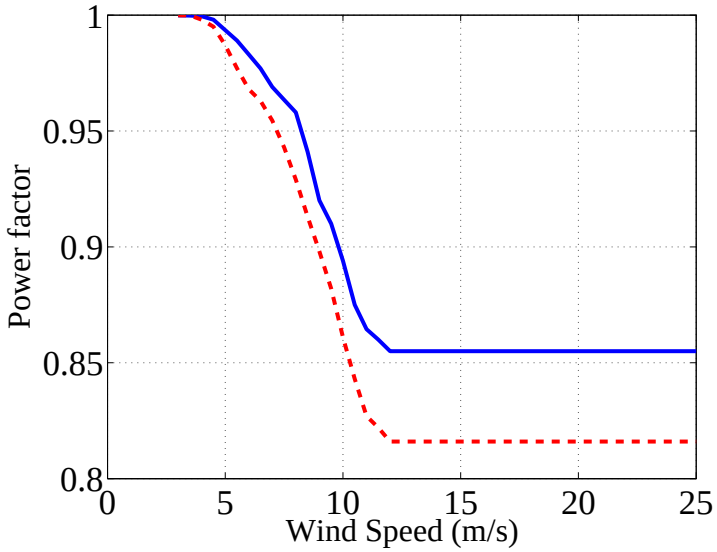

Fig. 6.11 Power factor for the IPMSG and PMa-SynRG.

6.2.3 Annual energy efficiency

The total amount of energy that a wind turbine produces is very important, since it gives the total income. Therefore, the energy collected from the wind over a period of time needs to be calculated. If this energy is calculated for a period of one year, it is called annual energy capture. For this purpose, the power and the probability density ($f(\omega)$) can be used. The amount of energy a wind turbine produces at a given average wind speed is

$$E_{\bar{\omega}} = T \int P(\omega) f(\omega) \, d\omega \tag{6.1}$$

where T is the number of hours per year and $f(\omega)$ can be found in [27]. If we need to calculate the annual energy losses (E_{loss}), then $P(\omega)$ will be the losses as a function of the wind speed. The losses can be any kind of loss, such as generator losses, converter losses, gearbox losses or the total losses. Depending on what we are looking for, the type of loss can be selected. In this work $P(\omega)$ is the sum of copper, iron and magnet losses of the machine. To calculate the mechanical annual energy (E_{mec}), the mechanical power of the turbine is used as $P(\omega)$ in (6.1).

The annual energy efficiency of a wind turbine for a specific average wind speed, E in percentage, can then be calculated using

$$E = \left(1 - \frac{E_{loss}}{E_{mec}}\right) 100 \tag{6.2}$$

As mentioned, E is the annual energy efficiency for a specific average wind speed.

The machine annual energy efficiency of the IPMSG and PMa-SynRG is illustrated in Fig. 6.12. As can be seen, the PMa-SynRG has higher machine annual energy efficiency at all average wind speeds. The reason for this is the lower flux level at low wind speeds in the PMa-SynRG which creates lower iron losses.

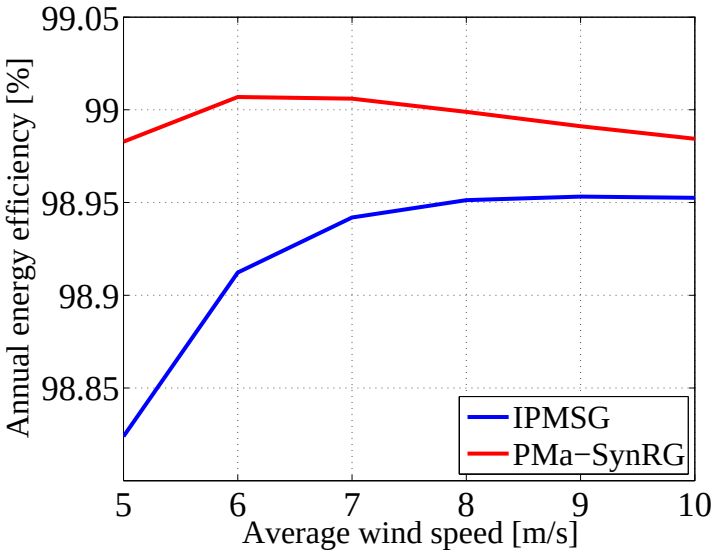

Fig. 6.12 Machine annual energy efficiency for the IPMSG and PMa-SynRG.

6.3 Weight comparison

The active material weight for the IPMSG and PMa-SynRG is given in Table 6.3.

TABLE 6.3: Active material weight

Parameter	IPMSG	PMa-SynRG
Stator core steel weight	2397 kg	2397 kg
Rotor core steel weight	1815 kg	1797 kg
Copper weight	1024 kg	1024 kg
Permanent magnet weight	310 kg	211 kg
Total active material weight	5546 kg	5429 kg

As can be seen, the PMa-SynRG not only has a slightly lighter rotor but also has less magnet weight. It should be mentioned that the rotor weight in both machines can be decreased by removing some parts of the rotor core.

Chapter 7

Conclusions and future work

7.1 Conclusions

In this work, design and analysis of a 5 MW wind energy generator is performed to find an energy-efficient generating system for offshore wind turbines, studying permanent magnet generators as well as a synchronous reluctance generator and a combination in between them. Quantities such as torque density, torque ripple, losses and amount of magnet material are studied. The work was performed in two stages, for the first part, results are given in [27], as well as in paper VII-IX (as listed in Section 1.3), while the second half of this work is presented in the present report. To sum up, the following main conclusions are found. First, the results from the first half:

If a medium voltage generator and an active rectifier with IGBTs are used in the system, from the loss point of view it is best to use a low voltage rating IGBT module (1.7 kV) for the converter, even though more modules are needed to be used in series to achieve the required voltage. The reason that makes the 1.7 kV module beneficial compared to higher voltage modules (3.3 kV and 6.5 kV) is that although the converter composed with low voltage modules has the highest conduction losses, it has substantially lower switching losses.

A SPMSG and an IPMSG with the same amount of material are considered. The results show that the power factor of the IPMSG is higher at the rated wind speed compared to the SPMSG. Moreover, the annual energy efficiency of the system comprising the IPMSG is higher.

An IPMSG is compared with a synchronous reluctance generator (SynRG) using the same geometrical dimensions for both generators. It was found that a SynRG can convert 74% of the power that an IPMSG can convert, while it has 80% of the IPMSG weight. The power factor of the IPMSG is higher for all the operating points.

Two methods to reduce the torque ripple of the IPMSG were studied. The first method is skewing the stator and the other method is a fractional slot interior permanent magnet generator (IPMSGFS). The results show that both methods reduce the torque ripple by about 70%, while the torque drop is negligible.

According to the investigations done in this work it is indicated that the most suitable system

includes an IPMSG with a dc-link voltage between the voltage level that gives maximum torque per ampere operation for the whole operation region and the minimum dc-link voltage level which gives the required rated torque.

In the second part of the project, the following conclusions are found.

It is found that the proposed PMa-SynRG has a better torque density compared to the IPMSG using the same size. In addition the torque ripple is lower, due to the freedom, although limited, to adjust the positions of the barriers in the rotor. It is also shown how the torque production and torque ripple are varying as the number of barriers varies.

An effort is made to instead of reaching the maximum torque, to reduce the magnet content and compare the generators at the same power level. Since the torque production to a high extent comes from the reluctance difference in d- and q-direction, it is found that the derived PMa-SynRG can contain 30% less magnet weight compared to the IPMSG for the same maximum power level.

It is further found that during the assessments of the generator rotors, the mechanical strength of the iron bridges above the barriers must be continuously checked, in order to make them thin and thereby giving a good performance, but also thick enough from a mechanical strength point of view.

Furthermore, the impact of magnet segmentation and the loss reduction potential is shown for different segmentation directions. It is also shown that the generators can withstand at least 2 times the rated current in the d-direction without being demagnetized.

Finally, by determining the annual average power produced by the two machine types during different average wind conditions, it is found that the machine annual energy efficiency for the PMa-SynRG is higher for all average wind speeds. The key reason for this is the lower flux level in the PMa-SynRG which creates lower iron losses at low wind speeds.

7.2 Future work

The speed of the generators that are investigated in this work is 750 rpm. Therefore the wind turbines using these generators need to be equipped with a gearbox. A valuable further effort is to include gearbox losses and weight and put these in relation to those using a generating system with a low speed generator (direct drive).

The number of poles in a generator is an important issue for the performance of the generating system, which can be investigated.

Thermal calculation of the generators is an important task. This could be used to verify the temperature considered during the demagnetization calculations.

As the rotor bridge thickness is an important parameter in PMa-SynRMs, it would be interesting to consider an outer rotor generator. The barrier thickness can be decreased in outer rotor machines due to less centrifugal force applied.

A 3-level converter, or even higher number of levels, can be included in the system and the

results can be compared to the case with a 2-level converter.

Finally, to build a small scale experimental system, in order to verify simulations and investigate practical details, would be of great value.

References

[1] A. Abedini and A. Nasiri, "Applications of super capacitors for PMSG wind turbine power smoothing," in *Industrial Electronics, 2008. IECON 2008. 34th Annual Conference of IEEE*, Nov 2008, pp. 3347–3351.

[2] K. Yoshimoto, T. Nanahara, and G. Koshimizu, "New control method for regulating state-of-charge of a battery in hybrid wind power/battery energy storage system," in *Power Systems Conference and Exposition, 2006. PSCE '06. 2006 IEEE PES*, Oct 2006, pp. 1244–1251.

[3] S. Musunuri and H. Ginn, "Comprehensive review of wind energy maximum power extraction algorithms," in *Power and Energy Society General Meeting, 2011 IEEE*, July 2011, pp. 1–8.

[4] S. Teleke, M. Baran, A. Huang, S. Bhattacharya, and L. Anderson, "Control strategies for battery energy storage for wind farm dispatching," *Energy Conversion, IEEE Transactions on*, vol. 24, no. 3, pp. 725–732, Sept 2009.

[5] M. Chowdhury, M. Haque, M. Aktarujjaman, M. Negnevitsky, and A. Gargoom, "Grid integration impacts and energy storage systems for wind energy applications - a review," in *Power and Energy Society General Meeting, 2011 IEEE*, July 2011, pp. 1–8.

[6] G. Wilson, D. McMillan, and G. Ault, "Modelling the effects of the environment on wind turbine failure modes using neural networks," in *Sustainable Power Generation and Supply (SUPERGEN 2012), International Conference on*, Sept 2012, pp. 1–6.

[7] R. Li, S. Bozhko, G. Asher, J. Clare, L. Yao, and C. Sasse, "Grid frequency control design for offshore wind farms with naturally commutated HVDC link connection," in *Industrial Electronics, 2006 IEEE International Symposium on*, vol. 2, july 2006, pp. 1595 –1600.

[8] N. Kirby, L. Xu, M. Luckett, and W. Siepmann, "HVDC transmission for large offshore wind farms," *Power Engineering Journal*, vol. 16, no. 3, pp. 135 –141, june 2002.

[9] T. Ackermann, "Transmission systems for offshore wind farms," *Power Engineering Review, IEEE*, vol. 22, no. 12, pp. 23 –27, dec. 2002.

[10] E. Lepa, T. Thurnherr, and A. Faulstich, "Design and testing of a 7 MW wind turbine medium voltage electrical drivetrain with medium speed permanent magnet synchronous generator," in EWEA *2013 Europe's premier wind energy event*, 2013, pp. 1–8.

[11] M. Alatalo, S. Lundmark, and E. Arfa Grunditz, "Electric machine design for traction applications considering recycling aspects-review and new solution," in *IECON 2011 - 37th Annual Conference on IEEE Industrial Electronics Society*, Nov 2011, pp. 1836–1841.

[12] B. Sprecher, Y. Xiao, A. Walton, J. Speight, R. Harris, R. Kleijn, G. Visser, and G. J. Kramer, "Life cycle inventory of the production of rare earths and the subsequent production of NdFeB rare earth permanent magnets," *Environmental Science & Technology*, vol. 48, no. 7, pp. 3951–3958, 2014.

[13] S. Tokunaga and K. Kesamaru, "FEM simulation of novel small wind turbine generation system with synchronous reluctance generator," in *Electrical Machines and Systems (ICEMS), 2011 International Conference on*, 2011, pp. 1–6.

[14] R. Moghaddam, "Synchronous reluctance machine (SynRM) in variable speed drives (VSD) applications," Ph.D Thesis, Royal Institute of Technology, School of Electrical Engineering, Stockholm, Sweden, May 2011.

[15] F. Libert and J. Soulard, "Design study of different direct-driven permanent-magnet motors for a low speed application," in *Proceedings of the Nordic Workshop on Power and Industrial Electronics (NORpie),* Trondheim, Norway, June 2004.

[16] H. Chen, R. Qu, J. Li, and B. Zhao, "Comparison of interior and surface permanent magnet machines with fractional slot concentrated windings for direct-drive wind generators," in *Electrical Machines and Systems (ICEMS), 2014 17th International Conference on*, Oct 2014, pp. 2612–2617.

[17] K. Klontz, T. Miller, M. McGilp, H. Karmaker, and P. Zhong, "Short-circuit analysis of permanent-magnet generators," *Industry Applications, IEEE Transactions on*, vol. 47, no. 4, pp. 1670–1680, July 2011.

[18] P. Reddy, A. El-Refaie, K.-K. Huh, J. Tangudu, and T. Jahns, "Comparison of interior and surface PM machines equipped with fractional-slot concentrated windings for hybrid traction applications," in *Energy Conversion Congress and Exposition (ECCE), 2011 IEEE*, 2011, pp. 2252–2259.

[19] J.-B. Park, M. Johnson, and H. Toliyat, "Interior PMSM double layer rotor core parametric design study," in *Industrial Electronics Society, IECON 2014 - 40th Annual Conference of the IEEE*, Oct 2014, pp. 695–701.

[20] L. Fang, J.-W. Jung, J.-P. Hong, and J.-H. Lee, "Study on high-efficiency performance in interior permanent-magnet synchronous motor with double-layer PM design," *Magnetics, IEEE Transactions on*, vol. 44, no. 11, pp. 4393–4396, Nov 2008.

[21] L. Fang and J.-P. Hong, "Flux-barrier design technique for improving torque performance of interior permanent magnet synchronous motor for driving compressor in HEV," in *Vehicle Power and Propulsion Conference, 2009. VPPC '09. IEEE*, Sept 2009, pp. 1486–1490.

[22] R. Vartanian, Y. Deshpande, and H. Toliyat, "Performance analysis of a rare-earth magnet based NEMA frame permanent magnet assisted synchronous reluctance machine with different magnet type and quantity," in *Electric Machines Drives Conference (IEMDC), 2013 IEEE International*, May 2013, pp. 476–483.

[23] J. H. Lee, J. C. Kim, and D.-S. Hyun, "Effect analysis of magnet on Ld and Lq inductance of permanent magnet assisted synchronous reluctance motor using finite element method," *Magnetics, IEEE Transactions on*, vol. 35, no. 3, pp. 1199–1202, May 1999.

[24] P. Guglielmi, M. Pastorelli, G. Pellegrino, and A. Vagati, "Position-sensorless control of permanent-magnet-assisted synchronous reluctance motor," *Industry Applications, IEEE Transactions on*, vol. 40, no. 2, pp. 615–622, March 2004.

[25] K. Khan, M. Leksell, and O. Wallmark, "Design aspects on magnet placement in permanent-magnet assisted synchronous reluctance machines," in *Power Electronics, Machines and Drives (PEMD 2010), 5th IET International Conference on*, April 2010, pp. 1–5.

[26] S. Sibande, M. Kamper, R. Wang, and E. Rakgati, "Optimal design of a pm-assisted rotor of a 110 kw reluctance synchronous machine," in *AFRICON, 2004. 7th AFRICON Conference in Africa*, vol. 2, Sept 2004, pp. 793–797 Vol.2.

[27] P. Roshanfekr, "Energy-efficient generating system for HVDC off-shore wind turbine," Licentiate Thesis, Chalmers University of Technology, Department of Electric Power Enginering, Göteborg, Sweden, October 2013.

[28] J. F. Gieras and M. Wing, *Permanent Magnet Motor Technology*. Marcel Dekker, Inc., 2002.

[29] S. Keshavarz, "Design and evaluation of an active rectifier for a 4.1 MW off-shore wind turbine," Master's thesis, 2011, 42.

[30] A. EL-Refaie, "Fractional-slot concentrated-windings synchronous permanent magnet machines: Opportunities and challenges," *Industrial Electronics, IEEE Transactions on*, vol. 57, no. 1, pp. 107–121, 2010.

[31] F. Tahami, H. Nademi, and M. Rezaei, "Maximum torque per ampere control of permanent magnet synchronous motor using genetic algorithm," *TELKOMNIKA (Telecommunication, Computing, Electronics and Control)*, vol. 9, no. 2, 2013. [Online]. Available: http://journal.uad.ac.id/index.php/TELKOMNIKA/article/view/1311

[32] T. Jahns, G. Kliman, and T. W. Neumann, "Interior permanent-magnet synchronous motors for adjustable-speed drives," *Industry Applications, IEEE Transactions on*, vol. IA-22, no. 4, pp. 738–747, 1986.

[33] E. Rashad, T. Radwan, and M. Rahman, "A maximum torque per ampere vector control strategy for synchronous reluctance motors considering saturation and iron losses," in *Industry Applications Conference, 2004. 39th IAS Annual Meeting. Conference Record of the 2004 IEEE*, vol. 4, 2004, pp. 2411–2417 vol.4.

[34] J. Hendershot and T. Miller, *Design of Brushless Permanent-Magnet Machines*. Florida, USA: Motor Design Books LLC, 2010.

[35] P. Niazi, H. Toliyat, D.-H. Cheong, and J.-C. Kim, "A low-cost and efficient permanent-magnet-assisted synchronous reluctance motor drive," *Industry Applications, IEEE Transactions on*, vol. 43, no. 2, pp. 542–550, March 2007.

[36] S. Morimoto, M. Sanada, and Y. Takeda, "Performance of PM-assisted synchronous reluctance motor for high-efficiency and wide constant-power operation," *Industry Applications, IEEE Transactions on*, vol. 37, no. 5, pp. 1234–1240, Sep 2001.

[37] P. Niazi, H. Toliyat, and A. Goodarzi, "Robust maximum torque per ampere (MTPA) control of PM-assisted SynRM for traction applications," *Vehicular Technology, IEEE Transactions on*, vol. 56, no. 4, pp. 1538–1545, July 2007.

[38] J. H. Lee, J. C. Kim, and D.-S. Hyun, "Effect analysis of magnet on Ld and Lq inductance of permanent magnet assisted synchronous reluctance motor using finite element method," *Magnetics, IEEE Transactions on*, vol. 35, no. 3, pp. 1199–1202, May 1999.

[39] R. Vartanian, H. Toliyat, B. Akin, and R. Poley, "Power factor improvement of synchronous reluctance motors (SynRM) using permanent magnets for drive size reduction," in *Applied Power Electronics Conference and Exposition (APEC), 2012 Twenty-Seventh Annual IEEE*, Feb 2012, pp. 628–633.

[40] A. Ortega Dulanto, "Design of a synchronous reluctance motor assisted with permanent magnets for pump applications," Master's thesis, 2015.

[41] K. Khan, S. Haghbin, M. Leksell, and O. Wallmark, "Design and performance analysis of a permanent-magnet assisted synchronous reluctance machine for an integrated charger application," in *Electrical Machines (ICEM), 2010 XIX International Conference on*, Sept 2010, pp. 1–6.

[42] Y. Deshpande and H. Toliyat, "Design of an outer rotor ferrite assisted synchronous reluctance machine (Fa-SynRM) for electric two wheeler application," in *Energy Conversion Congress and Exposition (ECCE), 2014 IEEE*, Sept 2014, pp. 3147–3154.

[43] J.-W. Jung, B.-H. Lee, D.-J. Kim, J.-P. Hong, J.-Y. Kim, S.-M. Jeon, and D.-H. Song, "Mechanical stress reduction of rotor core of interior permanent magnet synchronous motor," *Magnetics, IEEE Transactions on*, vol. 48, no. 2, pp. 911–914, Feb 2012.

[44] P. Lindh, J. Pyrhonen, M. Polikarpova, V. Kurvinen, J. Heikkinen, and V. Naumanen, "Electrical and mechanical design of a pm traction motor with tooth coils," in *Power Electronics and Applications (EPE), 2013 15th European Conference on*, Sept 2013, pp. 1–8.

[45] K.-H. Ha, J.-P. Hong, G.-T. Kim, Y.-H. Choi, and W.-J. Chung, "Mechanical vibration and stress analysis of the link of interior permanent magnet type synchronous motor," in *Electric Machines and Drives, 1999. International Conference IEMD '99*, May 1999, pp. 150–152.

[46] Z. Han, H. Yang, and Y. Chen, "Investigation of the rotor mechanical stresses of various interior permanent magnet motors," in *Electrical Machines and Systems, 2009. ICEMS 2009. International Conference on*, Nov 2009, pp. 1–6.

[47] S. T. Lundmark, *Course Compendium Part II for the course* LUP *625 Electric Drives*. Göteborg, Sweden, Chalmers University of Technology, Department of Energy and Environment, 2011.

[48] D. Lin, P. Zhou, W. N. Fu, Z. Badics, and Z. Cendes, "A dynamic core loss model for soft ferromagnetic and power ferrite materials in transient finite element analysis," *Magnetics, IEEE Transactions on*, vol. 40, no. 2, pp. 1318–1321, 2004.

[49] Y. Liu, S. Kashif, and A. Sohail, "Engineering considerations on additional iron losses due to rotational fields and sheet cutting," in *Electrical Machines, 2008. ICEM 2008. 18th International Conference on*, Sept 2008, pp. 1–4.

[50] W.-Y. Huang, A. Bettayeb, R. Kaczmarek, and J.-C. Vannier, "Optimization of magnet segmentation for reduction of eddy-current losses in permanent magnet synchronous machine," *Energy Conversion, IEEE Transactions on*, vol. 25, no. 2, pp. 381–387, June 2010.

[51] F. Deng, "Commutation-caused eddy-current losses in permanent-magnet brushless dc motors," *Magnetics, IEEE Transactions on*, vol. 33, no. 5, pp. 4310–4318, Sep 1997.

[52] K. Atallah, D. Howe, P. Mellor, and D. Stone, "Rotor loss in permanent-magnet brushless ac machines," *Industry Applications, IEEE Transactions on*, vol. 36, no. 6, pp. 1612–1618, Nov 2000.

[53] K. Yoshida, Y. Hita, and K. Kesamaru, "Eddy-current loss analysis in pm of surface-mounted-pm sm for electric vehicles," *Magnetics, IEEE Transactions on*, vol. 36, no. 4, pp. 1941–1944, Jul 2000.

[54] H. Toda, Z. Xia, J. Wang, K. Atallah, and D. Howe, "Rotor eddy-current loss in permanent magnet brushless machines," *Magnetics, IEEE Transactions on*, vol. 40, no. 4, pp. 2104–2106, July 2004.

[55] A. Nagarkatti, O. Mohammed, and N. Demerdash, "Special losses in rotors of electronically commutated brushless dc motors induced by non-uniformly rotating amature MMFS," *Power Apparatus and Systems, IEEE Transactions on*, vol. PAS-101, no. 12, pp. 4502–4507, Dec 1982.

[56] S. T. Lundmark, "Radial and transverese flux IPM core and magnet loss in FEM2D and 3D," Chalmers University of Technology, Gothenburg, Sweden, Technical Report 2015:2, 2015.

[57] K. Yamazaki and A. Abe, "Loss investigation of interior permanent-magnet motors considering carrier harmonics and magnet eddy currents," *Industry Applications, IEEE Transactions on*, vol. 45, no. 2, pp. 659–665, March 2009.

[58] K. Yamazaki and Y. Fukushima, "Effect of eddy-current loss reduction by magnet segmentation in synchronous motors with concentrated windings," *Industry Applications, IEEE Transactions on*, vol. 47, no. 2, pp. 779–788, March 2011.

[59] J. Ede, K. Atallah, G. Jewell, J. Wang, and D. Howe, "Effect of axial segmentation of permanent magnets on rotor loss in modular permanent-magnet brushless machines," *Industry Applications, IEEE Transactions on*, vol. 43, no. 5, pp. 1207–1213, Sept 2007.

[60] K. Yamazaki, M. Shina, Y. Kanou, M. Miwa, and J. Hagiwara, "Effect of eddy current loss reduction by segmentation of magnets in synchronous motors: Difference between interior and surface types," *Magnetics, IEEE Transactions on*, vol. 45, no. 10, pp. 4756–4759, Oct 2009.

[61] S. Lundmark and P. Roshanfekr, "Magnet and core loss in a radial flux and a transverse flux PM traction motor," in *Ecological Vehicles and Renewable Energies (EVER), 2015 Tenth International Conference on*, March 2015, pp. 1–9.

[62] C. Sadarangani, *Electrical Machines-Design and Analysis of Induction and Permanent Magnet Motors*. Royal Insitute of Technology, Stockholm, Sweden: KTH, 2006.

[63] N. Bianchi and M. Barcaro, "A modern approach to the analysis of PM motors using finite element method," in *Industrial Electronics (ISIE), 2010 IEEE International Symposium on*, July 2010.

[64] P. Lindh, J. Pyrhonen, M. Polikarpova, V. Kurvinen, J. Heikkinen, and V. Naumanen, "Electrical and mechanical design of a PM traction motor with tooth coils," in *Power Electronics and Applications (EPE), 2013 15th European Conference on*, Sept 2013, pp. 1–8.

[65] Z. Han, H. Yang, and Y. Chen, "Investigation of the rotor mechanical stresses of various interior permanent magnet motors," in *Electrical Machines and Systems, 2009. ICEMS 2009. International Conference on*, Nov 2009, pp. 1–6.

[66] Y.-L. Lee, M. E. Barkey, and H.-T. Kang, *Metal fatigue analysis handbook: practical problem-solving techniques for computer-aided engineering*. Butterworth-Heinemann, 2012.

[67] T. Thiringer, J. Paixao, and M. Bongiorno, "Monitoring of the ride-through ability of a 2 MW wind turbine in tvååker, halland," Chalmers University of Technology, Department of Energy and Enviroment, Göteborg, Sweden, Tech. Rep., 2009.

[68] C. Mi, G. Slemon, and R. Bonert, "Minimization of iron losses of permanent magnet synchronous machines," *Energy Conversion, IEEE Transactions on*, vol. 20, no. 1, pp. 121–127, 2005.

[69] J. Pyrhönen, T. Jokinen, and V. Hrabovcová, *Design of Rotating Electrical Machines*. John Wiley & Sons, 2010.

[70] L. Melcescu, M. Cistelecan, O. Craiu, and H. Cosan, "A new 4/6 pole-changing double layer winding for three phase electrical machines," in *Electrical Machines (ICEM), 2010 XIX International Conference on*, 2010, pp. 1–6.

[71] J. Luomi, *Magnetic field calculations and electrical machines*. Göteborg, Sweden, Chalmers University of Technology, Department of Energy and Environment, 1997.

[72] C. Mi, G. Slemon, and R. Bonert, "Modeling of iron losses of permanent-magnet synchronous motors," *Industry Applications, IEEE Transactions on*, vol. 39, no. 3, pp. 734–742, May 2003.

[73] K. M. Leban, "Design tool for direct drive wind turbine generators," Ph.D Thesis, Aalborg University, Department of Energy Technology, Aalborg, Denmark, 2014.

[74] T. Li and G. Slemon, "Reduction of cogging torque in permanent magnet motors," *Magnetics, IEEE Transactions on*, vol. 24, no. 6, pp. 2901–2903, Nov 1988.

[75] S.-M. Hwang, J.-B. Eom, Y.-H. Jung, D.-W. Lee, and B.-S. Kang, "Various design techniques to reduce cogging torque by controlling energy variation in permanent magnet motors," *Magnetics, IEEE Transactions on*, vol. 37, no. 4, pp. 2806–2809, Jul 2001.

[76] L. Dosiek and P. Pillay, "Cogging torque reduction in permanent magnet machines," *Industry Applications, IEEE Transactions on*, vol. 43, no. 6, pp. 1565–1571, Nov 2007.

[77] T. Ishikawa and G. Slemon, "A method of reducing ripple torque in permanent magnet motors without skewing," *Magnetics, IEEE Transactions on*, vol. 29, no. 2, pp. 2028–2031, Mar 1993.

[78] S. Meier, "Theoritical design of surface mounted permanent magnet motors with field weakening capability," Master's thesis, 2002.

[79] SurahammarsBruk, "Typical data for SURA M235-35A," Broschur data, 2008. [Online]. Available: http://www.sura.se/Sura/hp_products.nsf/vOpendocument/03A8B2433FAE16C4C1256AA8002280E6/$FILE/235-35.pdf?OpenElement

[80] P. Campbell, *Permanent Magnet Materials and Their Application*. Cambridge University Press, 1996.

[81] E. Lovelace, T. Jahns, T. Keim, and J. H. Lang, "Mechanical design considerations for conventionally laminated, high-speed, interior PM synchronous machine rotors," *Industry Applications, IEEE Transactions on*, vol. 40, no. 3, pp. 806–812, May 2004.

[82] P. Roshanfekr, S. Lundmark, T. Thiringer, and M. Alatalo, "Comparison of a 5 MW permanent magnet assisted synchronous reluctance generator with an IPMSG for wind application," in *Electrical Machines (ICEM), 2014 International Conference on*, Sept 2014, pp. 711–715.

Appendix A

Derivation of the eddy current paths resistance

A.1 Stator flux in the radial direction

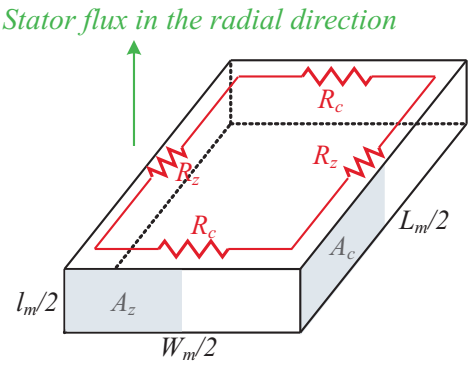

Fig. A.1 Resistances of the eddy current paths when the stator flux is in the radial direction.

The total resistance of the eddy current paths is

$$R_{NoSegment\_FluxRadial} = R_{cTotal} + R_{zTotal} \tag{A.1}$$

where R_{cTotal} is the sum of the resistances in the circumferential direction and R_{zTotal} is the sum of the resistances in the axial direction which are

$$R_{cTotal} = 2R_c \tag{A.2}$$

and

$$R_{zTotal} = 2R_z \tag{A.3}$$

R_c and R_z for a magnet with dimensions shown in Fig. A.1 can be calculated as

$$R_c = \rho \frac{W_m/2}{A_c} \tag{A.4}$$

and

$$R_z = \rho \frac{L_m/2}{A_z} \tag{A.5}$$

Therefore,

$$R_{cTotal} = \rho \frac{W_m}{A_c} \tag{A.6}$$

and

$$R_{zTotal} = \rho \frac{L_m}{A_z} \tag{A.7}$$

Substituting (A.6) and (A.7) in (A.1), the total resistance of the eddy current paths created by the stator flux in the radial direction is

$$R_{NoSegment\_FluxRadial} = \rho \left(\frac{W_m}{A_c} + \frac{L_m}{A_z} \right) \tag{A.8}$$

A.1.1 Circumferentially segmented

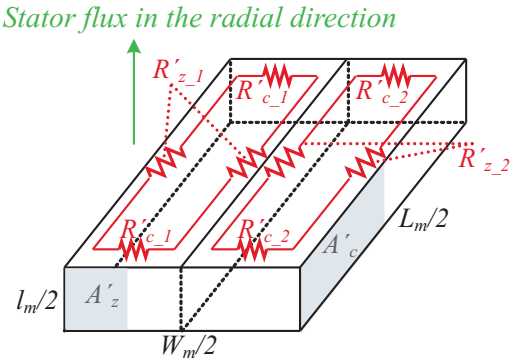

Fig. A.2 Resistances of the eddy current paths when the stator flux is in the radial direction for a magnet segmented circumferentially.

The total resistance of the eddy current paths in the first segment is

$$R'_1 = R'_{cTotal\_1} + R'_{zTotal\_1} \tag{A.9}$$

where R'_{cTotal_1} is the sum of the resistances in the circumferential direction of the first magnet segment and R'_{zTotal_1} is the sum of the resistances in the axial direction of the first magnet segment

$$R'_{cTotal\_1} = 2R'_{c\_1} \tag{A.10}$$

and

$$R'_{zTotal\_1} = 2R'_{z\_1} \tag{A.11}$$

The total resistance of the eddy current paths in the second segment is

$$R'_2 = R'_{cTotal\_2} + R'_{zTotal\_2} \tag{A.12}$$

where R'_{cTotal_2} is the sum of the resistances in the circumferential direction of the second magnet segment and R'_{zTotal_2} is the sum of the resistances in the axial direction of the second magnet segment

$$R'_{cTotal\_2} = 2R'_{c\_2} \tag{A.13}$$

and

$$R'_{zTotal\_2} = 2R'_{z\_2} \tag{A.14}$$

From Fig. A.2, R'_{c_1} and R'_{z_1} can be calculated as

$$R'_{c\_1} = \rho \frac{W_m/4}{A'_c} \tag{A.15}$$

and

$$R'_{z\_1} = \rho \frac{L_m/2}{A'_z} \tag{A.16}$$

As can be seen in Fig. A.1 and Fig. A.2, $A'_c = A_c$ and $A'_z = \frac{1}{2}A_z$. Inserting this in (A.15) and (A.16) and combining them with (A.10) and (A.11),

$$R'_{cTotal\_1} = \rho \frac{W_m/2}{A'_c} = \rho \frac{W_m/2}{A_c} \tag{A.17}$$

and

$$R'_{zTotal\_1} = \rho \frac{L_m}{A'_z} = \rho \frac{2L_m}{A_z} \tag{A.18}$$

Inserting (A.17) and (A.18) in (A.9), the total resistance of the eddy current paths for the first segment is

$$R'_1 = \rho \left(\frac{W_m/2}{A_c} + \frac{2L_m}{A_z} \right) \tag{A.19}$$

Similarly, the total resistance of the eddy current paths for the second segment can be calculated as

$$R'_2 = \rho \left(\frac{W_m/2}{A_c} + \frac{2L_m}{A_z} \right) \tag{A.20}$$

The total resistance of the two magnet segments is

$$R'_{TwoCirSegments\_FluxRadial} = R'_1 + R'_2 \tag{A.21}$$

Substituting (A.19) and (A.20) in (A.21),

$$R'_{TwoCirSegments\_FluxRadial} = \rho\left(\frac{W_m}{A_c} + \frac{4L_m}{A_z}\right) \tag{A.22}$$

A.1.2 Axially segmented

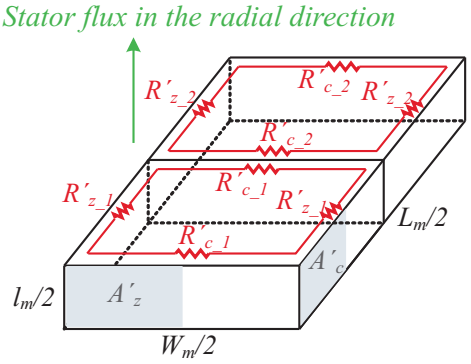

Fig. A.3 Resistances of the eddy current paths when the stator flux is in the radial direction for a magnet segmented axially.

Equations (A.9) to (A.14) can be used in this case as well. From Fig. 2.13(b), R'_{c_1} and R'_{z_1} can be calculated as

$$R'_{c\_1} = \rho\frac{W_m/2}{A'_c} \tag{A.23}$$

and

$$R'_{z\_1} = \rho\frac{L_m/4}{A'_z} \tag{A.24}$$

From Fig. A.1 and Fig. A.3, it can be seen that $A'_c = \frac{1}{2}A_c$ and $A'_z = A_z$. Therefore by inserting these into (A.23) and (A.24) and combing them with (A.10) and (A.11), we get

$$R'_{cTotal\_1} = \rho\frac{W_m}{A'_c} = \rho\frac{2W_m}{A_c} \tag{A.25}$$

and

$$R'_{zTotal\_1} = \rho\frac{L_m/2}{A'_z} = \rho\frac{L_m/2}{A_z} \tag{A.26}$$

From (A.9), (A.25) and (A.26), the total resistance of the eddy current paths for the first segment is

$$R'_1 = \rho\left(\frac{2W_m}{A_c} + \frac{L_m/2}{A_z}\right) \tag{A.27}$$

and similarly, the total resistance of the eddy current paths for the second segment is

$$R'_2 = \rho\left(\frac{2W_m}{A_c} + \frac{L_m/2}{A_z}\right) \tag{A.28}$$

The total resistance of the two magnet segments is

$$R'_{TwoAxialSegments\_FluxRadia} = R'_1 + R'_2 \tag{A.29}$$

Inserting (A.27) and (A.28) in (A.29)

$$R'_{TwoAxialSegments\_FluxRadial} = \rho\left(\frac{4W_m}{A_c} + \frac{L_m}{A_z}\right) \tag{A.30}$$

A.1.3 Radially segmented

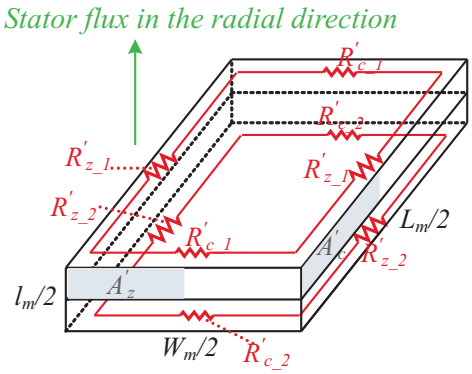

Fig. A.4 Resistances of the eddy current paths when the stator flux is in the radial direction for a magnet segmented radially.

Equations (A.9) to (A.14) can be used in this case as well. From Fig. A.4, R'_{c_1} and R'_{z_1} can be calculated as

$$R'_{c\_1} = \rho\frac{W_m/2}{A'_c} \tag{A.31}$$

and

$$R'_{z\_1} = \rho\frac{L_m/2}{A'_z} \tag{A.32}$$

From Fig. A.1 and Fig. A.4, it can be seen that $A'_c = \frac{1}{2}A_c$ and $A'_z = \frac{1}{2}A_z$. Therefore by inserting these into (A.31) and (A.32) and combing them with (A.10) and (A.11), we have

$$R'_{cTotal\_1} = \rho\frac{W_m}{A'_c} = \rho\frac{2W_m}{A_c} \tag{A.33}$$

and

$$R'_{zTotal\_1} = \rho \frac{L_m}{A'_z} = \rho \frac{2L_m}{A_z} \tag{A.34}$$

From (A.9), (A.33) and (A.34), the total resistance of the eddy current paths for the first segment is

$$R'_1 = \rho \left(\frac{2W_m}{A_c} + \frac{2L_m}{A_z} \right) = 2R_{NoSegment\_FluxRadial} \tag{A.35}$$

and similarly, the total resistance of the eddy current paths for the second segment is

$$R'_2 = \rho \left(\frac{2W_m}{A_c} + \frac{2L_m}{A_z} \right) \tag{A.36}$$

The total resistance of the two magnet segments is

$$R'_{TwoRadialSegments\_FluxRadial} = R'_1 // R'_2 = \frac{R'_1}{2} \tag{A.37}$$

Therefore,

$$R'_{TwoRadialSegments\_FluxRadial} = \rho \left(\frac{W_m}{A_c} + \frac{L_m}{A_z} \right) \tag{A.38}$$

A.2 Stator flux in the circumferential direction

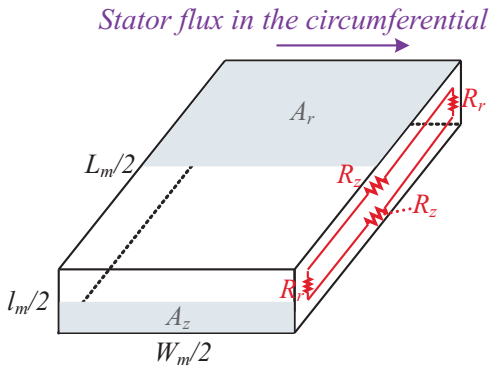

Fig. A.5 Resistances of the eddy current paths when the stator flux is in the circumferential direction.

The total resistance of the eddy current paths created by the stator flux in the circumferential direction is

$$R_{NoSegment\_FluxCircumferential} = R_{rTotal} + R_{zTotal} \tag{A.39}$$

where R_{rTotal} is the sum of the resistances in the radial direction which is

$$R_{rTotal} = 2R_r \tag{A.40}$$

The resistance R_r for a magnet with dimensions shown in Fig. A.5 can be calculated as

$$R_r = \rho \frac{l_m/2}{A_r} \tag{A.41}$$

According to (A.40) and (A.41)

$$R_{rTotal} = \rho \frac{l_m}{A_r} \tag{A.42}$$

Substituting (A.42) and (A.7) in (A.39), the total resistance of the eddy current paths created by the stator flux in the circumferential direction is

$$R_{NoSegment\_FluxCircumferential} = \rho \left(\frac{l_m}{A_r} + \frac{L_m}{A_z} \right) \tag{A.43}$$

A.2.1 Circumferentially segmented

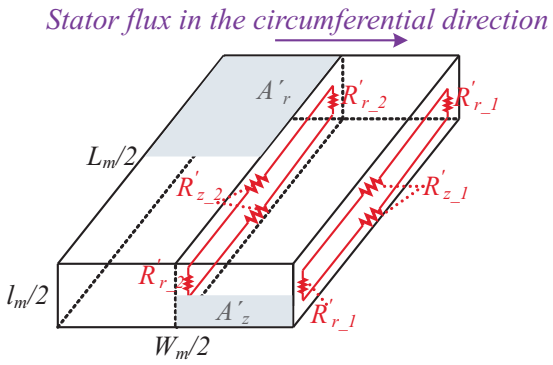

Fig. A.6 Resistances of the eddy current paths when the stator flux is in the circumferential direction for a magnet segmented circumferentially.

The total resistance of the eddy current paths in the first segment is

$$R'_1 = R'_{rTotal\_1} + R'_{zTotal\_1} \tag{A.44}$$

where R'_{rTotal_1} is the sum of the resistances in the radial direction of the first magnet

$$R'_{rTotal\_1} = 2R'_{r\_1} \tag{A.45}$$

and R'_{zTotal_1} is the sum of the resistances in the axial direction of the first magnet

$$R'_{zTotal\_1} = 2R'_{z\_1} \tag{A.46}$$

The total resistance of the eddy current paths in the second segment is

$$R'_2 = R'_{rTotal\_2} + R'_{zTotal\_2} \tag{A.47}$$

where R'_{rTotal_2} and R'_{zTotal_2} are

$$R'_{rTotal\_2} = 2R'_{r\_2} \tag{A.48}$$

and

$$R'_{zTotal\_2} = 2R'_{z\_2} \tag{A.49}$$

From Fig. A.6, R'_{r_1} and R'_{z_1} can be calculated as

$$R'_{r\_1} = \rho\frac{l_m/2}{A'_r} \tag{A.50}$$

and

$$R'_{z\_1} = \rho\frac{L_m/2}{A'_z} \tag{A.51}$$

As can be seen in Fig. A.5 and Fig. A.6, $A'_r = \frac{1}{2}A_r$ and $A'_z = \frac{1}{2}A_z$. Inserting this in (A.50) and (A.51) and using (A.45) and (A.46), the total resistances in the radial (R'_{rTotal_1}) and axial (R'_{zTotal_1}) directions for the first segment are

$$R'_{rTotal\_1} = \rho\frac{l_m}{A'_r} = \rho\frac{2l_m}{A_r} \tag{A.52}$$

and

$$R'_{zTotal\_1} = \rho\frac{L_m}{A'_z} = \rho\frac{2L_m}{A_z} \tag{A.53}$$

Substituting (A.52) and (A.53) in (A.44), the total resistance of the eddy current paths for the first segment is

$$R'_1 = \rho\left(\frac{2l_m}{A_c} + \frac{2L_m}{A_z}\right) = 2R_{NoSegment\_FluxCircumferential} \tag{A.54}$$

Similarly, the total resistance of the eddy current paths for the second segment can be calculated as

$$R'_2 = \rho\left(\frac{2l_m}{A_c} + \frac{2L_m}{A_z}\right) \tag{A.55}$$

The total resistance of the two magnet segments is

$$R'_{TwoCirSegments\_FluxCircumferential} = R'_1//R'_2 = \frac{R'_1}{2} \tag{A.56}$$

Therefore,

$$R'_{TwoCirSegments\_FluxCircumferential} = \rho\left(\frac{W_m}{A_c} + \frac{L_m}{A_z}\right) = R_{NoSegment\_FluxCircumferential} \tag{A.57}$$

A.2.2 Axially segmented

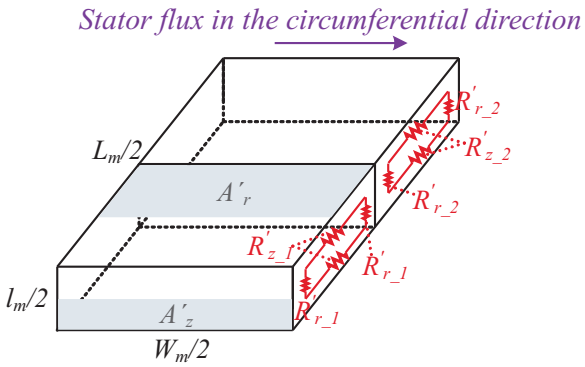

Fig. A.7 Resistances of the eddy current paths when the stator flux is in the circumferential direction for a magnet segmented axially.

From Fig. A.7, the resistance in the radial direction (R'_{r_1}) and the resistance in the axial direction (R'_{z_1}) can be calculated respectively as

$$R'_{r\_1} = \rho\frac{l_m/2}{A'_r} \tag{A.58}$$

and

$$R'_{z\_1} = \rho\frac{L_m/4}{A'_z} \tag{A.59}$$

From Fig. A.5 and Fig. A.7, it can be seen that $A'_r = \frac{1}{2}A_r$ and $A'_z = A_z$. Therefore

$$R'_{rTotal\_1} = \rho\frac{l_m}{A'_r} = \rho\frac{2l_m}{A_r} \tag{A.60}$$

and

$$R'_{zTotal\_1} = \rho\frac{L_m/2}{A'_z} = \rho\frac{L_m/2}{A_z} \tag{A.61}$$

The total resistance of the eddy current paths for the first segment is

$$R'_1 = \rho\left(\frac{2l_m}{A_r} + \frac{L_m/2}{A_z}\right) \tag{A.62}$$

and the total resistance of the eddy current paths for the second segment is

$$R'_2 = \rho\left(\frac{2l_m}{A_r} + \frac{L_m/2}{A_z}\right) \tag{A.63}$$

The total resistance of the two magnet segments can be calculated

$$R'_{TwoAxialSegments\_FluxCircumferential} = R'_1 + R'_2 \tag{A.64}$$

Inserting (A.62) and (A.63) in (A.64)

$$R'_{TwoAxialSegments\_FluxCircumferential} = \rho\left(\frac{4l_m}{A_r} + \frac{L_m}{A_z}\right) \tag{A.65}$$

A.2.3 Radially segmented

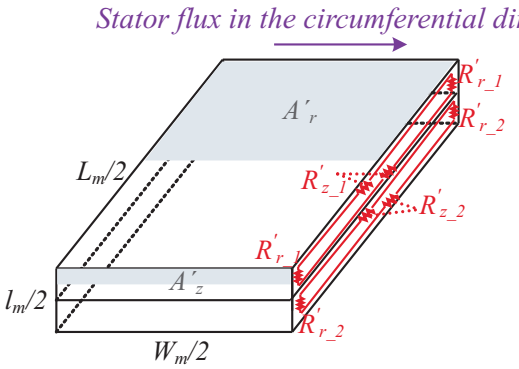

Fig. A.8 Resistances of the eddy current paths when the stator flux is in the circumferential direction for a magnet segmented radially.

From Fig. A.8, the resistances in the radial and axial directions are

$$R'_{r\_1} = \rho\frac{l_m/4}{A'_r} \tag{A.66}$$

and

$$R'_{z\_1} = \rho\frac{L_m/2}{A'_z} \tag{A.67}$$

From Fig. A.5 and Fig. A.8, it can be seen that $A'_r = A_r$ and $A'_z = \frac{1}{2}A_z$. So

$$R'_{rTotal\_1} = \rho\frac{l_m/2}{A'_r} = \rho\frac{l_m/2}{A_r} \tag{A.68}$$

and

$$R'_{zTotal\_1} = \rho\frac{L_m}{A'_z} = \rho\frac{2L_m}{A_z} \tag{A.69}$$

The total resistance of the eddy current paths for the first and second segments are

$$R'_1 = \rho\left(\frac{l_m/2}{A_r} + \frac{2L_m}{A_z}\right) = R'_2 \tag{A.70}$$

The total resistance of the two magnet segments is

$$R'_{TwoRadialSegments\_FluxCircumferential} = R'_1 + R'_2 = \rho\left(\frac{l_m}{A_r} + \frac{4L_m}{A_z}\right) \tag{A.71}$$

A.3 Stator flux in the axial direction

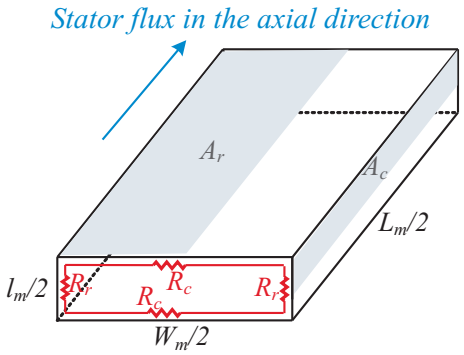

Fig. A.9 Resistances of the eddy current paths when the stator flux is in the axial direction.

The total resistance of the eddy current paths created by the stator flux in the axial direction is

$$R_{NoSegment\_FluxAxial} = R_{rTotal} + R_{cTotal} \tag{A.72}$$

Substituting (A.42) and (A.6) in (A.72), the total resistance of the eddy current paths created by the stator flux in the axial direction is

$$R_{NoSegment\_FluxAxial} = \rho\left(\frac{l_m}{A_r} + \frac{W_m}{A_c}\right) \tag{A.73}$$

A.3.1 Circumferentially segmented

From Fig. A.10, the resistances in the radial and circumferential directions are

$$R'_{r\_1} = \rho\frac{l_m/2}{A'_r} \tag{A.74}$$

and

$$R'_{c\_1} = \rho\frac{W_m/4}{A'_c} \tag{A.75}$$

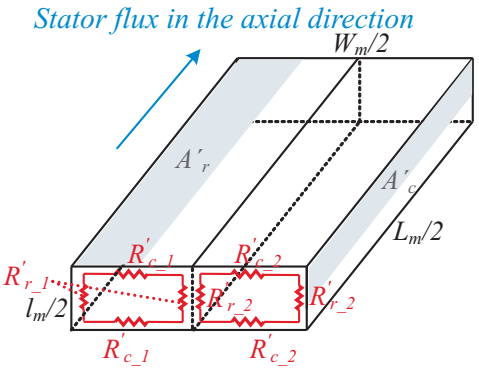

Fig. A.10 Resistances of the eddy current paths when the stator flux is in the axial direction for a magnet segmented circumferentially.

From Fig. A.9 and Fig. A.10, it can be seen that $A'_r = \frac{1}{2}A_r$ and $A'_c = A_c$. So

$$R'_{rTotal\_1} = \rho\frac{l_m}{A'_r} = \rho\frac{2l_m}{A_r} \tag{A.76}$$

and

$$R'_{cTotal\_1} = \rho\frac{W_m/2}{A'_c} = \rho\frac{W_m/2}{A_c} \tag{A.77}$$

The total resistance of the eddy current paths for the first and second segments are

$$R'_1 = \rho\left(\frac{2l_m}{A_r} + \frac{W_m/2}{A_c}\right) = R'_2 \tag{A.78}$$

The total resistance of the two magnet segments is

$$R'_{TwoCirSegments\_FluxAxial} = R'_1 + R'_2 = \rho\left(\frac{4l_m}{A_r} + \frac{W_m}{A_c}\right) \tag{A.79}$$

A.3.2 Axially segmented

From Fig. A.11, the resistances in the radial and circumferential directions are

$$R'_{r\_1} = \rho\frac{l_m/2}{A'_r} \tag{A.80}$$

and

$$R'_{c\_1} = \rho\frac{W_m/2}{A'_c} \tag{A.81}$$

From Fig. A.9 and Fig. A.11, it can be seen that $A'_r = \frac{1}{2}A_r$ and $A'_c = \frac{1}{2}A_c$. So

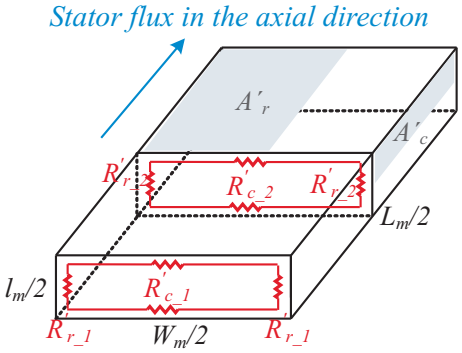

Fig. A.11 Resistances of the eddy current paths when the stator flux is in the axial direction for a magnet segmented axially.

$$R'_{rTotal\_1} = \rho \frac{l_m}{A'_r} = \rho \frac{2l_m}{A_r} \tag{A.82}$$

and

$$R'_{cTotal\_1} = \rho \frac{W_m}{A'_c} = \rho \frac{2W_m}{A_c} \tag{A.83}$$

The total resistance of the eddy current paths for the first and second segments are

$$R'_1 = \rho \left(\frac{2l_m}{A_r} + \frac{2W_m}{A_c} \right) = R'_2 \tag{A.84}$$

$$R'_2 = \rho \left(\frac{2l_m}{A_r} + \frac{2W_m}{A_c} \right) \tag{A.85}$$

The total resistance of the two magnet segments is

$$R'_{TwoAxialSegments\_FluxAxial} = R'_1 // R'_2 = \frac{R'_1}{2} \tag{A.86}$$

Thus

$$R'_{TwoAxialSegments\_FluxAxial} = \rho \left(\frac{l_m}{A_r} + \frac{W_m}{A_c} \right) = R_{NoSegment\_FluxAxial} \tag{A.87}$$

A.3.3 Radially segmented

From Fig. A.12, the resistances in the radial and circumferential directions are

$$R'_{r\_1} = \rho \frac{l_m/4}{A'_r} \tag{A.88}$$

and

$$R'_{c\_1} = \rho \frac{W_m/2}{A'_c} \tag{A.89}$$

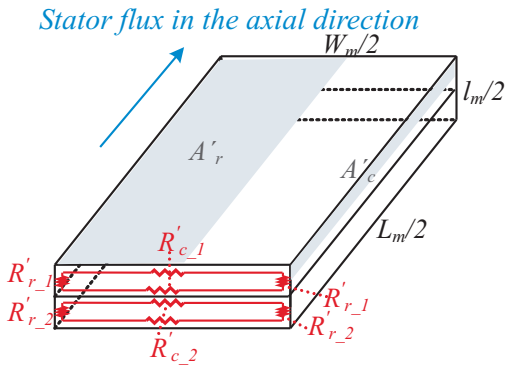

Fig. A.12 Resistances of the eddy current paths when the stator flux is in the axial direction for a magnet segmented radially.

From Fig. A.9 and Fig. A.12, it can be seen that $A'_r = A_r$ and $A'_c = \frac{1}{2}A_c$. So

$$R'_{rTotal\_1} = \rho\frac{l_m/2}{A'_r} = \rho\frac{l_m/2}{A_r} \tag{A.90}$$

and

$$R'_{cTotal\_1} = \rho\frac{W_m}{A'_c} = \rho\frac{2W_m}{A_c} \tag{A.91}$$

The total resistance of the eddy current paths for the first and second segments are

$$R'_1 = \rho\left(\frac{l_m/2}{A_r} + \frac{2W_m}{A_c}\right) = R'_2 \tag{A.92}$$

The total resistance of the two magnet segments is

$$R'_{TwoRadialSegments\_FluxAxial} = R'_1 + R'_2 = \rho\left(\frac{l_m}{A_r} + \frac{4W_m}{A_c}\right) \tag{A.93}$$